Introduction to Gravitational Lensing
Lecture scripts

Massimo Meneghetti

Contents

Introduction

These scripts aim at helping the students of the course on Gravitational Lensing to better understand the arguments discussed in the class.

Their goal is to give an overview on gravitational lensing and on its wide phenomenology. We will start from the basics of the lensing theory, discussing the deflection of light rays and defining some quantities which will be necessary for the rest of the course.

Then, we will discuss lensing on different scales, starting from lensing of point sources by point masses and ending with lensing by large-scale structures on the most extended source on the sky: the Cosmic-Microwave-Background.

Acknowledgements

$\textit{\Large 1}$ Introduction to lensing

1.1   Light deflection and resulting phenomena

It had been speculated even by Newton that masses should deflect light, but he did not know how to describe the deflection properly, because he thought of light as only a wave phenomenon.

In 1783, speculating that light consists of corpuscoles, a geologists, astronomer, natural phylosopher and what-so-ever, named John Mitchell (1724-1793) sent to Henry Cavendish (1731-1810) a paper he had written on a method to measure the mass of stars by detecting the reduction in the light speed by effect of gravity as the light corpuscoles propagated from the star's gravitational field to the Earth. Among the other things, in this paper Mitchel suggested that a sufficiently massive body could completely stop the light it emitted and appear as invisible (hey, aren't these balck holes?).

The paper from Mitchell pushed Cavendish to calculate the Newtonian deflection of light for the first time, probably around 1784. Unfortunately, he did not pubilsh his results. Some private notes where discovered only later.

The calculation was as follows (Will, 1988):

- let start from the assumption that light is composed of material corpuscles;

- according to the equivalence principle, the acceleration of a body in a gravitational field is independent of its mass, structure, composition. Therefore we do not need to care about the corpuscle mass;

- any light corpuscle should experience the acceleration

$$\frac{\mathrm{d}^2 \vec{r}}{\mathrm{d}t^2} = -\frac{Gm\vec{r}}{r^3} \; , \tag{1.1}$$

  where $\vec{r}$ define the position of the corpuscle in the gravitational field of the body whose mass is m;

- the solutions of this equation of motion are conic sections. They can describe bound or unbound orbits. However, the speed of light is so large that it exceeds the escape velocity. Thus, the resulting orbit will be an hyperbolic orbit, which can be parametrically written as

$$r = \frac{R(1+e)}{1+e\cos\phi} \quad , \quad r^2 \frac{\mathrm{d}\phi}{\mathrm{d}t} = [GmR(1+e)]^{1/2} \; , \tag{1.2}$$

In the previous equations R is the radius of the point of closest approach between the corpuscle and the body of mass m, chosen to lie of the x axis, e is the eccentricity of the orbit and ϕ is an angle, counted from the x axis, called *true anomaly*. r and ϕ define the position of the corpuscle with respect to the mass m in polar coordinates.
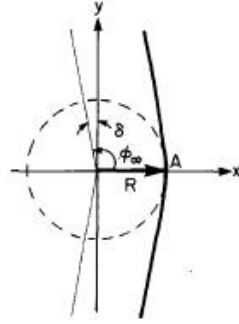
- the vecor $\vec{r}$ is written as

$$\vec{r} = r(\vec{e}_x \cos\phi + \vec{e}_y \sin\phi) \tag{1.3}$$

in terms of the two components along the x and the y axes. Thus, the velocity $\vec{v}$ is

$$\vec{v} = \frac{d\vec{r}}{dt} = \left(\frac{Gm}{R(1+e)}\right)^{1/2} [-\vec{e}_x \sin\phi + \vec{e}_y(\cos\phi + e)], \tag{1.4}$$

$$v^2 = \frac{Gm}{R(1+e)}(1 + 2e\cos\phi + e^2). \tag{1.5}$$

- as $r \to \infty$, the trajectory approaches asymptotes that make an angle ϕ_∞ with the x-axis; this occurs when

$$(1 + e\cos\phi) = 0 \Rightarrow \cos\phi_\infty = -\frac{1}{e}. \tag{1.6}$$

If we define $\phi_\infty \equiv \pi/2 + \delta$, where δ is one-half the deflection angle, then

$$\sin\delta = \frac{1}{e}; \tag{1.7}$$

- for determining the deflection angle, we need to determine the eccentricity. Now, let assume that the corpuscle is emitted at infinity with velocity c. Then, from Eq. 1.5 we obtain

$$c^2 = v^2|_{\phi=\phi_\infty} = \frac{Gm}{R(1+e)}(e^2 - 1) \tag{1.8}$$

$$= \frac{Gm}{R}(e - 1). \tag{1.9}$$

Thus,

$$e = \frac{Rc^2}{Gm} + 1; \tag{1.10}$$

- if the massive body is the Sun and the light is grazing its surface,

$$m = M_\odot = 1.989 \times 10^{30}\text{kg} \tag{1.11}$$

$$R = R_\odot = 6.96 \times 10^8\text{m} \tag{1.12}$$

and the deflection angles is

$$\Delta\theta \equiv 2\delta \approx \frac{2Gm}{c^2 R} \approx 0''.875 \tag{1.13}$$

However, we have to wait until the beginning of the XIXth century for finding an official document by Johann Soldner (1801), where these calculations were published. The result shown above is just one half of the true deflection, because it is derived by neglecting the local curvature of the space-time around massive bodies.
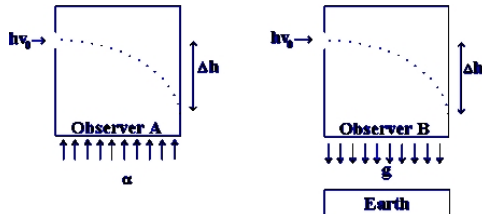
Using an argument based on the principle of equivalence, but still without full equations of relativity, Albert Einstein realized that massive bodies deflect light. The argument works like this. The principle of equivalence states that gravity and acceleration cannot be distinguished. In other words, a free falling observer does not feel gravity and an accelerated observer can interpret the resulting inertial force as due to a gravitational field. Suppose that the observer is contained in a box with a hole on its left side (see upper figure). If the box is accelerated upwards, the observer interprets the inertial force on him as a gravitational force acting downwards. Suppose that a light ray enters the hole on the left side of the box and propagates towards right. As the box is moving upwards, the ray hits the wall of the box on the opposite side at a lower point than it enter. As the box is accelerated the light ray appears curved. Then, based on the principle of equivalence, light must be deflected by gravity. Indeed, we can imagine to reverse the experiment: let the box to be stationary and within the gravitational field whose intesity is such to resemble the previous acceleration. If light is not deflected by gravity, then the oberver has the possibility to discriminate between gravity and acceleration, violating the principle of equivalence.

In order to get the correct value of the deflection of light by a mass M, we need to use the Theory of General Relativity (Einstein, 1916). According to this theory, the deflection is described by geodesic lines following the curvature of the space-time. In curved space-time, geodesic lines are lines which are as "straight as possible", resembling straight lines in flat space-time. As a light ray follows the curvature, it is bent towards the mass which causes the space-time to be curved. This bending gives rise to several important phenomena:

- multiple paths around a single mass become possible, e.g. one around the left and one around the right side of the deflector. The observer, who will see an image of the source along the backward tangent of each ray arriving at his position, will then see multiple images of a single source;

- in addition, the light deflection of two neighbouring rays may be different. Suppose a pair of rays, one from one side and one from the other side of a source, passes by a lensing mass distribution. The ray which passes closer to the deflector will be bent more than the other, thus the source will appear stretched. It is thus expected that gravitational lensing will typically distort the sources. By the same mechanism, they can appear larger or smaller than they originally are;

- since photons are not created, neither destroyed by the lensing effect the surface brightness of the source will remain unchanged. Since, as we said, the size is not conserved, this implys that the source can be either *magnified* or *demagnified* by lensing. If it is enlarged it will appear brigher, otherwise fainter;

- in case that multiple light paths are possible between the source and the observer, since they will be characterized by different lengths, the light travel times will differ

for the different images. One of the images will appear first, the others will be delayed.

Starting from the equivalence principle, we are thus arrived at the expectation of multiple images, distortions, magnification, and time delayes. All of these phenomena have been observed in numerous cases.

Example: Multiply-imaged quasars

Identification of the lensing galaxy in a double quasar system: the left panel shows on infrared (J-band) observation of the two images of double quasar HE 1104-1825 ($z_Q = 2.316$, $\theta = 3.2''$). The right panel obtained with some new deconvolution technique nicely reveals the lensing galaxy (at $z_G = 1.66$) between the quasar images (Credits: European Southern Observatory).
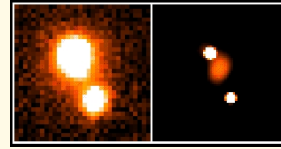
Example: Einstein ring

B1938+666 is another multiple-image lens, and was discovered in JVAS (Jodrell/VLA Astrometric Survey). This is a survey of flat-spectrum radio sources designed to identify gravitational lens candidates. HST observations show an Einstein ring in IR. The lens redshift is 0.878, but the source redshift is not yet known (IR spectroscopy required).
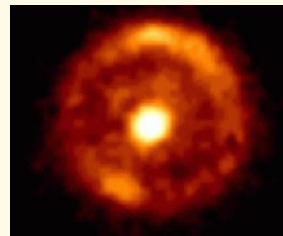
The bottom figure shows a MERLIN image of this system at 5GHz. In radio there is a significant arc visible.
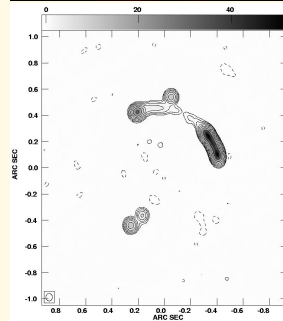
Credit: JVAS/CLASS

Example: Arcs in galaxy clusters

Abell 1689 is a galaxy cluster at z=0.183. The gravity of the cluster's trillion stars - plus dark matter - acts as a 2-million-light-year-wide 'lens' in space. This 'gravitational lens' bends and magnifies the light of galaxies located far behind it, distorting their shapes and creating multiple images of individual galaxies.
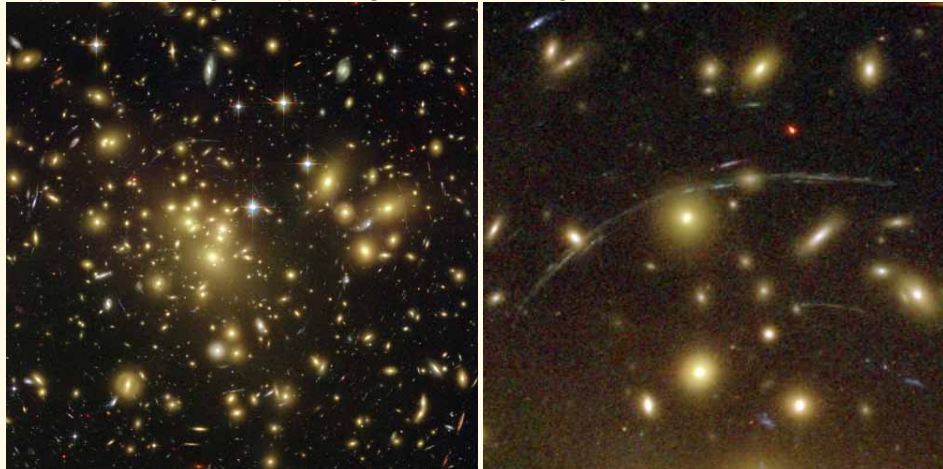
Credit: NASA, N. Benitez (JHU), T. Broadhurst (The Hebrew University), H. Ford (JHU), M. Clampin(STScI), G. Hartig (STScI), G. Illingworth (UCO/Lick Observatory), the ACS Science Team and ESA.

HST (H)

B

1 arcsec

A
B−0.69
shifted 51 days
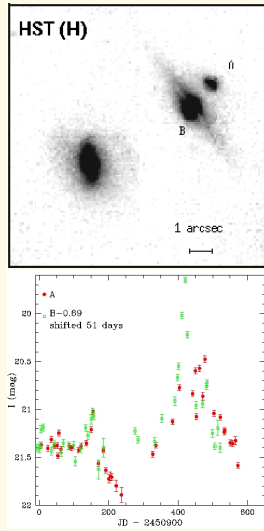
B1600+434 is a double gravitational lens system. A distant QSO at redshift $z = 1.59$ is lensed by an edge-on-late-type galaxy at $z = 0.41$ and has two images, labeled with A and B in the upper image. QSO's are characterized by intrinsic variability of their luminosity. The light curves of the two images have the same shape, as expected since they arise from the same source. However, the light curve of the image B is shifted by ~ 50 days with respect to that of image A. The reason is the different path of the light coming from the two images.

Credit: I. Burud, Institut d'Astrophysique et de Gophysique de Lige, Avenue de Cointe 5, B-4000 Lige, Belgium

1.2 Fermat's principle and light deflection

Starting from the field equations of general relativity, light deflection can be calculated by studying geodesic curves. It turns out that light deflection can equivalently be described by Fermat's principle, as in geometrical optics. This will be our starting point.

In its simplest form the Fermat's principle says that light waves of a given frequency traverse the path between two points which takes the least time. The speed of light in a medium with refractive index n is c/n, where c is its speed in a vacuum. Thus, the time required for light to go some distance in such a medium is n times the time light takes to go the same distance in a vacuum.
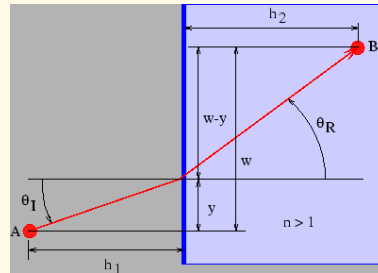
Referring to the figure above, the time required for light to go from A to B becomes

$$t = [\{h_1^2 + y^2\}^{1/2} + n\{h_2^2 + (w - y)^2\}^{1/2}]/c.$$

We find the minimum time by differentiating t with respect to y and setting the result to zero, with the result that

$$\frac{y}{\{h_1^2 + y^2\}^{1/2}} = n\frac{w - y}{\{h_2^2 + (w - y)^2\}^{1/2}}.$$

However, we note that the left side of this equation is simply $\sin \theta_I$, while the right side is $n \sin \theta_R$, so that the minimum time condition reduces to

$$\sin \theta_I = n \sin \theta_R$$

We recognize this result as Snell's law.

We first need an index of refraction n because Fermat's principle says that light will follow a path along which the travel time,

$$\int \frac{n}{c} \mathrm{d}l \ , \tag{1.14}$$

will be extremal. As in geometrical optics, we thus search for a path, $\vec{x}(l)$, for which the variation

$$\delta \int_A^B n(\vec{x}(l)) \mathrm{d}l = 0 \ , \tag{1.15}$$

where the starting point A and the end point B are kept fixed.

In order to find the index of refraction, we make a first approximation: we assume that the lens is weak, and that it is small compared to the overall dimensions of the optical system composed of source, lens and observer. With "weak lens", we mean a lens whose Newtonian gravitational potential Φ is much smaller than c^2, $\Phi/c^2 \ll 1$. Note that this approximation is valid in virtually all cases of astrophysical interest. Consider for istance a galaxy cluster: its gravitational potential is $|\Phi| < 10^{-4}c^2 \ll c^2$.

The metric of unperturbed space-time is the Minkowski metric,

$$\eta_{\mu\nu} = \begin{pmatrix} 1 & 0 & 0 & 0 \\ 0 & -1 & 0 & 0 \\ 0 & 0 & -1 & 0 \\ 0 & 0 & 0 & -1 \end{pmatrix} \ ,$$

whose line element is

$$\mathrm{d}s^2 = \eta_{\mu\nu}\mathrm{d}x^\mu\mathrm{d}x^\nu = (\mathrm{d}x^0)^2 - (\mathrm{d}\vec{x})^2 = c^2\mathrm{d}t^2 - (\mathrm{d}\vec{x})^2 \ . \tag{1.16}$$

A weak lens perturbs this metric such that

$$\eta_{\mu\nu} \rightarrow g_{\mu\nu} = \begin{pmatrix} 1 + \frac{2\Phi}{c^2} & 0 & 0 & 0 \\ 0 & -(1 - \frac{2\Phi}{c^2}) & 0 & 0 \\ 0 & 0 & -(1 - \frac{2\Phi}{c^2}) & 0 \\ 0 & 0 & 0 & -(1 - \frac{2\Phi}{c^2}) \end{pmatrix}$$

for which the line element becomes

$$\mathrm{d}s^2 = g_{\mu\nu}\mathrm{d}x^\mu\mathrm{d}x^\nu = \left(1 + \frac{2\Phi}{c^2}\right)c^2\mathrm{d}t^2 - \left(1 - \frac{2\Phi}{c^2}\right)(\mathrm{d}\vec{x})^2 \ . \tag{1.17}$$

Now light propagates at zero eigentime, $\mathrm{d}s = 0$, from which we gain

$$\left(1 + \frac{2\Phi}{c^2}\right)c^2\mathrm{d}t^2 = \left(1 - \frac{2\Phi}{c^2}\right)(\mathrm{d}\vec{x})^2 \ . \tag{1.18}$$

The light speed in the gravitational field is thus

$$c' = \frac{|\mathrm{d}\vec{x}|}{\mathrm{d}t} = c\sqrt{\frac{1 + \frac{2\Phi}{c^2}}{1 - \frac{2\Phi}{c^2}}} \approx c\left(1 + \frac{2\Phi}{c^2}\right) \ , \tag{1.19}$$

where we have used that $\Phi/c^2 \ll 1$ by assumption. The index of refraction is thus

$$n = c/c' = \frac{1}{1 + \frac{2\Phi}{c^2}} \approx 1 - \frac{2\Phi}{c^2} \;. \tag{1.20}$$

With $\Phi \leq 0$, $n \geq 1$, and the light speed c' is lower than in vacuum.

n will typically depend on the spatial coordinate $\vec{x}$ and perhaps also on time t. Let $\vec{x}(l)$ be a light path. Then the light travel time is proportional to

$$\int_A^B n[\vec{x}(l)]\mathrm{d}l \;, \tag{1.21}$$

and the light path follows from

$$\delta \int_A^B n[\vec{x}(l)]\mathrm{d}l = 0 \;. \tag{1.22}$$

This is a standard variational problem, which leads to the well known Euler equations. In our case we write

$$\mathrm{d}l = \left|\frac{\mathrm{d}\vec{x}}{\mathrm{d}\lambda}\right|\mathrm{d}\lambda \;, \tag{1.23}$$

with a curve parameter λ which is yet arbitrary, and find

$$\delta \int_{\lambda_A}^{\lambda_B} \mathrm{d}\lambda\, n[\vec{x}(\lambda)] \left|\frac{\mathrm{d}\vec{x}}{\mathrm{d}\lambda}\right| = 0 \tag{1.24}$$

The expression

$$n[\vec{x}(\lambda)] \left|\frac{\mathrm{d}\vec{x}}{\mathrm{d}\lambda}\right| \equiv L(\dot{\vec{x}}, \vec{x}, \lambda) \tag{1.25}$$

takes the role of the Lagrangian in analytic mechanics, with

$$\dot{\vec{x}} \equiv \frac{\mathrm{d}\vec{x}}{\mathrm{d}\lambda} \;. \tag{1.26}$$

Finally, we have

$$\left|\frac{\mathrm{d}\vec{x}}{\mathrm{d}\lambda}\right| = |\dot{\vec{x}}| = (\dot{\vec{x}}^2)^{1/2} \;. \tag{1.27}$$

Using these expressions, we find the Euler equations

$$\frac{\mathrm{d}}{\mathrm{d}\lambda}\frac{\partial L}{\partial \dot{\vec{x}}} - \frac{\partial L}{\partial \vec{x}} = 0 \;. \tag{1.28}$$

Now,

$$\frac{\partial L}{\partial \vec{x}} = |\dot{\vec{x}}|\frac{\partial n}{\partial \vec{x}} = (\vec{\nabla} n)|\dot{\vec{x}}| \;, \frac{\partial L}{\partial \dot{\vec{x}}} = n\frac{\dot{\vec{x}}}{|\dot{\vec{x}}|} \;. \tag{1.29}$$
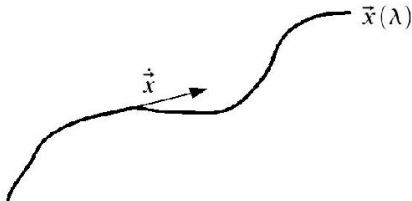
Evidently, $\dot{\vec{x}}$ is a tangent vector to the light path , which we can assume to be normalized by a suitable choice for the curve parameter λ. We thus assume $|\dot{\vec{x}}| = 1$ and write $\vec{e} \equiv \dot{\vec{x}}$ for the unit tangent vector to the light path. Then, we have

$$\frac{\mathrm{d}}{\mathrm{d}\lambda}(n\vec{e}) - \vec{\nabla}n = 0 , \tag{1.30}$$

or

$$n\dot{\vec{e}} + \vec{e} \cdot [(\vec{\nabla}n)\dot{\vec{x}}] = \vec{\nabla}n , \tag{1.31}$$

$$\Rightarrow n\dot{\vec{e}} = \vec{\nabla}n - \vec{e}(\vec{\nabla}n \cdot \vec{e}) . \tag{1.32}$$

The second term on the right hand side is the derivative along the light path, thus the whole right hand side is the gradient of n perpendicular to the light path. Thus

$$\dot{\vec{e}} = \frac{1}{n}\vec{\nabla}_\perp n = \vec{\nabla}_\perp \ln n . \tag{1.33}$$

As $n = 1 - 2\Phi/c^2$ and $\Phi/c^2 \ll 1$, $\ln n \approx -2\Phi/c^2$, and

$$\dot{\vec{e}} \approx -\frac{2}{c^2}\vec{\nabla}_\perp \Phi . \tag{1.34}$$

The total deflection angle of the light path is now the integral over $-\dot{\vec{e}}$ along the light path,

$$\hat{\vec{\alpha}} = \frac{2}{c^2}\int_{\lambda_A}^{\lambda_B} \vec{\nabla}_\perp \Phi \mathrm{d}\lambda . \tag{1.35}$$

The deflection is thus the integral over the "pull" of the gravitational potential perpendicular to the light path. Note that $\vec{\nabla}\Phi$ points away from the lens centre, so $\hat{\vec{\alpha}}$ points towards it.

As it stands, the equation for $\hat{\vec{\alpha}}$ is not useful, as we would have to integrate over the actual light path. However, since $\Phi/c^2 \ll 1$, we expect the deflection angle to be small. Then, we can adopt the Born approximation familiar from scattering theory and integrate over the unperturbed light path.

Suppose, therefore, a light ray starts out into $+\vec{e}_z$-direction and passes a lens at $z = 0$, with impact parameter b. The deflection angle is then given by

$$\hat{\vec{\alpha}}(b) = \frac{2}{c^2}\int_{-\infty}^{+\infty} \vec{\nabla}_\perp \phi \mathrm{d}z \tag{1.36}$$

Special case: point mass lens

If the lens is a point mass, then

$$\Phi = -\frac{GM}{r} \tag{1.37}$$

with $r = \sqrt{x^2 + y^2 + z^2} = \sqrt{b^2 + z^2}$, $b = \sqrt{x^2 + y^2}$ and

$$\vec{\nabla}_\perp \phi = \begin{pmatrix} \partial_x \Phi \\ \partial_y \Phi \end{pmatrix} = \frac{GM}{r^3} \begin{pmatrix} x \\ y \end{pmatrix} . \tag{1.38}$$

The deflection angle is then

$$\begin{aligned}
\hat{\vec{\alpha}}(b) &= \frac{2GM}{c^2} \begin{pmatrix} x \\ y \end{pmatrix} \int_{-\infty}^{+\infty} \frac{\mathrm{d}z}{(b^2 + z^2)^{3/2}} \\
&= \frac{4GM}{c^2} \begin{pmatrix} x \\ y \end{pmatrix} \left[\frac{z}{b^2(b^2 + z^2)^{1/2}} \right]_0^\infty = \frac{4GM}{c^2 b} \begin{pmatrix} \cos\phi \\ \sin\phi \end{pmatrix} ,
\end{aligned} \tag{1.39}$$

with

$$\begin{pmatrix} x \\ y \end{pmatrix} = b \begin{pmatrix} \cos\phi \\ \sin\phi \end{pmatrix} \tag{1.40}$$

Notice that $R_s = \frac{2GM}{c^2}$ is the Schwarzschild radius of a (point) mass M, thus

$$|\hat{\vec{\alpha}}| = \frac{4GM}{c^2 b} = 2\frac{R_s}{b} . \tag{1.41}$$

Also notice that $\hat{\vec{\alpha}}$ is linear in M, thus the deflection angles of an array of lenses can linearly be superposed.

Note that the deflection angle found here in the framework of general relativity exceeds by a factor of two that calculated by using standard Newtonian Gravity (see Eq. 1.13), as anticipated at the beginning of this chapter.

Since the speed of the light is reduced in the gravitational field, $c' = c/n$, the travel time (along the perturbed path) is larger by

$$\Delta t = \int \frac{\mathrm{d}l}{c'} - \int \frac{\mathrm{d}l}{c} = \int (n-1) \mathrm{d}l = -\frac{2}{c^3} \int \Phi \mathrm{d}l . \tag{1.42}$$

This is the so-called *Shapiro delay* (Shapiro, 1964).

2 General concepts

2.1 The general lens

The deflection angle in Eq. 1.41 depends linearly on the mass M. This ensures that the deflection angles of an array of lenses can linearly be superposed. Suppose we have a sparse distribution of N point masses on a plane, whose positions and masses are $\vec{\xi}_i$ and M_i, $1 \leq i \leq N$. The deflection angle of a light ray crossing the plane at $\vec{\xi}$ will be:

$$\hat{\vec{\alpha}}(\vec{\xi}) = \sum_i \hat{\vec{\alpha}}_i(\vec{\xi} - \vec{\xi}_i) = \frac{4G}{c^2} \sum_i M_i \frac{\vec{\xi} - \vec{\xi}_i}{|\vec{\xi} - \vec{\xi}_i|^2} \ . \tag{2.1}$$

We now consider more realistic lens models, i.e. three dimensional distributions of matter. Even in the case of lensing by galaxy clusters, the physical size of the lens is generally much smaller than the distances between observer, lens and source. The deflection therefore arises along a very short section of the light path. This justifies the usage of the *thin screen approximation* (see Fig. (2.1)): the lens is approximated by a planar distribution of matter, the lens plane. Even the sources are assumed to lie on a plane, called the source plane.

Within this approximation, the lensing matter distribution is fully described by its surface density,

$$\Sigma(\vec{\xi}) = \int \rho(\vec{\xi}, z) \ \mathrm{d}z \ , \tag{2.2}$$

where $\vec{\xi}$ is a two-dimensional vector on the lens plane and ρ is the three-dimensional density.

As long as the thin screen approximation holds, the total deflection angle is obtained by summing the contribution of all the mass elements $\Sigma(\vec{\xi})\mathrm{d}^2\xi$:

$$\hat{\vec{\alpha}}(\vec{\xi}) = \frac{4G}{c^2} \int \frac{(\vec{\xi} - \vec{\xi'})\Sigma(\vec{\xi'})}{|\vec{\xi} - \vec{\xi'}|^2} \ \mathrm{d}^2\xi' \ . \tag{2.3}$$

2.2 Lens equation

In Fig. (2.1) we sketch a typical gravitational lens system. A mass concentration is placed at redshift z_L, corresponding to an angular diameter distance D_L. This lens deflects the light rays coming from a source at redshift z_S (or angular distance D_S).
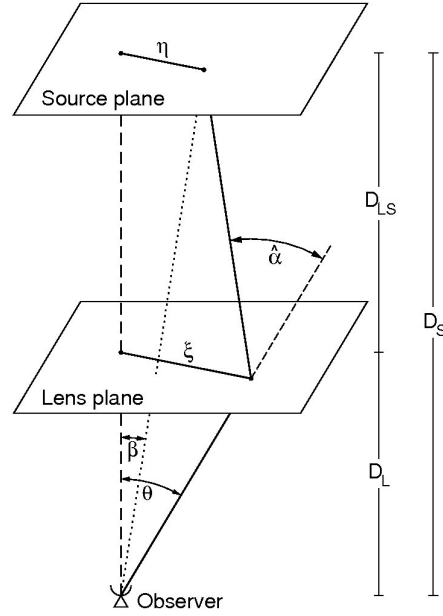
Figure 2.1: Sketch of a typical gravitational lensing system (Figure from Bartelmann & Schneider, 2001).

> **Remark:**
>
> It is not guaranteed that the relation between physical size, distance and angular size can be written as $[\text{physical size}] = [\text{angular size}] \cdot [\text{distance}]$ if space is curved. It is however possible to define distances in curved spacetime such that this relation from Euclidean space holds. Then, however, distances are not additive, such that $D_{\mathrm{L}} + D_{\mathrm{LS}} \neq D_{\mathrm{S}}$.

We first define an optical axis, indicated by the dashed line, perpendicular to the lens and source planes and passing through the observer. Then we measure the angular positions on the lens and on the source planes with respect to this reference direction.

Consider a source at the angular position $\vec{\beta}$, which lies on the source plane at a distance $\vec{\eta} = \vec{\beta} D_{\mathrm{S}}$ from the optical axis. The deflection angle $\hat{\vec{\alpha}}$ of the light ray coming from that source and having an impact parameter $\vec{\xi} = \vec{\theta} D_{\mathrm{L}}$ on the lens plane is given by Eq. (1.36). Due to the deflection, the observer receives the light coming from the source as if it was emitted at the angular position $\vec{\theta}$.

If $\vec{\theta}$, $\vec{\beta}$ and $\hat{\vec{\alpha}}$ are small, the true position of the source and its observed position on the sky are related by a very simple relation, obtained by a geometrical construction. This relation is called the *lens equation* and is written as

$$\vec{\theta} D_{\mathrm{S}} = \vec{\beta} D_{\mathrm{S}} + \hat{\vec{\alpha}} D_{\mathrm{LS}} \; , \tag{2.4}$$

where D_{LS} is the angular diameter distance between lens and source.

Defining the reduced deflection angle

$$\vec{\alpha}(\vec{\theta}) \equiv \frac{D_{\mathrm{LS}}}{D_{\mathrm{S}}} \hat{\vec{\alpha}}(\vec{\theta}) \; , \tag{2.5}$$

from Eq. (2.4), we obtain

$$\vec{\beta} = \vec{\theta} - \vec{\alpha}(\vec{\theta}) \; . \tag{2.6}$$

This equation, called *lens equation* is apparently very simple. All the interesting physics of lensing arises because $\vec{\alpha}$ depends on $\vec{\theta}$.

It is very common and useful to write Eq. (2.4) in dimensionless form. This can be done by defining a length scale ξ_0 on the lens plane and a corresponding length scale $\eta_0 = \xi_0 D_{\mathsf{S}}/D_{\mathsf{L}}$ on the source plane. Then we define the dimensionless vectors

$$\vec{x} \equiv \frac{\vec{\xi}}{\xi_0} \quad ; \quad \vec{y} \equiv \frac{\vec{\eta}}{\eta_0} \ , \tag{2.7}$$

as well as the scaled deflection angle

$$\vec{\alpha}(\vec{x}) = \frac{D_{\mathsf{L}} D_{\mathsf{LS}}}{\xi_0 D_{\mathsf{S}}} \hat{\vec{\alpha}}(\xi_0 \vec{x}) \ . \tag{2.8}$$

Carrying out some substitutions, Eq. (2.4) can finally be written as

$$\vec{y} = \vec{x} - \vec{\alpha}(\vec{x}) \ . \tag{2.9}$$

Special case: axially symmetric lenses

In general, the deflection angle is a two-dimensional vector. In the case of axially symmetric lenses we may compute it only in one dimension, since all light rays from the source to the observer must lie in the plane spanned by the center of the lens, the source and the observer. This can be seen explicitely as follows.

We start from Eq. 2.3. Let take the lens center as the origin of the reference frame. By symmetry, we can choose the reference frame such that $\vec{\xi} = (\xi, 0)$, $\xi \geq 0$. In polar coordinates, $\vec{\xi'} = (\xi_1', \xi_2') = \xi'(\cos\phi, \sin\phi)$.

Then,

$$\vec{\xi} - \vec{\xi'} = (\xi - \xi'\cos\phi, -\xi'\sin\phi) \tag{2.10}$$
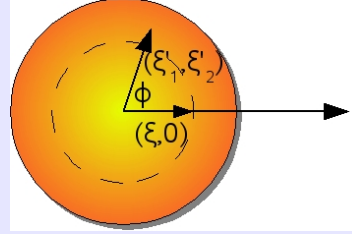
$$|\vec{\xi} - \vec{\xi'}|^2 = \xi^2 + \xi'^2\cos^2\phi - 2\xi\xi'\cos\phi + \xi'^2\sin^2\phi$$
$$= \xi^2 + \xi'^2 - 2\xi\xi'\cos\phi \tag{2.11}$$

For a symmetric mass distribution $\Sigma(\vec{\xi}) = \Sigma(|\vec{\xi}|)$. The components of the deflection angle are thus

$$\hat{\alpha}_1(\vec{\xi}) = \frac{4G}{c^2} \int_0^\infty d\xi' \xi' \Sigma(\xi') \int_0^{2\pi} d\phi \frac{\xi - \xi'\cos\phi}{\xi^2 + \xi'^2 - 2\xi\xi'\cos\phi}$$

$$\hat{\alpha}_2(\vec{\xi}) = \frac{4G}{c^2} \int_0^\infty d\xi' \xi' \Sigma(\xi') \int_0^{2\pi} d\phi \frac{-\xi'\sin\phi}{\xi^2 + \xi'^2 - 2\xi\xi'\cos\phi} \tag{2.12}$$

By symmetry, the second component of the deflection angle is zero, therefore $\hat{\vec{\alpha}}$ is parallel to $\vec{\xi}$. Thus, using the lens equation, we find that also the vector $\vec{\eta}$ must be parallel to $\vec{\xi}$.

For the first component of the deflection angle in Eq. 2.12, the inner integral vanishes for $\xi' > \xi$, while it is $2\pi/\xi$ if $\xi' < \xi$. Then, the deflection angle for an axially symmetric lens is

$$\hat{\alpha}(\xi) = \frac{4G}{c^2} \frac{2\pi \int_0^\xi \Sigma(\xi')\xi' \, d\xi'}{\xi} = \frac{4GM(\xi)}{c^2\xi} \ . \tag{2.13}$$

The formula is similar to that derived for a point mass. The deflection is determined by the mass enclosed by the circle of radius ξ, $M(\xi)$.

2.3   Lensing potential

An extended distribution of matter is characterized by its *effective lensing potential*, obtained by projecting the three-dimensional Newtonian potential on the lens plane and by properly rescaling it:

$$\hat{\Psi}(\vec{\theta}) = \frac{D_{\mathrm{LS}}}{D_{\mathrm{L}} D_{\mathrm{S}}} \frac{2}{c^2} \int \Phi(D_{\mathrm{L}}\vec{\theta}, z)\mathrm{d}z \ . \tag{2.14}$$

The dimensionless counterpart of this function is given by

$$\Psi = \frac{D_{\mathrm{L}}^2}{\xi_0^2} \hat{\Psi} \ . \tag{2.15}$$

This lensing potential satisfies two important properties:

(1) the gradient of Ψ gives the scaled deflection angle:

$$\vec{\nabla}_x \Psi(\vec{x}) = \vec{\alpha}(\vec{x}) \ . \tag{2.16}$$

Indeed,

$$\vec{\nabla}_x \Psi(\vec{x}) = \xi_0 \vec{\nabla}_\perp \left(\frac{D_{\mathrm{LS}} D_{\mathrm{L}}}{\xi_0^2 D_{\mathrm{S}}} \frac{2}{c^2} \int \Phi(\vec{x}, z)\mathrm{d}z \right) \tag{2.17}$$

$$= \frac{D_{\mathrm{LS}} D_{\mathrm{L}}}{\xi_0 D_{\mathrm{S}}} \frac{2}{c^2} \int \vec{\nabla}_\perp \Phi(\vec{x}, z)\mathrm{d}z \tag{2.18}$$

$$= \vec{\alpha}(\vec{x}) \tag{2.19}$$

(2) the Laplacian of Ψ gives twice the *convergence*:

$$\triangle_x \Psi(\vec{x}) = 2\kappa(\vec{x}) \ . \tag{2.20}$$

This is defined as a dimensionless surface density

$$\kappa(\vec{x}) \equiv \frac{\Sigma(\vec{x})}{\Sigma_{\mathrm{cr}}} \quad \text{with} \quad \Sigma_{\mathrm{cr}} = \frac{c^2}{4\pi G} \frac{D_{\mathrm{S}}}{D_{\mathrm{L}} D_{\mathrm{LS}}} \ , \tag{2.21}$$

where Σ_{cr} is called the *critical surface density*, a quantity which characterizes the lens system and which is a function of the angular diameter distances of lens and source.

Eq. 2.20 is derived from the Poisson equation,

$$\triangle \Phi = 4\pi G \rho \ . \tag{2.22}$$

The surface mass density is

$$\Sigma(\vec{\theta}) = \frac{1}{4\pi G} \int_{-\infty}^{+\infty} \triangle \Phi \mathrm{d}z \tag{2.23}$$

and

$$\kappa(\vec{\theta}) = \frac{1}{c^2} \frac{D_{\mathrm{L}} D_{\mathrm{LS}}}{D_{\mathrm{S}}} \int_{-\infty}^{+\infty} \triangle \Phi \mathrm{d}z \ . \tag{2.24}$$

Let us now introduce a two-dimensional Laplacian

$$\triangle_\theta = \frac{\partial^2}{\partial\theta_1^2} + \frac{\partial^2}{\partial\theta_2^2} = D_L^2\left(\frac{\partial^2}{\partial\xi_1^2} + \frac{\partial^2}{\partial\xi_2^2}\right) = D_L^2\left(\triangle - \frac{\partial^2}{\partial z^2}\right) , \tag{2.25}$$

which gives

$$\triangle\Phi = \frac{1}{D_L^2}\triangle_\theta\Phi + \frac{\partial^2\Phi}{\partial z^2} . \tag{2.26}$$

Inserting Eq. 2.26 into Eq. 2.24, we obtain

$$\kappa(\vec{\theta}) = \frac{1}{c^2}\frac{D_{LS}}{D_S D_L}\left[\triangle_\theta\int_{-\infty}^{+\infty}\Phi \mathrm{d}z + D_L^2\int_{-\infty}^{+\infty}\frac{\partial^2\Phi}{\partial z^2}\mathrm{d}z\right] . \tag{2.27}$$

If the lens is gravitationally bound, $\partial\Phi/\partial z = 0$ at its boundaries and the second term on the right hand side vanishes. From Eqs. 2.14 and 2.15, we find

$$\kappa(\theta) = \frac{1}{2}\triangle_\theta\hat{\Psi} = \frac{1}{2}\frac{\xi_0^2}{D_L^2}\triangle_\theta\Psi . \tag{2.28}$$

Since

$$\triangle_\theta = D_L^2\triangle_\xi = \frac{D_L^2}{\xi_0^2}\triangle_x , \tag{2.29}$$

using adimensional quantities Eq. 2.28 reads

$$\kappa(\vec{x}) = \frac{1}{2}\triangle_x\Psi(\vec{x}) \tag{2.30}$$

Integrating Eq. (2.20), the effective lensing potential can be written in terms of the convergence as

$$\Psi(\vec{x}) = \frac{1}{\pi}\int_{\mathbf{R}^2}\kappa(\vec{x}')\ln|\vec{x} - \vec{x}'|\mathrm{d}^2x' , \tag{2.31}$$

from which we obtain that the scaled deflection angle is

$$\vec{\alpha}(\vec{x}) = \frac{1}{\pi}\int_{\mathbf{R}^2}\mathrm{d}^2x'\kappa(\vec{x}')\frac{\vec{x} - \vec{x}'}{|\vec{x} - \vec{x}'|} . \tag{2.32}$$

2.4 Magnification and distortion

One of the main features of gravitational lensing is the distortion which it introduces into the shape of the sources. This is particularly evident when the source has no negligible apparent size. For example, background galaxies can appear as very long arcs in galaxy clusters.

The distortion arises because light bundles are deflected differentially. Ideally the shape of the images can be determined by solving the lens equation for all the points within the extended source. In particular, if the source is much smaller than the angular size on which the physical properties of the lens change, the relation between source and

Convergence alone

Source
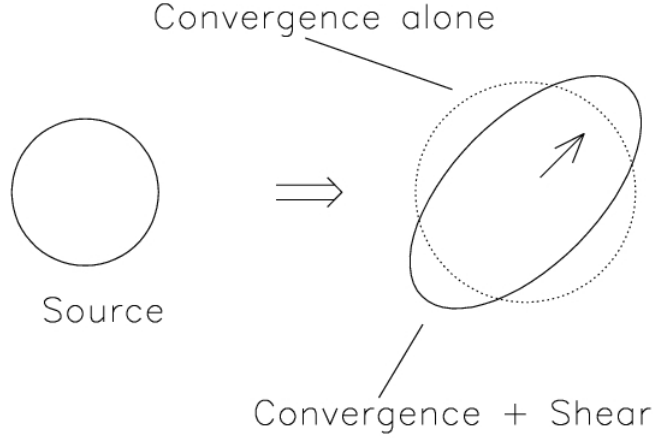
Convergence + Shear

Figure 2.2: Distortion effects due to convergence and shear on a circular source (Figure from Narayan & Bartelmann, 1995).

image positions can locally be linearized. In other words, the distortion of images can be described by the Jacobian matrix

$$A \equiv \frac{\partial \vec{y}}{\partial \vec{x}} = \left(\delta_{ij} - \frac{\partial \alpha_i(\vec{x})}{\partial x_j} \right) = \left(\delta_{ij} - \frac{\partial^2 \Psi(\vec{x})}{\partial x_i \partial x_j} \right) \ , \tag{2.33}$$

where x_i indicates the i-component of $\vec{x}$ on the lens plane. Eq. (2.33) shows that the elements of the Jacobian matrix can be written as combinations of the second derivatives of the lensing potential.

For brevity, we will use the shorthand notation

$$\frac{\partial^2 \Psi(\vec{x})}{\partial x_i \partial x_j} \equiv \Psi_{ij} \ . \tag{2.34}$$

We can now split off an isotropic part from the Jacobian:

$$\left(A - \frac{1}{2} \mathrm{tr} A \cdot I \right)_{ij} = \delta_{ij} - \Psi_{ij} - \frac{1}{2}(1 - \Psi_{11} + 1 - \Psi_{22})\delta_{ij} \tag{2.35}$$

$$= -\Psi_{ij} + \frac{1}{2}(\Psi_{11} + \Psi_{22})\delta_{ij} \tag{2.36}$$

$$= \begin{pmatrix} -\frac{1}{2}(\Psi_{11} - \Psi_{22}) & -\Psi_{12} \\ -\Psi_{12} & \frac{1}{2}(\Psi_{11} - \Psi_{22}) \end{pmatrix} \ . \tag{2.37}$$

This is manifestly an antisymmetric, trace-free matrix is called the shear matrix. It quantifies the projection of the gravitational tidal field (the gradient of the gravitational force), which describes distortions of background sources.

This allows us to define the pseudo-vector $\vec{\gamma} = (\gamma_1, \gamma_2)$ on the lens plane, whose components are

$$\gamma_1(\vec{x}) \quad = \quad \frac{1}{2}(\Psi_{11} - \Psi_{22}) \tag{2.38}$$

$$\gamma_2(\vec{x}) \quad = \quad \Psi_{12} = \Psi_{21} \ , \tag{2.39}$$

This is called the *shear*.

The eigenvalues of the shear matrix are

$$\pm\sqrt{\gamma_1^2 + \gamma_2^2} = \pm\gamma \ . \tag{2.40}$$

Thus, there exists a coordinate rotation by an angle ϕ such that

$$\begin{pmatrix} \gamma_1 & \gamma_2 \\ \gamma_2 & -\gamma_1 \end{pmatrix} = \gamma \begin{pmatrix} \cos 2\phi & \sin 2\phi \\ \sin 2\phi & \cos 2\phi \end{pmatrix} \tag{2.41}$$

> **Remark:**
> Note the factor 2 on the angle ϕ, which reminds that the shear component are elements of a 2×2 tensor and not a vector.

The remainder of the Jacobian is

$$\frac{1}{2}\mathrm{tr}A \quad = \quad \left[1 - \frac{1}{2}(\Psi_{11} + \Psi_{22})\right]\delta_{ij} \tag{2.42}$$

$$= \quad \left(1 - \frac{1}{2}\triangle\Psi\right)\delta_{ij} = (1 - \kappa)\delta_{ij} \ . \tag{2.43}$$

Thus, the Jacobian matrix becomes

$$A \quad = \quad \begin{pmatrix} 1 - \kappa - \gamma_1 & -\gamma_2 \\ -\gamma_2 & 1 - \kappa + \gamma_1 \end{pmatrix}$$

$$= \quad (1 - \kappa)\begin{pmatrix} 1 & 0 \\ 0 & 1 \end{pmatrix} - \gamma\begin{pmatrix} \cos 2\phi & \sin 2\phi \\ \sin 2\phi & -\cos 2\phi \end{pmatrix} \ . \tag{2.44}$$

The last equation explains the meaning of both convergence and shear. The distortion induced by the convergence is isotropic, i.e. the images are only rescaled by a constant factor in all directions. On the other hand, the shear stretches the intrinsic shape of the source along one privileged direction. For this reason, a circular source, which is small enough compared to the scale of the lens, like that shown in Fig. (2.2) is mapped into an ellipse when κ and γ are both non-zero. The semi-major and -minor axes are

$$a = \frac{r}{1 - \kappa - \gamma} \quad , \quad b = \frac{r}{1 - \kappa + \gamma} \ , \tag{2.45}$$

where r is the radius of the circular source.

An important consequence of the lensing distortion is the magnification. Through the lens equation, the solid angle element $\delta\beta^2$ (or equivalently the surface element δy^2) is mapped into the solid angle $\delta\theta^2$ (or in the surface element δx^2). Since the Liouville theorem and the absence of emission and absorbtion of photons in gravitational light deflection ensure the conservation of the source surface brightness, the change of the solid angle under which the source is seen implies that the flux received from a source is magnified (or demagnified).

Given Eq. (2.33), the *magnification* is quantified by the inverse of the determinant of the Jacobian matrix. For this reason, the matrix $M = A^{-1}$ is called the *magnification tensor*. We therefore define

$$\mu \equiv \det M = \frac{1}{\det A} = \frac{1}{(1 - \kappa)^2 - \gamma^2} \ . \tag{2.46}$$

The eigenvalues of the magnification tensor (or the inverse of the eigenvalues of the Jacobian matrix) measure the amplification in the tangential and in the radial direction and are given by

$$\mu_t = \frac{1}{\lambda_t} = \frac{1}{1 - \kappa - \gamma} \tag{2.47}$$

$$\mu_r = \frac{1}{\lambda_r} = \frac{1}{1 - \kappa + \gamma} \ . \tag{2.48}$$

The magnification is ideally infinite where $\lambda_t = 0$ and where $\lambda_r = 0$. These two conditions define two curves in the lens plane, called the *tangential* and the *radial critical line*, respectively. An image forming along the tangential critical line is strongly distorted tangentially to this line. On the other hand, an image forming close to the radial critical line is stretched in the direction perpendicular to the line itself.

Example: Numerically simulated galaxy cluster

Galaxy clusters are the most massive bound objects in the Universe. They are "young" structures, whose assembling process is still on-going. For this reason they are characterized by an high level of complexity. The luminous matter within them (gas and stars) accounts for $\sim 10\%$ of their mass. The rest is dark matter. Numerical simulations provide the most realistic description of these cosmic structures. N-body and hydrodynamical simulations have been used to simulate the formation and the evolution of systems on different scales. The figure on the left side shows the adimensional surface mass density (or *convergence*) of a cluster-sized dark matter halo simulated at $z \sim 0.3$. The mass of such object is $\sim 10^{15} M_\odot$.
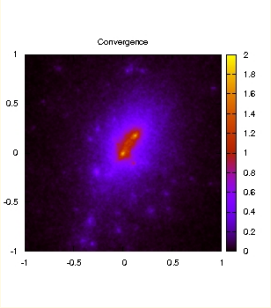
Imagine that a bundle of light rays passes through the mass distribution showed above. Each mass element of the lens contributes to deflect the light coming from background sources. Eq.2.3 allows to calculate the deflection angle at each position $\vec{\xi}$ on the lens plane. The resulting deflection angle field is shown on the right.
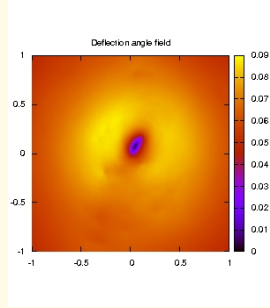
The lensing effect can be decomposed into two terms: the isotropic term given by the convergence and the anisotropic term given by the shear γ. This is a pseudo-vector, whose orientation define the direction into which an image is stretched. All around the cluste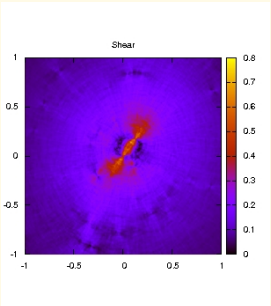r, the shear tends to be tangential to the lens iso-density contours (see the left panel below). Close to the cluster cores, images can be distorted also towards the cluster center. The intensity of γ determines the amplitude of the distortion. The shear pattern for our numerical cluster is shown on the left.

By distorting them, the lens magnifies the sources. Depending on where the sources are located behind the cluster, the resulting magnification is different. In the Figure on the right shown is the magnification on the lens plane (in logarithmic scale!). It is ideally infinite along the so-called *lens critical lines*. The sources generating images around the critical lines are located along the *caustics*. The critical lines and the caustics are shown in the middle and in the right panels below, respectively.
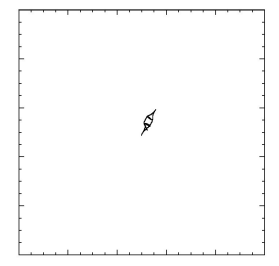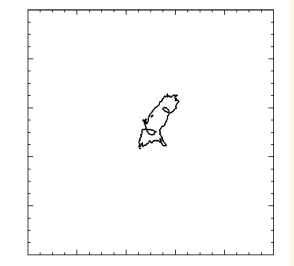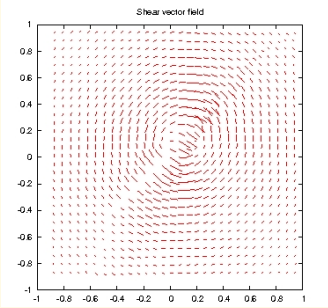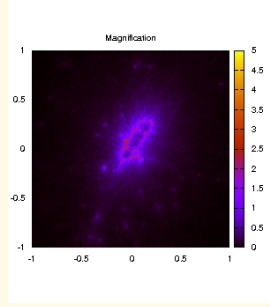
2.5 Lensing to the second order

In section 2.4, we discussed the effects of lensing at the first order. We briefly mention now some second order effects. Using a Taylor expansion around the origin, the unperturbed coordinates can be linked to the perturbed ones through the following equation

$$y_i \simeq \frac{\partial y_i}{\partial x_j} x_j + \frac{1}{2} \frac{\partial^2 y_i}{\partial x_j \partial x_k} x_j x_k \ . \tag{2.49}$$

The lensing effect is described at the first order by the Jacobian matrix A. Now, we introduce the tensor

$$D_{ijk} = \frac{\partial^2 y_i}{\partial x_j \partial x_k} = \frac{\partial A_{ij}}{\partial x_k} \ . \tag{2.50}$$

Then, Eq. 2.49 reads

$$y_i \simeq A_{ij} x_j + \frac{1}{2} D_{ijk} x_j x_k \tag{2.51}$$

By simple algebra, it can be shown that

$$D_{ij1} = \begin{pmatrix} -2\gamma_{1,1} - \gamma_{2,2} & -\gamma_{2,1} \\ -\gamma_{2,1} & -\gamma_{2,2} \end{pmatrix} \ , \tag{2.52}$$

and

$$D_{ij2} = \begin{pmatrix} -\gamma_{2,1} & -\gamma_{2,2} \\ -\gamma_{2,2} & 2\gamma_{1,2} - \gamma_{2,1} \end{pmatrix} \ . \tag{2.53}$$

Thus, the second order lensing effect can be expressed in terms of the derivatives of the shear (or in terms of the third derivatives of the potential).

We can construct the complex quantities

$$F = F_1 + iF_2 = (\gamma_{1,1} + \gamma_{2,2}) + i(\gamma_{2,1} - \gamma_{1,2}) \tag{2.54}$$

and

$$G = G_1 + iG_2 = (\gamma_{1,1} - \gamma_{2,2}) + i(\gamma_{2,1} + \gamma_{1,2}) \tag{2.55}$$

which are called *first and second flexion*, respectively. They describe second order distortions of the images of lensed sources.

The flexion is responsible for introducing a curvature and other anisotropic distortions in the images. An illustration of the effects of first and second flexions on the shape of a circular source is shown in Fig. 2.3.

Note that the vector $\vec{F}$ having components F_1 and F_2 is

$$\vec{F} = \vec{\nabla}\kappa \ . \tag{2.56}$$

Indeed:

$$\gamma_{1,1} = \frac{1}{2}(\Psi_{111} - \Psi_{221}) \tag{2.57}$$

$$\gamma_{2,2} = \Psi_{122} \tag{2.58}$$

$$\gamma_{2,1} = \Psi_{121} \tag{2.59}$$

$$\gamma_{1,2} = \frac{1}{2}(\Psi_{112} - \Psi_{222}) \tag{2.60}$$
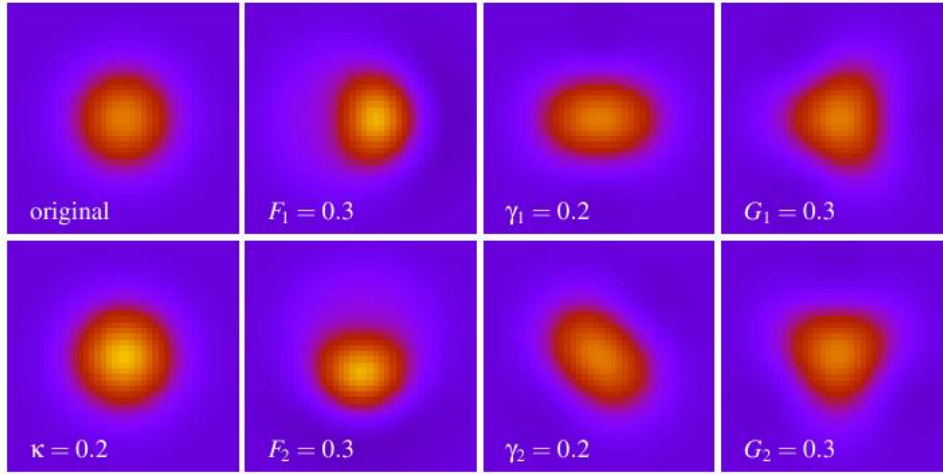
Figure 2.3: First and second order distortions on the image of a circular source. The unlensed source is shown in the top left panel. The convergence simply changes the size (bottom left panel). While the shear deforms the image such that it becomes elliptical (third column of panels from the left), the first and the second flexion introduce curvature and other distortions (second and fourth columns). Courtesy of Peter Melchior.

Therefore:

$$F_1 = \frac{1}{2}(\Psi_{111} - \Psi_{221}) + \Psi_{122} = \frac{1}{2}(\Psi_{111} + \Psi_{221}) = \frac{\partial \kappa}{\partial x_1} \tag{2.61}$$

$$F_2 = \frac{1}{2}(\Psi_{112} - \Psi_{222}) + \Psi_{121} = \frac{1}{2}(\Psi_{112} + \Psi_{222}) = \frac{\partial \kappa}{\partial x_2} . \tag{2.62}$$

This means that the first flexion can be used to obtain the convergence field.

2.6 Occurrence of images

The deflection of light rays causes a delay in the time between the emission of radiation by the source and the signal reception by the observer. This time delay has two components:

$$t = t_{\text{geom}} + t_{\text{grav}} \tag{2.63}$$

The first one has a geometrical reason and is due to the different path length of the deflected light rays compared to the unperturbed ones. This time delay is proportional to the squared angular separation between the intrisic position of the source and the location of its image. The second one comes from the slowing down of photons traveling through the gravitational field of the lens and is therefore related to the lensing potential. Considering a lens at redshift z_{L}, the total time delay introduced by gravitational lensing at the position $\vec{x}$ on the lens plane is

$$t(\vec{x}) = \frac{(1 + z_{\text{L}})}{c} \frac{D_{\text{S}} \xi_0^2}{D_{\text{L}} D_{\text{LS}}} \left[\frac{1}{2}(\vec{x} - \vec{y})^2 - \Psi(\vec{x}) \right] . \tag{2.64}$$
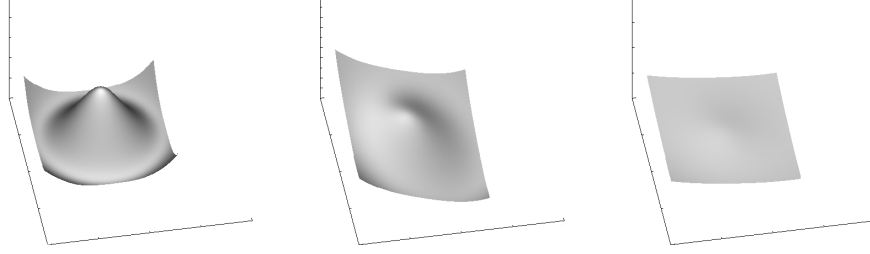
Figure 2.4: Time delay surfaces of an axially symmetric lens for three different source positions. Right panel: source and lens are perfectly aligned along the optical axis; middle panel: the source is no more aligned with the lens. Its projected position on the lens plane is moved along the line $x_1 = x_2$; right panel: the source is moved to an even larger angular distance from the optical axis.

Through the effective lensing potential, the lens equation can be written as

$$(\vec{x} - \vec{y}) - \nabla \Psi(\vec{x}) = \nabla \left[\frac{1}{2}(\vec{x} - \vec{y})^2 - \Psi(\vec{x}) \right] = 0 \ . \tag{2.65}$$

Eqs. (2.64) and (2.65) imply that images satisfy the Fermat Principle, $\nabla t(\vec{x}) = 0$. Images therefore are located at the stationary points of the time delay surface given by Eq. (2.64). The Hessian matrix of this surface is

$$T = \frac{\partial^2 t(\vec{x})}{\partial x_i \partial x_j} \propto (\delta_{ij} - \Psi_{ij}) = A \tag{2.66}$$

We can distinguish between three types of image:

(1) type I images arise at the minima of the time delay surface, where the eigenvalues of the Hessian matrix are both positive, hence $\det A > 0$ and $\mathrm{tr}A > 0$. Therefore, they have positive magnification;

(2) type II images arise at the saddle points of the time delay surface, where eigenvalues have opposite signs. Since $\det A < 0$, they have negative magnification. The interpretation of a negative μ is that the parity of the image is flipped compared to the source;

(3) finally, type III images arise at the maxima of the time delay surface. Here, the eigenvalues are both negative, hence $\det A > 0$ and $\mathrm{tr}A < 0$. These images therefore have positive magnification.

Since the Hessian matrix describes the local curvature of the time delay surface, the smaller is the curvature along one direction at the position where the image forms, the larger is its magnification along the same direction. We display in Fig. (2.4) some examples of the time delay surface for a general axially symmetric lens with core. The density profile of this lens scales with radius as r^{-2} outside the core. The surfaces are plotted for three different source position $\vec{y}$: in the left panel the source and the lens are perfectly aligned along the optical axis passing through the lens center ($\vec{y} = 0$ and $\vec{x} = 0$); in the middle and right panel, the source is moved far away, increasing its angular distance from the optical axis. In order to better see where the minima and the maxima arise, we show in Fig. (2.5) the profile along the line $x_1 = x_2$ of the same
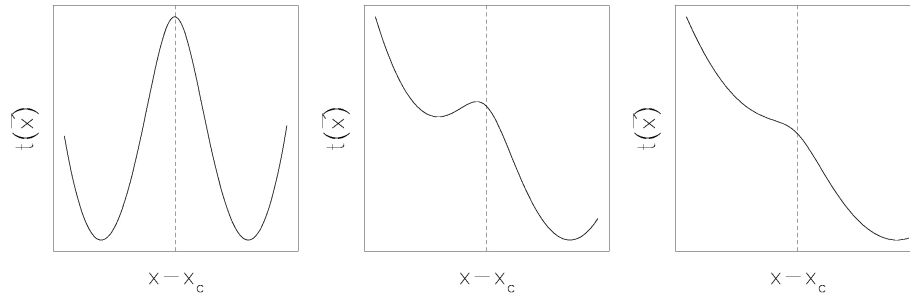
Figure 2.5: Profiles of the time delay surfaces displayed in Fig. (2.4) along the line $x_1 = x_2$.

surfaces. When the source and the lens are perfectly aligned, the minima of the time delay surface are located on a ring and the maximum is at the lens center. The source therefore is mapped to a ring image of type I (the so called *Einstein Ring*) and to a central type III image. This last one is generally demagnified, since the curvature of the time delay surface here is large for density profiles peaked at the lens center.

As the source is moved far away from the optical axis, the time delay surface deforms. In particular, the ring breaks, leading to the formation of a minimum and of a saddle point. Three images therefore arise. In the case displayed in the middle panel of Fig. (2.4), the type I image at the minimum and the type II image at the saddle point are stretched in the tangential direction, since the local curvature of the time delay surface is small in that direction. This explains the formation of tangential arcs in galaxy clusters. However, as the source is moved to even larger angular distances from the optical axis, the saddle point and the maximum move much closer to each other, while the minimum follows the source. The local curvature of the time delay surface in the radial direction becomes smaller between the saddle point and the maximum as they get closer. The images arising at this two points therefore are stretched towards each other. Then a radial image forms. When the saddle point and the maximum point touch, two images disappear and only the image arising at the minimum of the time delay surface remains (see right panels of Fig. (2.4) and Fig. (2.5)).

Here follows a number of other important properties of the time-delay surface:

- the height difference at different images of the surface $t(\vec{x})$ gives the difference in arrival time between these images. This time delay can be measured if the source is variable, and provides one way of potentially measuring the Hubble constant;

- in absence of the lens, the time-delay surface is a parabola which has a single extremum (a minimum); additional extrema have to come in pairs, thus the total number of images must be odd (as we showed earlier by continously deforming the time-delay surface);

- when two additional images are formed, they must be a maximum and a saddle point; in between them, the curvature changes from negative to positive, thus it is zero between them; remember that $\det A = 0$ is the condition for having a critical point, where the magnification is (formally) infinite. The critical lines thus separate multiple-image pairs; these pairs merge and desappear (as discussed above) at the critical lines. In other words, the critical lines separate regions of different image multiplicities.

Example: Determination of the Hubble Constant

The lens equation is dimensionless, and the positions of images as well as their magnifications are dimensionless numbers. Therefore, information on the image configuration alone does not provide any constraint on the overall scale of the lens geometry or the value of the Hubble constant. Refsdal 1964 realized that the time delay, however, is proportional to the absolute scale of the system and does depend on H_0.

To see this, we first note that the geometrical time delay is simply proportional to the path lengths of the rays which scale as H_0^{-1}. The gravitational time delay also scales as H_0^{-1} because the linear size of the lens and its mass have this scaling. Therefore for any gravitational lens system, the quantity

$$H_0 \Delta t$$

depends only on the lens model and the geometry of the system. A good lens model which reproduces the positions and magnifications of the images provides the scaled time delay $H_0 \Delta t$ between the images. Therefore, a measurement of the time delay Δt will yield the Hubble constant H_0.

As an example, we summarize here the results of Koopmans et al. (2003). They analyse the lens system B1608+656, a quadruply-imaged QSO at reshift $z_S = 1.39$ lensed by two lens galaxies at redshift $z_L = 0.63$ (see Fig. on the right side). For this system very accurate determinations of the time delays between the different images were obtained by Fassnacht et al. (2002), by monitoring the VLA radio fluxes of the four images. Labelling the images from A to D, the time-delays with respect to the image B were found to be $\Delta t_{AB} = 31.5 \pm 1.5$, $\Delta t_{CB} = 36 \pm 1.5$ and $\Delta t_{DB} = 77 \pm 1.5$ (days).
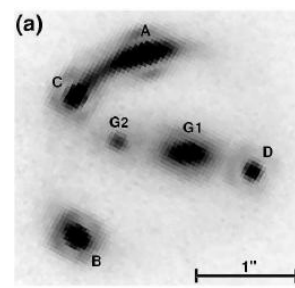
By combining several radio, optical, infrared observations plus some constraints on the dynamics of stars in the main lens galaxy (G1), Koopmans et al. were able to construct a detailed model of the lens system, and to reconstruct the shape of the time-delay surface.
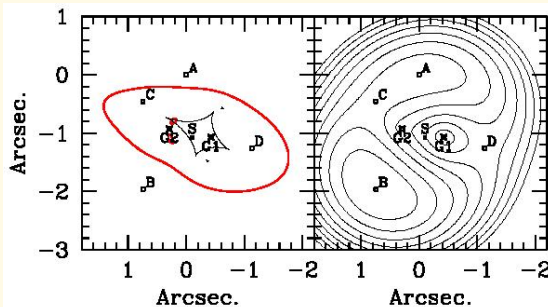
The lens critical lines (in red) and caustics (in black) are shown in the left panel, the contours of constant time-delay on the right. They start at $\Delta t = 0$ at image B and increase in steps of $10h^{-1}$ days. As expected, images B and A correspond to minima of the time-delay surface. Image C and D are located at two saddle points, instead.

Finally, a maximum falls onto the galaxy G1, where no images of the source QSO are seen. For this galaxy, the lens model predicts a very large inner slope of its density profile. Consequently, the local curvature of the time-delay surface is very large. Thus, the image which should form at this position is strongly de-magnified. The light of the lens galaxy also prevents to observe such image. Note that the critical lines pass between the saddle and the minimal points.

Using this lens model, Koopmans et al. estimate the Hubble constant to be $H_0 = 75^{+7}_{-6}$ km s^{-1} Mpc^{-1}.

3 Lens models

One of the main goals of lensing theory is to determine which combinations of lenses and sources can reproduce a particular image configuration. For solving this kind of problem, it is very common to use analytic lens models. These models have the advantage that they are very simple and their lensing properties can be derived quite easily.

A variety of models exists, which are more ore less reliable for describing lensing on different scales. Compact objects like planets, stars, black holes or the so called Massive Astrophysical Compact Halo Objects (MACHOs) are usually well aproximated by point lenses. The most simple models which are used in studies of extended lenses are the axially symmetric models. However, they are not sufficiently realistic for describing the majority of astrophysical objects, and elliptical models turn out to be much more appropriate in most cases.

3.1   Point masses

Let us begin with point masses as lenses. The deflection angle of a point mass was

$$\hat{\vec{\alpha}} = -\frac{4GM}{c^2 b}\,\vec{e}_r \;, \tag{3.1}$$

where $\vec{e}_r$ is the unit vector in radial direction. No direction is prefered in an axisymmetric situation like that, so we can identify $\vec{e}_r$ with one coordinate axis and thus reduce the problem to one dimension. Then

$$\hat{\alpha} = \frac{4GM}{c^2 b} = \frac{4GM}{c^2 D_\mathsf{L} \theta} \;, \tag{3.2}$$

where we have expressed the impact parameter by the angle θ, $b = D_\mathsf{L}\theta$.

The lensing potential is given by

$$\hat{\Psi} = \frac{4GM}{c^2}\frac{D_\mathsf{LS}}{D_\mathsf{L} D_\mathsf{S}}\,\ln|\vec{\theta}| \;, \tag{3.3}$$

as one can show using

$$\nabla \ln|\vec{x}| = \frac{\vec{x}}{|\vec{x}|^2} \;. \tag{3.4}$$

The lens equation reads

$$\beta = \theta - \frac{4GM}{c^2 D_\mathsf{L}\theta}\frac{D_\mathsf{LS}}{D_\mathsf{S}} \;. \tag{3.5}$$

With the definition of the Einstein radius,

$$\theta_E \equiv \sqrt{\frac{4GM}{c^2}\frac{D_{\mathsf{LS}}}{D_{\mathsf{L}}D_{\mathsf{S}}}} \ , \tag{3.6}$$

we have

$$\beta = \theta - \frac{\theta_E^2}{\theta} \ . \tag{3.7}$$

Dividing by θ_E and setting $y = \beta/\theta_E$ and $x = \theta/\theta_E$, the lens equation in its adimensional form is written as

$$y = x - \frac{1}{x} \tag{3.8}$$

Multiplication with x leads to

$$x^2 - xy - 1 = 0 \ , \tag{3.9}$$

which has two solutions:

$$x_\pm = \frac{1}{2}\left[y \pm \sqrt{y^2 - 4}\right] \ . \tag{3.10}$$
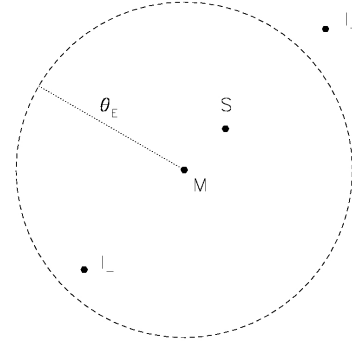
Thus, a point-mass lens has two images for any source, irrespective of its distance y from the lens. Why not three? Because its mass is singular and thus the time-delay surface is not continously deformed.

If $y = 0$, $x_\pm = \pm 1$; that is, a source directly behind the point lens has a ring-shaped image with radius θ_E. For order-of-magnitude estimates:

$$\begin{aligned}
\theta_E &\approx (10^{-3})'' \left(\frac{M}{M_\odot}\right)^{1/2}\left(\frac{D}{10\mathrm{kpc}}\right)^{-1/2} \ , \\
&\approx 1'' \left(\frac{M}{10^{12}M_\odot}\right)^{1/2}\left(\frac{D}{\mathrm{Gpc}}\right)^{-1/2} \ , \tag{3.11}
\end{aligned}$$

where

$$D \equiv \frac{D_{\mathsf{L}}D_{\mathsf{S}}}{D_{\mathsf{LS}}} \tag{3.12}$$

is called *effective lensing distance*.

As $\beta \to \infty$, we see that $\theta_- = x_-\theta_E \to 0$, while obviously $\theta_+ = x_+\theta_E \to \beta$: when the angular separation between the lens and the source becomes large, the source is unlensed. Formally, there is still an image at $\theta_- = 0$.

The magnifications follow from from the Jacobian. For any axially-symmetric lens,

$$\begin{aligned}
\det A &= \frac{y}{x}\frac{\partial y}{\partial x} = \left(1 - \frac{\alpha}{x}\right)\left(1 - \frac{\partial\alpha}{\partial x}\right) \\
&= \left(1 - \frac{1}{x^2}\right)\left(1 + \frac{1}{x^2}\right) = 1 - \left(\frac{1}{x}\right)^4 \\
&\Rightarrow \mu = \left[1 - \left(\frac{1}{x}\right)^4\right]^{-1} \ , \tag{3.13}
\end{aligned}$$

i.e. a source at $y = 1$ has two images at

$$x_\pm = \frac{1 \pm \sqrt{5}}{2} \ , \tag{3.14}$$

and their magnifications are

$$\mu_\pm = \left[1 - \left(\frac{2}{1 \pm \sqrt{5}} \right)^4 \right]^{-1} \ . \tag{3.15}$$

For general source positions,

$$\begin{aligned} \mu_\pm &= \left[1 - \left(\frac{1}{x_\pm} \right)^4 \right]^{-1} \\ &= \frac{x_\pm^4}{x_\pm^4 - 1} = \frac{1}{2} \pm \frac{y^2 + 2}{2y\sqrt{y^2 + 4}} \ . \end{aligned} \tag{3.16}$$

Note that $\lim_{y \to \infty} \mu_- = 0$ and that $\lim_{y \to \infty} \mu_+ = 1$: even if the lens equation has always two solutions, for large angular separations between the source and the lens, one image desappears because it is demagnified. The other is completely undistiguishable from the source because it has the same flux and the same position.

The total magnification of a point source by a point mass is thus

$$\mu = |\mu_+| + |\mu_-| = \frac{y^2 + 2}{y\sqrt{y^2 + 4}} \ , \tag{3.17}$$

and the magnification ratio of the two images is

$$\left| \frac{\mu_-}{\mu_+} \right| = \left(\frac{y - \sqrt{y^2 + 4}}{y + \sqrt{y^2 + 4}} \right)^2 = \left(\frac{x_-}{x_+} \right)^2 \ . \tag{3.18}$$

If $\beta = \theta_E$, $y = 1$ and the total magnification is $\mu = 1.17 + 0.17 = 1.34$. In terms of magnitudes, this correspond to $\Delta m = -2.5 \log \mu \sim 0.3$. The image forming at x_+ contributes for $\sim 87\%$ of the total magnification.

Lensing by point masses on point sources will be discussed in detail in a following chapter. However, we can already answer to the question: how can lensing by a point mass be detected? Unless the lens is more massive than $10^6 \, M_\odot$ (for a source at cosmological distance), the angular separation between multiple images is too small to be resolved. However, the magnification effect will be detectable in many cases if the source is moving relative to the lens (for example, a star in the large magellanic cloud is in relative motion with respect to a star in the halo of our galaxy). Thus, since the magnification changes as a function of the angular separation between source and lens, the lensing effect will induce a time variability in the light curve of the source.

3.2 Axially symmetric lenses

The main advantage of using axially symmetric lenses is that their surface density is independent on the position angle with respect to lens center. If we choose the optical axis such that it intercepts the lens plane in the lens center, this implies that $\Sigma(\vec{\xi}) = \Sigma(|\vec{\xi}|)$. The lensing equations therefore reduce to a one-dimensional form, since all the light rays from a (point) source lie on the same plane passing through the center of the lens, the source and the observer.

The deflection angle for an axially symmetric lens was found to be

$$\hat{\alpha}(\xi) = \frac{4GM(\xi)}{c^2\xi} \ .$$
(3.19)

If want to use adimensional quantities:

$$
\begin{aligned}
\alpha(x) &= \frac{D_{\mathrm{L}}D_{\mathrm{LS}}}{\xi_0 D_{\mathrm{S}}} \hat{\alpha}(\xi_0 x) \\
&= \frac{D_{\mathrm{L}}D_{\mathrm{LS}}}{\xi_0 D_{\mathrm{S}}} \frac{4GM(\xi_0 x)}{c^2\xi} \frac{\pi\xi_0}{\pi\xi_0} \\
&= \frac{M(\xi_0 x)}{\pi\xi_0^2 \Sigma_{\mathrm{cr}}} \frac{1}{x} \equiv \frac{m(x)}{x} \ ,
\end{aligned}
$$
(3.20)

where we have introduced the *dimensionless mass* $m(x)$. Note that

$$\alpha(x) = \frac{2}{x} \int_0^x x' \kappa(x') \mathrm{d}x' \Rightarrow m(x) = 2 \int_0^x x' \kappa(x') \mathrm{d}x' \ .$$
(3.21)

The lens equation (2.9) then becomes

$$y = x - \frac{m(x)}{x} \ .$$
(3.22)

Now, we derive formulas for several lensing quantities. To do that, we need to write the deflection angle as a vector. For an axially symmetric lens, the deflection angle points towards the lens center. Then,

$$\vec{\alpha}(\vec{x}) = \frac{m(\vec{x})}{x^2} \vec{x} \ ,$$
(3.23)

where $\vec{x} = (x_1, x_2)$.

By differentiating we obtain:

$$\frac{\partial\alpha_1}{\partial x_1} = \frac{\mathrm{d}m}{\mathrm{d}x} \frac{x_1^2}{x^3} + m \frac{x_2^2 - x_1^2}{x^4} \ ,$$
(3.24)

$$\frac{\partial\alpha_2}{\partial x_2} = \frac{\mathrm{d}m}{\mathrm{d}x} \frac{x_2^2}{x^3} + m \frac{x_1^2 - x_2^2}{x^4} \ ,$$
(3.25)

$$\frac{\partial\alpha_1}{\partial x_2} = \frac{\partial\alpha_2}{\partial x_1} = \frac{\mathrm{d}m}{\mathrm{d}x} \frac{x_1 x_2}{x^3} - 2m \frac{x_1 x_2}{x^4} \ ,$$
(3.26)

which immediately give the elements of the Jacobian matrix:

$$
\begin{aligned}
A =\ & I - \frac{m(x)}{x^4} \begin{pmatrix} x_2^2 - x_1^2 & -2x_1 x_2 \\ -2x_1 x_2 & x_1^2 - x_2^2 \end{pmatrix} \\
& - \frac{\mathrm{d}m(x)}{\mathrm{d}x} \frac{1}{x^3} \begin{pmatrix} x_1^2 & x_1 x_2 \\ x_1 x_2 & x_2^2 \end{pmatrix} \ .
\end{aligned}
$$
(3.27)

This permits us to obtain the following expressions for the convergence and the shear components:

$$\kappa(x) = \frac{1}{2x} \frac{\mathrm{d}m(x)}{\mathrm{d}x} \ ,$$
(3.28)

$$\gamma_1(x) = \frac{1}{2}(x_2^2 - x_1^2)\left(\frac{2m(x)}{x^4} - \frac{\mathrm{d}m(x)}{\mathrm{d}x}\frac{1}{x^3}\right) \ ,$$
(3.29)

$$\gamma_2(x) = x_1 x_2 \left(\frac{\mathrm{d}m(x)}{\mathrm{d}x}\frac{1}{x^3} - \frac{2m(x)}{x^4}\right) \ .$$
(3.30)

From these relations,

$$\gamma(x) = \frac{m(x)}{x^2} - \kappa(x) \ . \tag{3.31}$$

Since $m(x) = 2 \int_0^x x' \kappa(x') \mathrm{d}x'$, we see that

$$\frac{m(x)}{x^2} = 2\pi \frac{\int_0^x x' \kappa(x') \mathrm{d}x'}{\pi x^2} = \overline{\kappa}(x) \ . \tag{3.32}$$

where $\overline{\kappa}(x) = m(x)/x^2$ is the *mean surface mass density* within x. Eq. 3.31 then reduces to

$$\gamma(x) = \overline{\kappa}(x) - \kappa(x) \tag{3.33}$$

The Jacobian determinant of the lens mapping is

$$
\begin{aligned}
\det A &= \frac{y}{x}\frac{\mathrm{d}y}{\mathrm{d}x} = \left(1 - \frac{m(x)}{x^2}\right)\left[1 - \frac{\mathrm{d}}{\mathrm{d}x}\left(\frac{m(x)}{x}\right)\right] \\
&= \left(1 - \frac{m(x)}{x^2}\right)\left(1 + \frac{m(x)}{x^2} - 2\kappa(x)\right) \\
&= \left(1 - \frac{\alpha(x)}{x}\right)\left(1 - \frac{\mathrm{d}\alpha(x)}{\mathrm{d}x}\right) \ .
\end{aligned}
\tag{3.34}
$$

Since the critical lines arise where $\det A = 0$, Eq. (3.34) implies that axially symmetric lenses with monotonically increasing $m(x)$ have at most two critical lines, where $m(x)/x^2 = 1$ and $\mathrm{d}(m(x)/x)/\mathrm{d}x = \mathrm{d}y/\mathrm{d}x = 1$. Both these conditions define circles on the lens plane (see Fig. 3.1). The critical line along which $m(x)/x^2 = 1$ is the tangential one: any vector which is tangential to this line is an eigenvector with zero eigenvalue of the Jacobian matrix. On the other hand, given that any vector perpendicular to the critical line where $\mathrm{d}(m(x)/x)/\mathrm{d}x = 1$ is also an eigenvector with zero eigenvalue, this line is the radial critical line.

From the lens equation it can be easily seen that all the points along the tangential critical line are mapped on the point $y = 0$ on the source plane. Indeed:

$$y = x\left(1 - \frac{m}{x^2}\right) = 0 \ . \tag{3.35}$$

if x indicates a tangential critical point. Therefore, axially symmetric models have point tangential caustics. On the other hand, the points along the radial critical line are mapped onto a circular caustic on the source plane.

As discussed previously, if the lens is strong, multiple images can be formed of the same source. The number of these images depends on the position of the source with respect to the caustics. Sources which lie within the radial caustic produce three images. Sources outside the radial caustic have only one image. This is shown in Fig. 3.1. Since the tangential critical curve does not lead to a caustic curve, but the corresponding caustic degenerates to a single point $\vec{y} = 0$, the tangential critical curves have no influence on the image multiplicity. Thus, pairs of images can only be created or destroyed if the radial critical curve exists. For axially symmetric lenses, it can be shown that the necessary conditions for them to produce multiple images are (Schneider et al., 1992):

(1) at least at one point $1 - 2\kappa(x) + \overline{\kappa}(x) < 0$: if $1 - 2\kappa(x) + \overline{\kappa}(x) > 0$ throughout, a lens produces no multiple images, since $y(x)$ increases monotonically. If on
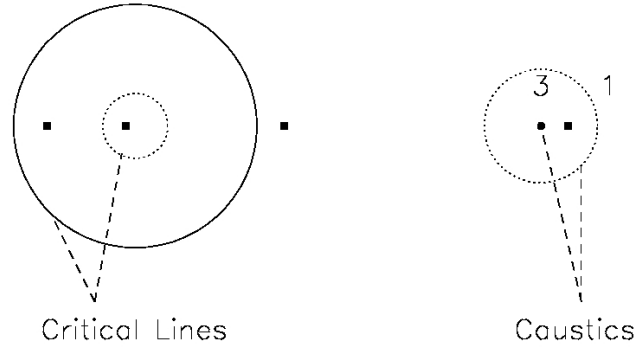
Figure 3.1: Imaging of a point source by a non-singular, circularly-symmetric lens. Left: image positions and critical lines; right: source position and corresponding caustics. From Narayan & Bartelmann (1995).

the other hand, there is a point where $\mathrm{d}y/\mathrm{d}x < 0$, there is at least one local maximum x_1 and one local minimum $x_2 > x_1$ of the curve $y(x)$ since $\mathrm{d}y/\mathrm{d}x \to 1$ for $|x| \to \infty$. For values of y such that $y(x_2) < y < y(x_1)$, there are at least three images;

(2) $\kappa > 1/2$ at one point in the lens: if $\mathrm{d}y/\mathrm{d}x < 0$ at one point, then $\kappa > (1+\overline{\kappa})/2 \geq 1/2$; a sufficient condition for multiple imaging is that $\kappa > 1$ at one point. Indeed: if κ have a a maximum at one point x_m where $\kappa(x_m) > 1$, then $\overline{\kappa}(x_m) \leq \kappa(x_m)$ and $\mathrm{d}y/\mathrm{d}x < 0$ at x_m. The statement then follows from (1);

(3) if the surface density does not increase with x, $\kappa'(x) \leq 0$, $\kappa(0) > 1$: from (2) we know that it is sufficient that $\kappa > 1$ at one point for having multiple images. On the other hand if $\kappa(0) \leq 1$, then, since $y = x(1 - \overline{\kappa})$, we have for $x \geq 0$: $\mathrm{d}y/\mathrm{d}x = (1 - \overline{\kappa}) - x\overline{\kappa}'$. Since

$$\overline{\kappa}(x) = 2 \int_0^1 \mathrm{d}u\, u \kappa(ux) \,, \tag{3.36}$$

then

$$\frac{\mathrm{d}\overline{\kappa}}{\mathrm{d}x} = 2 \int_0^1 \mathrm{d}u\, u^2 \kappa'(ux) \leq 0 \tag{3.37}$$

and $\overline{\kappa}(x) \leq \kappa(0) \leq 1$, we see that $\mathrm{d}y/\mathrm{d}x \geq 0$, so that no multiple images can occur.

Images are in odd numbers. A special case is that of singular lenses, i.e. lenses with infinite density at the center: in this case only two images arise when the source is within
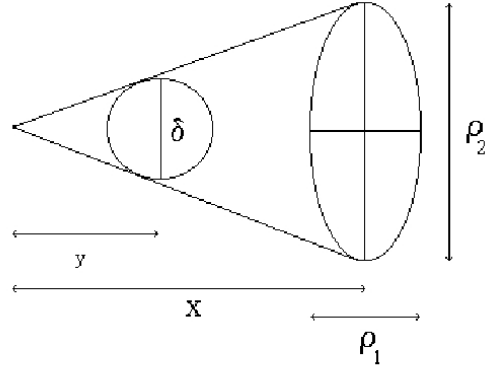
Figure 3.2: Sketch of the mapping of an infinitesimal circular source onto an elliptical image (Figure from Schneider et al., 1992).

the radial caustic. This is clear from the discussion in Sect. (2.6): when the singularity is present, the central maximum of the time delay surface is suppressed. Therefore one possible image is missed.

As was pointed out in the previous chapter, the eigenvalues of the Jacobian matrix give the inverse magnification of the image along the tangential and radial directions. Fig. (3.2) illustrates an infinitesimal source of diameter δ at position y and its image, which is an ellipse, whose minor and major axes are ρ_1 and ρ_2 respectively, at position x. With respect to the origin of the reference frame on the source plane, the circular source subtends an angle $\phi = \delta/y$. Due to the axial symmetry of the lens, $\phi = \rho_2/x$. Using the lens equation, we thus obtain

$$\frac{\delta}{\rho_2} = 1 - \frac{m(x)}{x^2} \ . \tag{3.38}$$

The lens mapping gives $\delta = \rho_1(\mathrm{d}y/\mathrm{d}x)$, from which

$$\frac{\delta}{\rho_1} = 1 + \frac{m(x)}{x^2} - 2\kappa(x) \tag{3.39}$$

This means that the image is stretched in the tangential direction by a factor $[1 - m(x)/x^2]^{-1}$ and in the radial direction by $[1 + m(x)/x^2 - 2\kappa(x)]^{-1}$.

Such distortions are more evident is the sources are extended. Fig. 3.3 shows the images of two extended sources lensed by the same model as in Fig. 3.1. One source is located close to the point-like caustic in the center of the lens. It is imaged onto the two long, tangentially oriented arcs close to the outer critical curve and the very faint image at the lens center. The other source is located on the outer caustic and forms a radially elongated image which is composed of two merging images, and a third tangentially oriented image outside the outer critical line.

3.2.1 Singular Isothermal Sphere

One of the most widely used axially symmetric model is the Singular Isothermal Sphere (SIS hereafter). The density profile of this model can be derived assuming that the
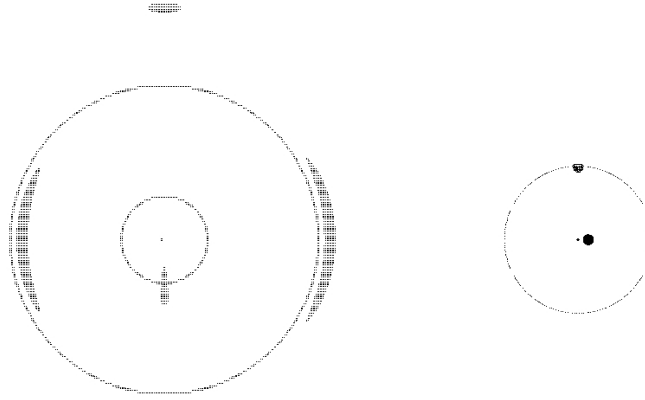
Figure 3.3: Imaging of an extended source by a non-singular circularly-symmetric lens. A source close to the point caustic at the lens center produces two tangentially oriented arc-like images close to the outer critical curve, and a faint image at the lens center. A source on the outer caustic produces a radially elongated image on the inner critical curve, and a tangentially oriented image outside the outer critical curve. From Narayan & Bartelmann (1995).

matter content of the lens behaves as an ideal gas confined by a spherically symmetric gravitational potential. This gas is taken to be in thermal and hydrostatic equilibrium. One of the two density profiles satisfying these sets of equations is given by

$$\rho(r) = \frac{\sigma_v^2}{2\pi G r^2} \ , \tag{3.40}$$

where σ_v is the velocity dispersion of the "gas" particles and r is the distance from the sphere center. By projecting the three-dimensional density along the line of sight, we obtain the corresponding surface density

$$
\begin{aligned}
\Sigma(\xi) &= 2\frac{\sigma_v^2}{2\pi G} \int_0^\infty \frac{\mathrm{d}z}{\xi^2 + z^2} \\
&= \frac{\sigma_v^2}{\pi G} \frac{1}{\xi} \left[\arctan \frac{z}{\xi} \right]_0^\infty \\
&= \frac{\sigma_v^2}{2G\xi} \ .
\end{aligned}
\tag{3.41}
$$

This density profile has a singularity at $\xi = 0$, where the density is ideally infinite. Nevertheless, it has been used to describe the matter distribution in galaxies, expecially because it can reproduce the flat rotation curves of spiral galaxies.

By choosing

$$\xi_0 = 4\pi \left(\frac{\sigma_v}{c}\right)^2 \frac{D_\mathsf{L} D_\mathsf{LS}}{D_\mathsf{S}} \tag{3.42}$$

as the length scale on the lens plane, we obtain:

$$\Sigma(x) = \frac{\sigma_v^2}{2G\xi}\frac{\xi_0}{\xi_0} = \frac{1}{2x}\frac{c^2}{4\pi G}\frac{D_\mathsf{S}}{D_\mathsf{L} D_\mathsf{LS}} = \frac{1}{2x}\Sigma_{\mathrm{cr}} \ . \tag{3.43}$$

Thus, the convergence for the singular isothermal profile is

$$\kappa(x) = \frac{1}{2x} \ , \tag{3.44}$$

and the lensing potential (2.15) is

$$\Psi(x) = |x| \ . \tag{3.45}$$

Using Eqs. (2.16), we obtain

$$\alpha(x) = \frac{x}{|x|} \ , \tag{3.46}$$

and the lens equation reads

$$y = x - \frac{x}{|x|} \ . \tag{3.47}$$

If $y < 1$, two solutions of the lens equation exist. They arise at $x = y - 1$ and $x = y + 1$, on opposite sides of the lens center. The corresponding angular positions of the images are

$$\theta_\pm = \beta \pm \theta_E \tag{3.48}$$

where θ_E is the *Einstein radius*, defined now as

$$\theta_E = \sqrt{\frac{4GM(\theta_E)}{c^2}\frac{D_\mathsf{LS}}{D_\mathsf{L} D_\mathsf{S}}} \ . \tag{3.49}$$

The quantity $M(\theta_E)$ is the mass within the Einstein radius. The angular separation between the two images therefore is $\Delta(\theta) = 2\theta_E$: the Einstein radius defines a typical scale for separation between multiple images.

On the other hand, if $y > 1$, Eq. (3.47) has a unique solution, $x = y + 1$. Images arising at $x > 0$ are of type I (positive parity), while those arising at $x < 0$ are of type II (negative parity).

The shear follows from the derivatives of Ψ. Since

$$\frac{\partial\Psi}{\partial x_i} = \frac{x_i}{|x|} \tag{3.50}$$

we have

$$\frac{\partial\Psi}{\partial x_i \partial x_j} = \frac{\delta_{ij}x - x_i x_j/x}{x^2} = \frac{\delta_{ij}x^2 - x_i x_j}{x^3} \ , \tag{3.51}$$

and thus

$$\Psi_{11} = \frac{x^2 - x_1^2}{x^3} = \frac{x_2^2}{x^3} \tag{3.52}$$

$$\Psi_{12} = -\frac{x_1 x_2}{x^3} \tag{3.53}$$

$$\Psi_{22} = \frac{x^2 - x_2^2}{x^3} = \frac{x_1^2}{x^3} \ . \tag{3.54}$$

The shear components are

$$\gamma_1 = \frac{1}{2}(\Psi_{11} - \Psi_{22}) = \frac{1}{2}\frac{x_2^2 - x_1^2}{x^3} = \frac{1}{2}\frac{\sin^2 \phi - \cos^2 \phi}{x} = -\frac{1}{2}\frac{\cos 2\phi}{x} \ , \tag{3.55}$$

$$\gamma_2 = \Psi_{12} = -\frac{\cos \phi \sin \phi}{x} = -\frac{1}{2}\frac{\sin 2\phi}{x} \ . \tag{3.56}$$

Thus,

$$\gamma(x) = (\gamma_1^2 + \gamma_2^2)^{1/2} = \frac{1}{2x} = \kappa(x) \ . \tag{3.57}$$

From Eq. (3.47), the magnification as a function of the image position is given by

$$\mu = \frac{|x|}{|x| - 1} \ . \tag{3.58}$$

Images are only magnified in the tangential direction, since the radial eigenvalue of the Jacobian matrix is unity everywhere.

If $y < 1$, the magnifications of the two images are

$$\mu_+ = \frac{y+1}{y} = 1 + \frac{1}{y} \quad ; \quad \mu_- = \frac{|y-1|}{|y-1| - 1} = \frac{-y+1}{-y} = 1 - \frac{1}{y} \ , \tag{3.59}$$

from which we see that for $y \to 1$, the second image becomes weaker and weaker until it disappears at $y = 1$. On the other hand, for $y \to \infty$, the source magnification obviously tends to unity: sources which are at large distance from the lens can only be weakly magnified by gravitational lensing.

3.2.2   Softened Isothermal Sphere

The singular isothermal sphere produces only two images of a background point source, because the time-delay surface is not continously deformed due to the the singularity in the lensing mass distribution. The singularity can be avoided by intoducing a core radius, x_c, into the potential,

$$\Psi = \sqrt{x^2 + x_c^2} \ . \tag{3.60}$$

Then, the deflection angle is

$$\vec{\alpha}(\vec{x}) = \frac{\vec{x}}{\sqrt{x^2 + x_c^2}} \ , \tag{3.61}$$

and convergence and shear turn out to be

$$\kappa = \frac{x^2 + 2x_c^2}{2(x^2 + x_c^2)^{3/2}} \tag{3.62}$$

$$\gamma_1 = -\frac{x^2}{2(x^2 + x_c^2)^{3/2}} \cos 2\phi \tag{3.63}$$

$$\gamma_2 = -\frac{x^2}{2(x^2 + x_c^2)^{3/2}} \sin 2\phi \tag{3.64}$$

3.2.3 The Navarro-Frenk & White density profile

Navarro et al. (1997) (NFW hereafter) found that the density profile of dark matter halos numerically simulated in the framework of CDM cosmogony can be very well described by the radial function

$$\rho(r) = \frac{\rho_s}{(r/r_s)(1 + r/r_s)^2} \; , \tag{3.65}$$

within the wide mass range $3 \times 10^{11} \lesssim M_{vir}/(h^{-1}M_{\odot}) \lesssim 3 \times 10^{15}$. The logarithmic slope of this density profile changes from -1 at the center to -3 at large radii. Therefore, it is flatter than that of the SIS in the inner part of the halo, and steeper in the outer part. The two parameters r_s and ρ_s are the scale radius and the characteristic density of the halo.

NFW parameterized dark matter halos by their masses M_{200}, i.e. the masses enclosed in spheres with radius r_{200} in which the average density is 200 times the critical density. The relationship between M_{200} and r_{200} is given by

$$r_{200} = 1.63 \times 10^{-2} \left(\frac{M_{200}}{h^{-1}M_{\odot}} \right)^{1/3} \left[\frac{\Omega_0}{\Omega(z)} \right]^{-1/3} (1+z)^{-1} h^{-1} \text{ kpc} . \tag{3.66}$$

This definition depends on the redshift z at which the halo is identified as well as on the background cosmological model.

From the former definition of r_{200}, the *concentration*, $c \equiv r_{200}/r_s$, and the characteristic density are linked by the relation,

$$\rho_s = \frac{200}{3} \rho_{\text{cr}} \frac{c^3}{[\ln(1+c) - c/(1+c)]} \; . \tag{3.67}$$

Numerical simulations show that the scale radii of dark matter halos at any redshift z systematically change with mass in such a way that concentration is a characteristic function of M_{200}.

Several algorithms have been suggested for describing the concentration of dark matter halos. They are all based on the assumption that the central density of a halo reflects the mean cosmic density at the time when the halo formed. This is justified by numerical simulations of structure formation, which show that halos are the more concentrated the earlier they form. Originally, NFW devised the following approach. Each halo is assigned a collapse redshift, defined as the redshift at which half of the halo mass is contained in progenitors more massive than a fraction f_{NFW} of the final mass. Then, the characteristic density is taken to be some factor C times the mean cosmic density at the collapse redshift. For fitting the results of their numerical simulations, they use $f_{\text{NFW}} = 0.01$ and $C = 3 \times 10^3$.

Bullock et al. (2001) suggested a different definition, because they noticed that the concentrations of numerically simulated dark matter halos change more rapidly with redshift than predicted by the NFW approach. They define the collapse redshift such that the non-linear mass scale at that redshift is a fraction f_{B} of the final halo mass. The halo concentration is then assumed to be a factor K times the ratio of the scale factors at the redshift when the halo is identified and at the collapse redshift. The best fitting values they found when comparing to numerical simulations are $f_{\text{B}} = 0.01$ and $K = 4$.

Finally, Eke et al. (2001) suggested another different approach. The collapse redshift of a halo of mass M is defined such that the suitably defined amplitude of the linearly evolving power spectrum at the mass scale M matches a constant C_{E}^{-1}. The halo concentration is then obtained by setting the characteristic density equal to the spherical
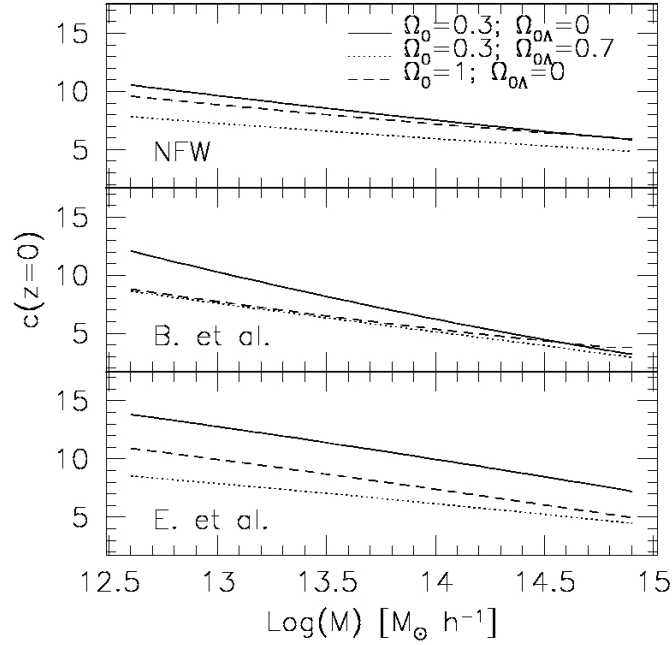
Figure 3.4: Halo concentration parameters as function of halo masses M_{200}. Results obtained for three different approaches for calculating the concentration are shown; these are the approaches by Navarro, Frenk & White (NFW; top panel), by Bullock et al. (B. et al.; middle panel) and by Eke et al. (E. et al.; bottom panel). In each panel we show the curves for a low-density OCDM model ($\Omega_0 = 0.3$, $\Omega_{0\Lambda} = 0$; solid lines), for a flat low-density ΛCDM model ($\Omega_0 = 0.3$, $\Omega_{0\Lambda} = 0.7$; dotted lines) and for a SCDM model ($\Omega_0 = 1$, $\Omega_{0\Lambda} = 0$; dashed lines).

collapse density at the collapse epoch. Numerical results are well represented assuming $C_E = 28$.

The mass-dependence of the concentration parameter c is shown in Fig. (3.4) for all the definitions of halo concentration discussed before and for different cosmological models. The main features of these plots can be summarized as follows:

- although halo concentrations produced by these different algorithms differ in detail, they have in common that the concentration increases toward lower masses in all the cosmological models considered. This is a direct result of the higher collapse redshift of less massive systems;

- the concentration depends on cosmology. The collapse redshift is determined by Ω_0 and $\Omega_{0\Lambda}$: halos form earlier in open low-density universes, then in flat low-density universes and later in flat high-density universes. The concentration thus reflects the mean cosmic density at the time when they collapse. For example, halos in an OCDM model ($\Omega_0 = 0.3$, $\Omega_{0\Lambda} = 0$) are generally more concentrated than halos in ΛCDM ($\Omega_0 = 0.3$, $\Omega_{0\Lambda} = 0.7$) or SCDM ($\Omega_0 = 1$, $\Omega_{0\Lambda} = 0$) models, because they form earlier and the mean cosmic density is higher when they collapse. On the other hand, halos formed in a low-density ΛCDM model are less concentrated than those formed in the SCDM model: even if they have an higher collapse redshift, the mean cosmic density is lower when they form.

Several different aspects of lensing by halos with NFW or generalized NFW profiles can be found in Bartelmann Bartelmann (1996), Wright & Brainerd Wright & Brainerd (2000), Li & Ostriker Li & Ostriker (2002), Wyithe, Turner & Spergel Wyithe et al. (2001), Perrotta et al. Perrotta et al. (2002), Meneghetti et al. Meneghetti et al. (2002), Bartelmann et al. Bartelmann et al. (2002a,b). If we take $\xi_0 = r_s$, the density profile (3.65) implies the surface mass density

$$\Sigma(x) = \frac{2\rho_s r_s}{x^2 - 1} f(x) \; , \tag{3.68}$$

with

$$f(x) = \begin{cases} 1 - \frac{2}{\sqrt{x^2-1}} \arctan\sqrt{\frac{x-1}{x+1}} & (x > 1) \\ 1 - \frac{2}{\sqrt{1-x^2}} \operatorname{arctanh}\sqrt{\frac{1-x}{1+x}} & (x < 1) \\ 0 & (x = 1) \end{cases} \; . \tag{3.69}$$

The lensing potential is given by

$$\Psi(x) = 4\kappa_s g(x) \; , \tag{3.70}$$

where

$$g(x) = \frac{1}{2}\ln^2\frac{x}{2} + \begin{cases} 2\arctan^2\sqrt{\frac{x-1}{x+1}} & (x > 1) \\ -2\operatorname{arctanh}^2\sqrt{\frac{1-x}{1+x}} & (x < 1) \\ 0 & (x = 1) \end{cases} \; , \tag{3.71}$$

and $\kappa_s \equiv \rho_s r_s \Sigma_{\mathrm{cr}}^{-1}$. This implies the deflection angle

$$\alpha(x) = \frac{4\kappa_s}{x} h(x) \; , \tag{3.72}$$

with

$$h(x) = \ln\frac{x}{2} + \begin{cases} \frac{2}{\sqrt{x^2-1}} \arctan\sqrt{\frac{x-1}{x+1}} & (x > 1) \\ \frac{2}{\sqrt{1-x^2}} \operatorname{arctanh}\sqrt{\frac{1-x}{1+x}} & (x < 1) \\ 1 & (x = 1) \end{cases} \; . \tag{3.73}$$

It is an important feature of the NFW lensing potential [Eq. (3.70)] that its radial profile is considerably less curved near the center than the SIS profile [Eq. (3.45)]. Since the local imaging properties are determined by the curvature of Ψ, this immediately implies substantial changes to the lensing properties [see Fig. (3.5)].

The convergence can be written as

$$\kappa(x) = \frac{\Sigma(\xi_0 x)}{\Sigma_{cr}} = 2\kappa_s \frac{f(x)}{x^2 - 1} \; , \tag{3.74}$$

from which we obtain the dimensionless mass,

$$m(x) = 2\int_0^x \kappa(x')x'dx' = 4k_s h(x) \; . \tag{3.75}$$

The lens equation for this kind of lens model can be solved by using numerical methods. At fixed halo mass, the critical curves of an NFW lens are closer to its center than for SIS lens because of its flatter density profile. There, the potential is less curved, thus the image magnification is larger and decreases more slowly away from the critical curves. Therefore NFW lenses are less efficient in image splitting than SIS lenses, but comparably efficient in image magnification.
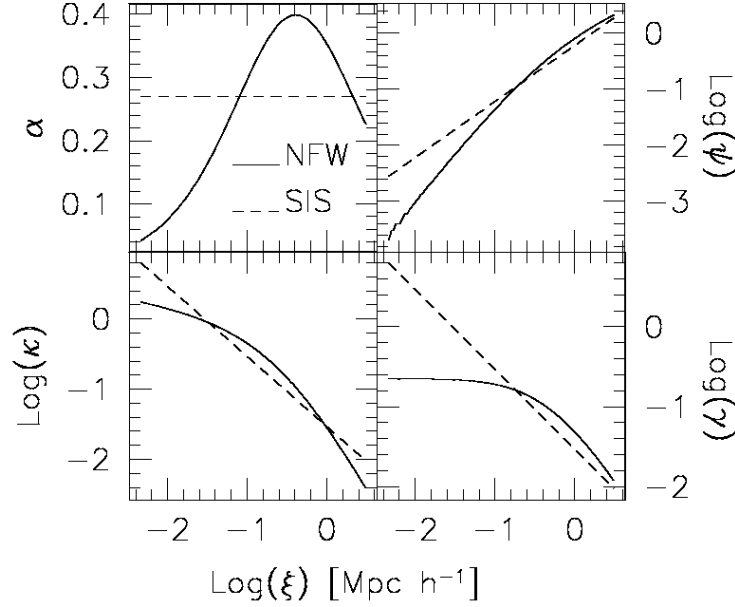
Figure 3.5: Some properties of NFW and SIS lenses as functions of the distance from the lens center. Top left panel: reduced deflection angle; top right panel: lensing potential; bottom left panel: convergence; bottom right panel: shear.

3.3 Towards more realistic lenses

3.3.1 External perturbations

It is often necessary to embed a lens into an external shear field which is created by matter in the neighbourhood. We want to represent this shear by a potential Ψ_γ, which must satisfy the following conditions:

$$
\begin{aligned}
\gamma_1 &= \frac{1}{2}(\Psi_{11} - \Psi_{22}) = \text{const.} \\
\gamma_2 &= \Psi_{12} = \text{const.} \\
\kappa &= \frac{1}{2}(\Psi_{11} + \Psi_{22}) = \text{const.} .
\end{aligned}
\tag{3.76}
$$

If $\Psi_{11} \pm \Psi_{22}$ are required to be constant, Ψ_{11} and Ψ_{22} must separately be constants, thus

$$
\Psi_\gamma = C x_1^2 + C' x_2^2 + D x_1 x_2 + E .
\tag{3.77}
$$

This requires

$$
\begin{aligned}
\frac{1}{2}(\Psi_{11} - \Psi_{22}) &= C - C' = \gamma_1 \\
\Psi_{12} &= D = \gamma_2 \\
\frac{1}{2}(\Psi_{11} + \Psi_{22}) &= C + C' = \kappa
\end{aligned}
$$

(3.78)

Imposing $\kappa = 0$, we obtain

$$
C = -C' \quad \Rightarrow \quad C = \frac{\gamma_1}{2} \ .
$$

(3.79)

Therefore,

$$
\Psi_\gamma = \frac{\gamma_1}{2}(x_1^2 - x_2^2) + \gamma_2 x_1 x_2
$$

(3.80)

Likewise, if we want to place our lens on a sheet of constant surface-mass density, the shear of that sheet must be zero (because no direction can be prefered), and from Eq. 3.78 we find

$$
\Psi_\kappa = \frac{\kappa}{2}(x_1^2 + x_2^2) \ .
$$

(3.81)

Irrelevant constants have been suppressed above.

We can now embed e.g. a softened isothermal sphere into a constant shear field,

$$
\Psi = \sqrt{x^2 + x_c^2} + \frac{\gamma_1}{2}(x_1^2 - x_2^2) + \gamma_2 x_1 x_2
$$

(3.82)

yielding the deflection angle

$$
\begin{aligned}
\vec{\nabla}\Psi &= \frac{\vec{x}}{\sqrt{x^2 + x_c^2}} + \begin{pmatrix} \gamma_1 x_1 + \gamma_2 x_2 \\ -\gamma_1 x_2 + \gamma_2 x_1 \end{pmatrix} \\
&= \frac{\vec{x}}{\sqrt{x^2 + x_c^2}} + \begin{pmatrix} \gamma_1 & \gamma_2 \\ \gamma_2 & -\gamma_1 \end{pmatrix} \vec{x}
\end{aligned}
$$

(3.83)

and the convergence remains unchanged by construction.

The deflection angle of a sheet of constant surface-mass density is

$$
\vec{\alpha} = \vec{\nabla}\Psi_\kappa = \kappa\vec{x} \ .
$$

(3.84)

Thus, the lens equation reads, in this case,

$$
\vec{y} = \vec{x} - \vec{\alpha} = \vec{x}(1 - \kappa) \ .
$$

(3.85)

If $\kappa = 1$, $y = 0$ for all images, i.e. this sheet focuses all light rays exactly on the origin. This gravitational lens thus has a well-defined focal point.

Remark:
When combining the potentials of the lens and of external perturbers the same scale ξ_0 must be chosen if using adimensional coordinates.
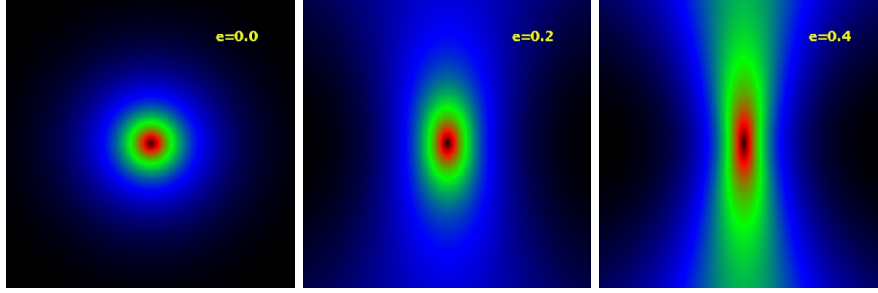
Figure 3.6: Deflection angle map for an axially symmetric (left panel) and elliptically distorted NFW lens model, for ellipticity 0.2 (central panel) and 0.4 (right panel). The lens mass and redshift are $10^{15} M_\odot h^{-1}$ and 0.3 respectively. The source redshift is 1. The side length of each panel is $\sim 6'$.

3.3.2 Elliptical lenses

A circularly symmetric lens model is too much idealized to describe the properties of real lenses, like galaxies or galaxy clusters. Slighltly less unrealistic models are obtained by adding two more parameters: the ellipticity and the position angle describing the orientation of the lens.

The construction of lens models with elliptical or pseudo-elliptical isodensity contours is generally quite complicated Kassiola et al. (1992); Kormann et al. (1994); Golse & Kneib (2002). One can start from the projected surface-mass density of an axially symmetric model

$$\Sigma(x) = f(x) \tag{3.86}$$

and can obtain its elliptical generalization by substituting

$$x \rightarrow X = \sqrt{\frac{x_1^2}{(1-e)} + x_2^2(1-e)} \,, \tag{3.87}$$

where $e = 1 - b/a$ is the ellipticity and a and b are the major and minor axis of the ellipse. This ensures that the mass inside circles of fixed radius remains constant as the ellipticity changes. The resulting model will have elliptical iso-density contours whose major axis will be oriented along the x_2-direction. The model can then arbitrarily rotated by the desired position angle, θ.

The complication in this approach comes from the fact that obtaining the potential corresponding to these kinds of density distributions can become extremely complicated, even for quite simple lens models. It is simpler and often sufficient to model a lens by means of an elliptical effective lensing potential.

For any axially symmetric lensing potential in the form

$$\Psi(x) = g(x) \tag{3.88}$$

the same substitution given in Eq. 3.87 can be carried out.

The Cartesian components of the deflection angle are then

$$
\begin{aligned}
\alpha_1 &= \frac{\partial \Psi}{\partial x_1} = \frac{x_1}{(1-e)X}\tilde{\alpha}(X) \,, \\
\alpha_2 &= \frac{\partial \Psi}{\partial x_2} = \frac{x_2(1-e)}{X}\tilde{\alpha}(X) \,,
\end{aligned}
\tag{3.89}
$$
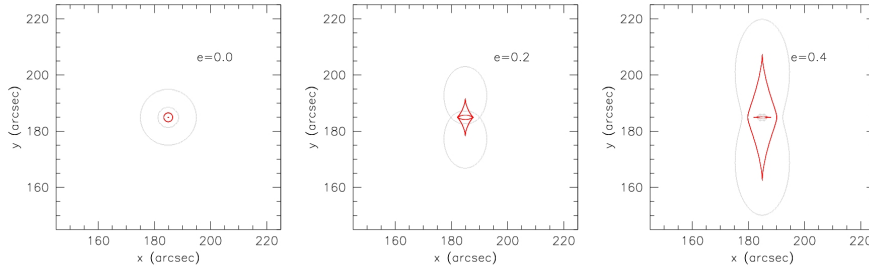
Figure 3.7: Critical lines (black lines) and caustics (red lines) for the same lens models as in Fig. (3.6).

where $\tilde{\alpha}(X)$ is the unperturbed (i.e. axially-symmetric) deflection angle at the distance X from the lens center.

Using these formulae, deflection-angle fields for different values of the ellipticity e are readily computed. Some examples for deflection-angle maps are displayed in Fig. (3.6), where ellipticity is included in the lensing potential of the sphere with the NFW density profile. Starting from an elliptical lensing potential is computationally much more tractable, but has the disadvantage that the deflection angle field and the mass distribution corresponding to the elliptical potential can become dumbbell-shaped even for moderate ellipticities. This is unwanted for galaxy lenses but admissible for galaxy clusters, because they are less relaxed and exhibit substructure.

Increasing the ellipticity of the lensing potential strengthens the shear field of the lens, and consequently the caustics and the critical lines expand and change. Examples for the change of the caustics and of the critical lines with ellipticity e for a pseudo-elliptical NFW halo are shown in Fig. (3.7), which refers to a lens with mass $M = 10^{15}\,h^{-1}\,M_\odot$ at redshift $z = 0.3$, and the underlying cosmology is the ΛCDM model. As discussed above, the radial and tangential caustics are a circle and a point, respectively, for the axially symmetric models. Increasing e, the caustics stretch, develop cusps, and enclose an increasing area. The critical lines, which are originally circles on the lens plane, are stretched as well and assume the dumbbell shape which characterizes the surface density distribution of the lens.

In the case of non-axially symmetric lenses, a wide variety of image configurations can be produced. Some examples are shown in Fig. (3.8). Compared to the axially-symmetric case, when the source is enclosed within two caustics, it has five images. One appears at the lens center, and the four others form a cross-shaped pattern. When the source is moved outward, two of the four outer images move along the tangential critical line towards each other, merge, and disappear when the source cross the tangential caustic. Three images remain until the source crosses the radial caustic, when two more images approach each other perpendicular to the radial critical line, merge and disappear. After that, only one weakly distorted image remains.
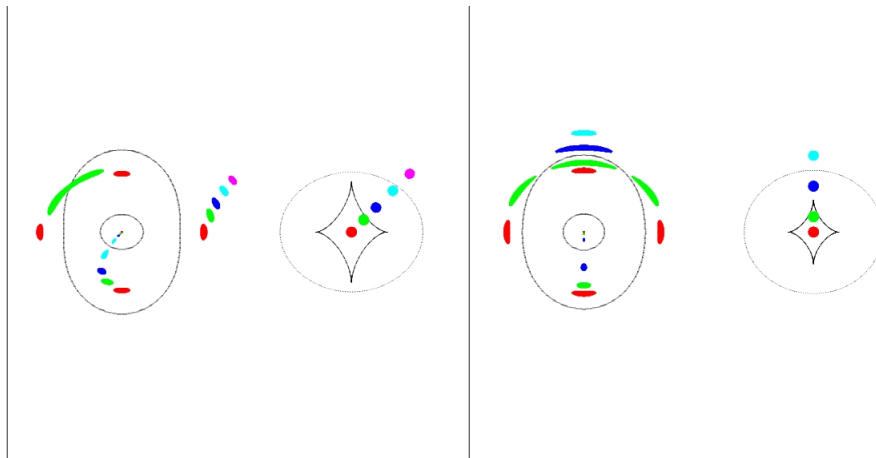
Figure 3.8: Compact source moving away from the center of an elliptical lens. Left panel: source crossing a fold caustic; right panel: source crossing a cusp caustic. Within each panel the digram on the right shows the caustics and the source positions and the left diagram shows the critical lines and the corresponding image positions (Figure from Narayan & Bartelmann, 1995).

4 Microlensing

We derived in Chapter 3 the formalism to describe lensing by point masses. Such simple model of lens is useful to describe a class of lensing phenomena which are called *microlensing events*. These are produced by lenses whose sizes are small compared to the scale of the lensing system. In other words, to classify a lensing event as microlensing, we need sufficiently small masses and sufficiently distant lenses and sources. Such lenses can be for example planets, stars or any compact object floating in the halo or in the bulge of our or of other galaxies. Typically, a mass which gives raise to microlensing events is in the range $10^{-6} \leq M/M_\odot \leq 10^6$. The corresponding Einstein radii are smaller than a milli-arcsecond.

In this chapter we will briefly review some important results in microlensing studies. For a more detailed discussion, we recommend the paper by Joachim Wambsganss (astro-ph/0604278).

4.1 Lensing of single stars by single stars

We consider here the simplest case of microlensing: lensing by single foreground stars on single background stars in the Milky Way or in the Local Group. In this regime, lens and source distances are of the order kpc. The curvature of the space time is negligible so that in most cases we can assume that $D_S = D_L + D_{LS}$.

Moreover, we can generally safely adopt the approximation of point lens and point source. This is justified in most of the cases of interest:

(1) the mass distribution of a star can be assumed to be spherically symmetric. This implies that the projected mass distribution is axisymmetric, independent of the direction. The mean free path of photons is small in all but the extreme outer layers of stellar atmospheres, Therefore the star is not transparent. If it has a radius $R_\star$, all the light approaching the lens with an impact parameter $b \leq R_\star$ will be absorbed. On the other hand, all rays having $b > R_\star$ will pass by the lens and will be deflected by

$$\hat{\alpha} = \frac{4GM}{c^2 b} \ , \tag{4.1}$$

where M is the total mass of the star. The point mass approximation then holds as long as we consider impact parameters larger than the star radius;

(2) the characteristic scale, which characterizes the lens is the Einstein radius, θ_E. This scale defines the typical separation between multiple images, $\Delta\theta \sim 2\theta_E$. Then, the source can be well approximated by a point if its angular size is smaller than θ_E. Stellar sources subtend considerably smaller angles than the Einstein
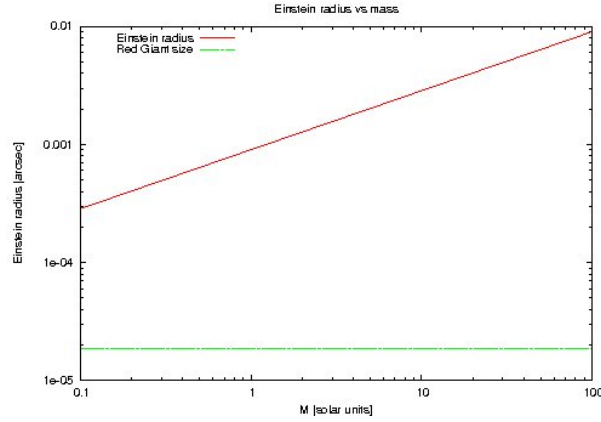
Figure 4.1: Einstein radius vs mass of the lens (red line), assuming that the lens and the source are at $\sim 5\text{kpc}$ and $\sim 10\text{kpc}$, respectively. The horizontal green line shows the angular size of a red giant star at the distance of the source.

radii in most of the microlensing systems. Fig. 4.1 compares the Einstein radius of lenses with different masses (red line) with the typical angular size of a red giant star (green line), assuming that the star acting as source is at the border of our galaxy ($\sim 10\text{kpc}$) and the lens at half way to the source ($\sim 5\text{kpc}$). Clearly, the approximation holds even for source stars of the largest angular sizes.

Given the smallness of the Einstein radius, a microlensing event cannot be detected via observation of multiple images of the background source. However, the Earth and the stars in our galaxy participate to the motion of the galaxy around its center. Potential lenses in the galaxy then move relative to potential sources in the halo or in some external galaxies. The relative velocities are such that the time scale of the relative change of lens and sources is of the order of weeks or shorter.

Since the magnification given by Eq. 3.17 is function of the source position, the relative motion of the source with respect to the lens introduces a variability in the light curve of source:

$$L[y(t)] = \mu[y(t)]\hat{L} \;, \tag{4.2}$$

where $\hat{L}$ is the source intrinsic luminosity. The characteristic time scale of the change of L is given by the time needed to the source to cross the lens Einstein ring,

$$t_E = \frac{D_L \theta_E}{v_\perp} \;. \tag{4.3}$$

In the last equation, $v_\perp$ is the component of the velocity of the source relative to the lens which is perpendicular to the observer's line of sight (transverse velocity).

Assuming that for the duration of the lensing event the motion of the source is rectilinear, the trajectory of the source can be represented by

$$y(t) = \sqrt{y_0^2 + \left(\frac{t - t_0}{t_E}\right)^2} \;, \tag{4.4}$$

where y_0 is the minimal distance between the lens and t_0 is the time of closest approach, $y(t_0) = y_0$. Combining Eq. 3.17 with Eq. 4.4, we derive different light curves of the source for different impact parameters y_0, as shown in Fig. 4.2.
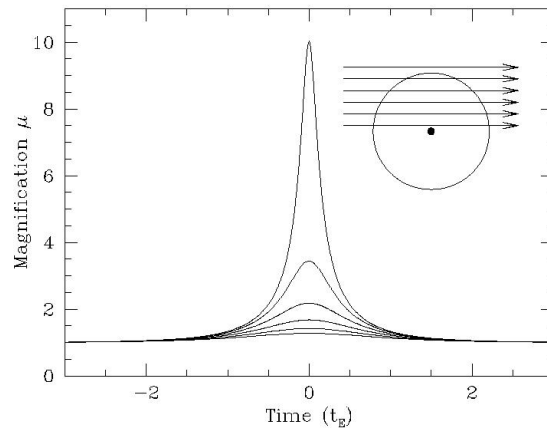
Figure 4.2: Magnification of a point source lensed by a point lens for different impact parameters y_0. Figure taken from Wambsganss (2006).

Such light curves are described by four parameters: the unlensed luminosity (flux), $\hat{L}$, the time of closest approach, t_0, the distance of closest approach, y_0, and the Einstein crossing time t_E. Of these, $\hat{L}$ can be measured when the source is at large angular distances from the lens; t_0 can be taken as the time when the light curve reaches its maximum; y_0 can be measured if the lens position is known, which happens very rarely. In any case, y_0 only depends on the random placement of lens and source on the sky. Only t_E contains physical informations about the lensing system, because it depends on the lens mass M, on the distances between observer, lens and source and on the transverse velocity $v_\perp$. Assuming that the distance between observer and source can be determined in some way, we remain with three physical parameters which are embedded into t_E in a degenerate combination. The microlensing event itself gives us very little possibility to measure or estimate the lens mass M, the lens distance D_L or the transverse velocity $v_\perp$ independently.

Example: degeneracy between mass M and distance D_L

As an example, consider a Galactic microlensing system in which the source is known to lie in the Galactic Bulge at 8kpc and the Einstein time t_E has been precisely determined to be 40 days. Assuming that the lens is within the galaxy, the transverse velocity is likely to be $0 < v_\perp < 600$km s^{-1}, with values nearer to the middle of the range statistically favored. The figure on the side illustrates the resulting degeneracy in the mass and distance of the lens. The distribution of the lens masses ranges from those of massive brown dwarfs ($\lesssim 0.1 M_\odot$) to that of a heavy stellar black hole ($\sim 10^2 M_\odot$). From Wambsganss (2006)
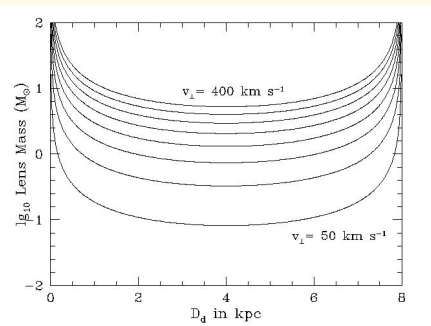
Note also that, even if the source light typically dominates the lens light dramatically, and the so called *blending* effect is generally negligible, in those cases when this does not happen, the light curve depends on one additional parameter: the lens luminosity

L_L. This makes more problematic the determination of t_E.

4.2 Searching for dark matter with microlensing

4.2.1 General concepts

Based on an idea proposed by Paczynski (1986), several groups have tried to use microlensing to measure the density and the total mass of a population of objects, in particular the so called *Massive Astrophysical Compact Halo Objects* (MACHOs), one of the possible candidates for the dark matter in the galaxy.

The idea is the following. Imagine that we are looking, through a distribution of microlenses in our galaxy, at some more distant sources, for example in the Magellanic Clouds. The microlenses would produce time-variable magnification of the background stars. The more abundant and massive the microlenses are, the more frequent and longer the microlensing events would be.

Let the solid angle of the observation be $\delta\Omega$, and the microlens density as a function of distance be $n(D_L)$. Then, the optical depth is

$$\tau = \frac{1}{\delta\Omega} \int dV n(D_L)\pi\theta_E^2 \ , \tag{4.5}$$

where $\pi\theta_E^2$ is the cross section of the microlensing event. Since the volume element is $\delta V = \delta\Omega D_L^2 dD_L$, we obtain

$$\begin{aligned}\tau &= \frac{1}{\delta\Omega} \int_0^{D_S} \delta\Omega D_L^2 dD_L n(D_L)\pi \frac{4GM}{c^2}\frac{D_{LS}}{D_L D_S} \\ &= \frac{4\pi G}{c^2} \int_0^{D_S} dD_L \frac{D_{LS}D_L}{D_S}\rho(D_L) \ , \end{aligned} \tag{4.6}$$

where $\rho = Mn$ is the mass density of lenses (assumed to have all the same mass). Assume further that the space-time is flat, so that $D_L + D_{LS} = D_S$, and introduce $x = D_L/D_S$. Then,

$$\tau = \frac{4\pi G}{c^2}D_S^2 \int_0^1 x(1-x)\rho(D_S x)dx \ . \tag{4.7}$$

If $\rho \approx$ const along the line of sight to the sources

$$\tau \approx \frac{2\pi}{3}\frac{G\rho}{c^2}D_S^2 \ . \tag{4.8}$$

For a galaxy whose stars rotate with velocity v,

$$v^2 \approx \frac{GM_g}{r} \Rightarrow M_g = \frac{rv^2}{G} \ , \tag{4.9}$$

the density is

$$\rho \approx \frac{3M_g}{4\pi r^3} \approx \frac{3}{4\pi G}\left(\frac{v}{r}\right)^2 \ , \tag{4.10}$$

and the optical depth is

$$\tau \approx \frac{1}{2}\left(\frac{v}{c}\right)^2 \ . \tag{4.11}$$

Thus, the optical depth for a galaxy like the Milky way is of the order of 10^{-6}, if all of its matter is composed of microlenses and the sources are at the boundaries of the galaxy ($D_S \sim r$). This means that roughly one out of a million stars in the nearby galaxies will be lensed, i.e. magnified by at least $\mu \sim 1.34$.

Therefore, if one measures the optical depth for microlensing by counting the number of microlensing events in a particular direction, he can characterize the whole population of microlenses. The possibility of detecting such events depends on their duration (the Einstein crossing time). This is determined by the transverse velocity $v_\perp$ and by the lens mass. For microlenses in the halo of the galaxy ($D_L \sim 10$kpc) with tangential velocity $v_\perp \sim 200$km s^{-1}, it is

$$t_E \approx 6 \times 10^6 \text{ s } \left(\frac{M}{M_\odot} \right)^{0.5} \approx 0.2 \text{ yr} \left(\frac{M}{M_\odot} \right)^{0.5} \tag{4.12}$$

In reality, since the lenses have velocity vectors with different orientations and intensities, there will be a distribution of event durations characterized by a tail of long events, caused by those lenses whose velocity is mainly radial. At the same time, also the lens masses and distances are within a range of values, which also contributes to broaden the distribution of the durations of the microlensing events.

If all events have the same time scale, then the number of events N expected in the monitoring time Δt would be given by

$$N = \frac{2}{\pi} n \tau \frac{\Delta t}{t_E} , \tag{4.13}$$

(Paczynski, 1996), where n is the total number of sources monitored.

4.2.2 Observational results in searches for dark matter

Among the many candidates, it has been proposed that the dark matter could be in the form of compact objects distributed in the halo of the galaxy. If the mass of such objects is in the range $10^{-6} \lesssim M/M_\odot \lesssim 10^6$, they would originate detectable microlensing signal, because they would occasionally pass close to the line-of-sight to a background star in the Large or in the Small Magellanic Clouds.

Many groups have tried to detect such lensing signal. This was not an easy task because it requires to monitor a huge number of stars with a good time resolution, waiting for fluctuations of their luminosity. In the last fifteen years however, such campaigns became possible. First, technological improvements in construction of astronomical detectors allowed to build up wide field CCD cameras, so that large spots in the sky could be observed simultaneously. Second, software for automatic data reduction was developed and computer speed increased allowing to process huge amounts of data in few time. Third, dedicated telescopes became available to the scientific community for large monitoring campaigns.

A huge number of stars have then been monitored in the direction of the LMC/SMC. The principal results found by the several groups active in this field can be summarized as follows:

- the MACHO team (USA/Australia) analyzed data taken from 11.9 million stars in the direction of the LMC over 5.7 years. They found 13-17 microlensing events, while between 2 and 4 were expected from known stellar populations in the Milky Way and in the LMC. The microlensing optical depth deduced from lensing events lasting between 2 and 400 days is (Alcock et al., 2000)

$$\tau_{\text{LMC(MACHO)}} = 1.2^{+0.4}_{-0.3} \times 10^{-7} . \tag{4.14}$$
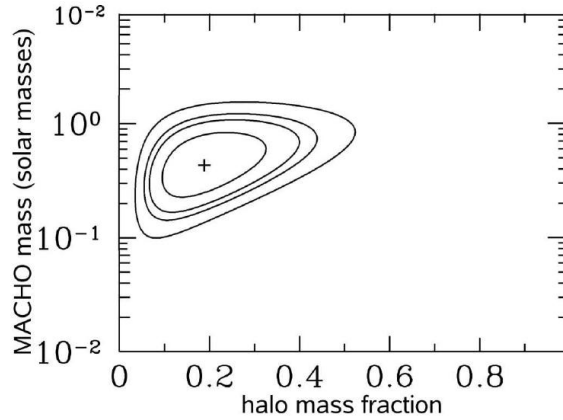
Figure 4.3: Example of likelihood contours obtained from the MACHO experiment for one specific model for the Milky Way halo. The abscissa is the fraction of the halo mass contained in MACHOs, the ordinate is the MACHO mass. The contours shown are the 60%, 90%, 95% and 99% confidence levels. From Bartelmann (2005).

This implies that between 8% and 50% of the Milky Way's halo can be composed of MACHOs (at 95% confidence), whose most likely mass ranges between $0.15M_\odot$ and $0.9M_\odot$. The likelihood contours obtained from the MACHO experiment for one specific model of the Milky Way are shown in Fig. 4.3;

- the EROS project (France) found results consistent with those of the MACHO collaboration. Based on their observations of the LMC and SMC, MACHOs cannot dominate the Galactic halo if their masses are $\lesssim 1M_\odot$. They find that the halo mass fraction in MACHOs is $< 20\%$ for MACHO masses between $10^{-7}M_\odot$ and $0.1M_\odot$ (at 95% confidence). The upper limit to the optical depth from the data towards the SMC is (Afonso et al., 2003)

$$\tau_{\mathrm{SMC(EROS)}} \leq 10^{-7} \; . \tag{4.15}$$

Preliminary analysis of the full 6.7 year EROS data set on the LMC indicate an optical depth (Wambsganss, 2006)

$$\tau_{\mathrm{LMC(EROS)}} \approx 10^{-7} \; . \tag{4.16}$$

Thus, although MACHOs have been detected between us and the Magellanic Clouds, they are insufficient for explaining all of the Milky Way's dark mass. These MACHO's can in principle be anywhere between the source stars and the observer, i.e. in the dark halos of the Milky Way or of the Magellanic Clouds. It is unlikely that all of the LMC lensing events are due to self-lensing by stars. The important results of the microlensing experiments is that the Galaxy and the LMC must be embedded into extended dark matter halos, only a fraction of which is composed of compact objects of stellar and sub-stellar mass.

Microlensing monitoring programs are now targeting the Andromeda galaxy M31. M31 is roughly 15 times as distant as the LMC/SMC and the individual stars cannot be resolved anymore. This means that we can only measure the flux of many stars within any pixel of the CCD camera. Since the source is so much extended, the magnification effect during a microlensing event is diluted. Only high magnification events will result detectable.

However, using the "pixel lensing" approach
towards M31 has also several important ad-
vanges. First, the high inclination of the
disc of M31 would result in an asymmetry
in the observed rate of microlensing events,
if the disc is surrounded by a halo filled with
MACHOs. The idea is illustrated in the fig-
ure on the right (taken from Kerins et al.
(2001)): the optical depth is expected to be
lower towards the "near" disk and higher to-
wards the "far" disk. Neither variable stars
or self-lensing events in the disc of M31
would exhibit such asymmetry.
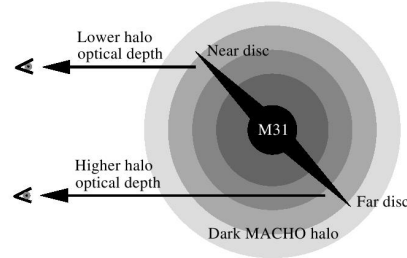
Second, being far away from M31 has the advantage that the we can accurately measure
the rotation curve and the surface brightness profile of the galaxy and derive a more
reliable model than we can do from inside the Milky Way. Third, since M31 is a
large and massive galaxy, it contains a huge number of potential sources and we can
choose several line of sight through its halo, allowing to map the spatial distribution
of MACHOs. Fourth, due to the large distance of M31, microlensing events due to
the Milky Way halo objects are statistically distinguishable from those produced by
M31-halo objects.

A few teams are actually looking for microlensing events towards M31. Interestingly,
the POINT-AGAPE collaboration (UK/France) is finding a large microlensing signal
compared to that measured by the EROS team towards the Magellanic Clouds (Paulin-
Henriksson, private communication).

4.3 Binary lenses

We consider now a lens consisting of two point-mass components. Let assume that
these have masses M_a and M_b, respectively. Due to the linear dependence of the
deflection angle on the mass, the total deflection angle of a ray crossing the lens plane
at $\vec{\xi}$ is in this case

$$\hat{\vec{\alpha}}(\vec{\xi}) = \frac{4G}{c^2} \left[\frac{M_a}{|\vec{\xi} - \vec{\xi}_a|^2}(\vec{\xi} - \vec{\xi}_a) + \frac{M_b}{|\vec{\xi} - \vec{\xi}_b|^2}(\vec{\xi} - \vec{\xi}_b) \right] \ . \tag{4.17}$$

The presence of the second lens component breaks the axial symmetry of the system.
The resulting lensing effect is much different from the case of a single lens.

First of all, the lens becomes astigmatic. This results into a completely different mag-
nification pattern on the source plane and in the appearance of extended caustics. As
seen in the previous chapters, caustics are lines which separate regions with different
image multiplicities. When the source crosses a caustic during its motion relative to the
lens, new images are created or destroyed. As in the case of a single point mass, the
image separations are too small to allow to see them, but the light curves are generally
much more complicated and exhibit multiple peaks, asymmetries, etc.

Due to the presence of the second lens component, there are three new parameters
which characterize the light curves. These are

(1) the mass ratio, $q = M_a/M_b$;

(2) the separation between the two components, d, which is commonly expressed in
units of the Einstein radius for a point-mass lens of mass equal to the total mass
of the system, $M = M_a + M_b$;
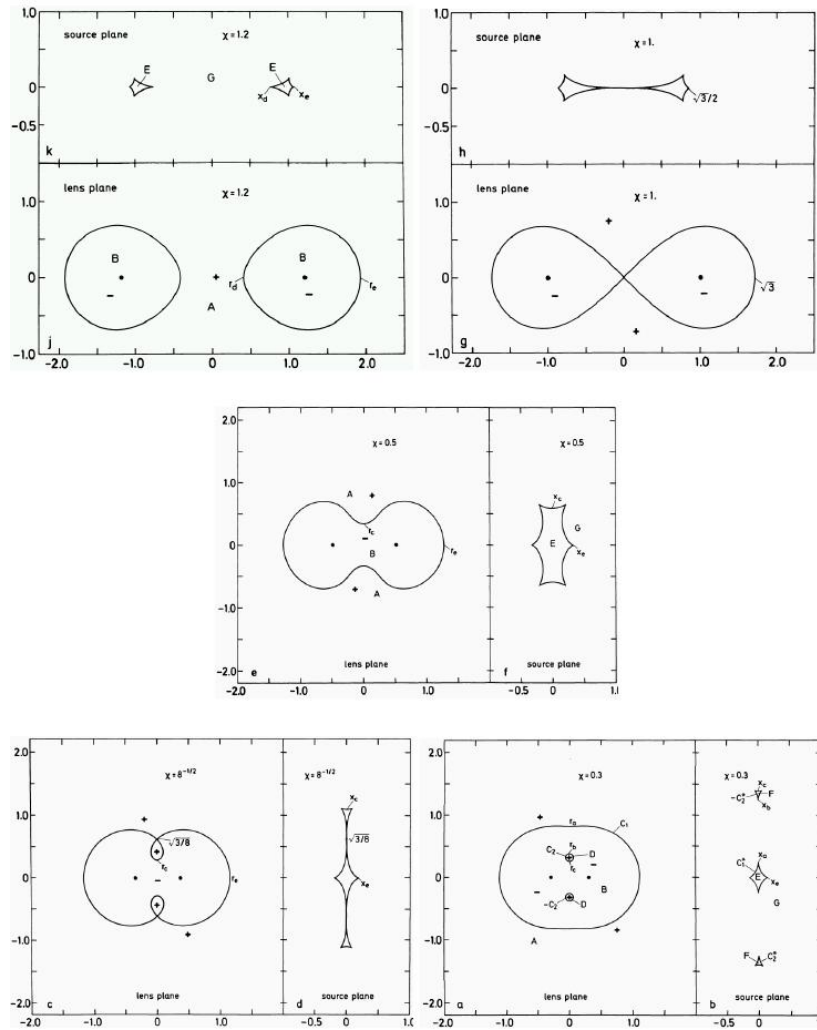
Figure 4.4: Critical lines and caustics for a binary lens system consisting of two equal point masses with decreasing separation. From Schneider & Weiss (1986).

(3) the angle ϕ between the source trajectory and the line connecting the two lenses.

Thanks to the large number of parameters involved, the analytical derivation of the critical lines and caustics of binary lens systems is very complicated. Qualitatively, we can find three regimes, which are illustrated in Fig. 4.4 for two lenses with the same mass ($q = 1$):

(1) when the two lenses are widely separated $d > 1$, they act like single lenses which slightly feel the perturbation of the companion. The point caustic becomes an asymmetric asterisk with four cusps. The corresponding critical line becomes an oval (top left panel, $d = 1.2$);

(2) once the separation of the two lenses approaches $d = 1$, the critical lines and the corresponding caustics merge together. They first touch in one point (top right panel, $d = 1$), then, for further decreasing separations, there is one single critical line and one single caustic, which is characterized by six cusps (middle
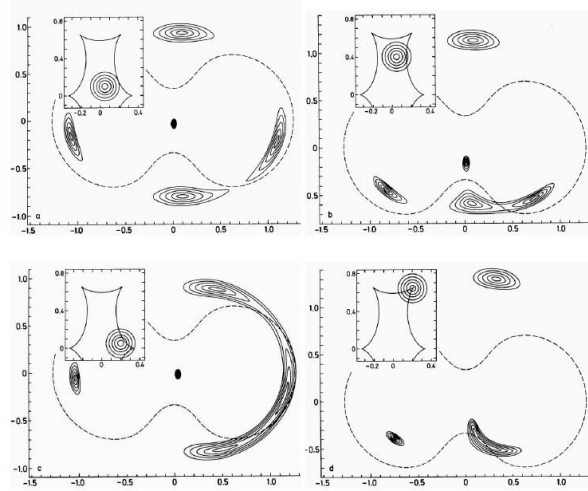
Figure 4.5: Image configurations for an extended source lensed by a binary lens with $q = 1$ and $d = 0.5$. The insets show the position of the source relative to the caustics. From Schneider & Weiss (1986).
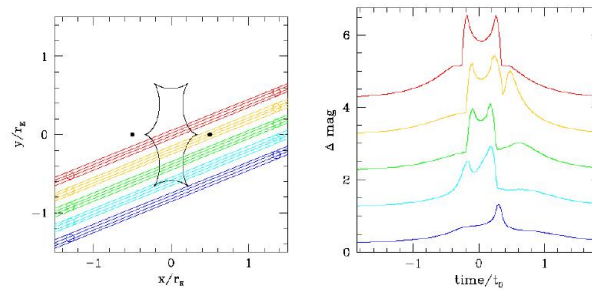
Figure 4.6: The left panel shown some possible trajectories of an extended source (circles) relative to the caustics of a binary lens. In the right panel, the corresponding lightcurves are displayed. From Wambsganss (2006).

    panel, $d = 0.5$);

(3) when the separation reaches $d = 8^{-0.5} \approx 0.35355$ (bottom left panel), two regions inside the critical line detach and the caustic breaks down into three parts. These are a central diamond-shaped and two triangular-shaped caustics. By reducing further the separation between the two components, the two triangular caustics move away from the central one, which also shrink (bottom right panel, $d = 0.3$.

The signs $+$ and $-$ in Fig. 4.4 indicate the parity of the images forming on the lens plane. Several examples of image configurations for different positions of an extended source with respect to the caustics of a binary lens with $q = 1$ and $d = 0.5$ are shown in Fig.4.5. If the source is inside the caustic, it produces five images: three are inside the critical line and two are outside it. When the source crosses the caustic, two or three images merge together and disappear. During the transition the images assume the usual arc-like shape. Their size increases and therefore they are highly magnified.

Microlensing lightcurves originated by binary lenses reflect the complexity of the caustic structures. For example, in the left panel of Fig. 4.6 we consider several parallel tra-
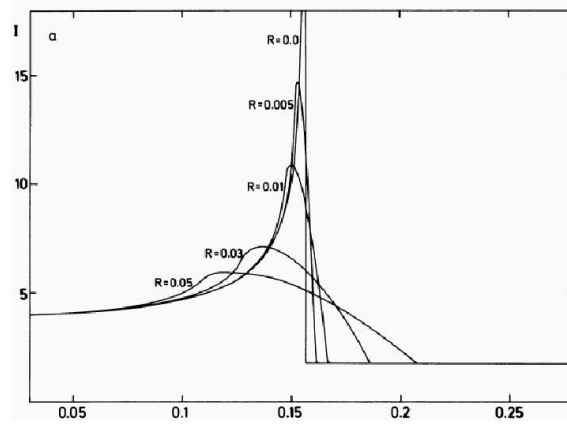
Figure 4.7: Variations of the lightcurves during a fold caustic crossing due to different source sizes. From Schneider & Weiss (1986).

jectories of an extended source relative to the caustic of a binary lens, and in the right panel we show the resulting lightcurves. A peak appears when the source crosses or passes very close to the caustic. The number of the peaks and their height can differ substantially. The peaks themselves can be more or less sharp. This depends on the size of the source: small sources produce sharper peaks when they cross a caustic, larger sources produce smoother lightcurves (Schneider & Weiss, 1986). Some examples are shown in Fig.4.7, where the crossing of a source with varying radius along the fold of a caustic is simulated. The source radius is expressed in units of the Einstein radius.

Based on the fact that more than 50% of all stars are in binary systems, Mao & Paczynski (1991) predicted that a large number of microlensing events is originated by binary lenses. Not all of them can be identified through the shape of the lightcurves because of the large range of separations between the lens components. For very close pairs of stars and for wide systems, these binaries act as single or two single lenses, respectively. For this reason, only 10% of the microlensing lightcurves should show signatures of binarity in the lens.

Example: OGLE-7

OGLE-7 is the first microlensing event whose lightcurve revealed the presence of a binary lens. It was discovered in 1993 by the OGLE team, a collaboration between Poland and USA, who was monitoring the LMC and the SMC in search of microlensing events.

The source star had a constant flux during the monitoring in 1992, then brightened up by more than two magnitudes during 1993, showing two sharp peaks separated by ~ 60 days. Udalski et al. (1994) found a binary lens solution for describing such lightcurve. The lens have $q = 1.02$ and the projected separation between the two components is $1.14\theta_E$. The star has a trajectory with impact parameter $b = 0.05\theta_E$ and inclination angle $\phi = 48.3$ degrees with respect to the axis passing through the two lens components. The Einstein crossing time is $t_E = 80$ days, the baseline magnitude is $I_0 = 18.1$, and the fraction of "blended" light is $f = 56\%$.

The "blending" is due to the presence of an additional source along the line of sight. This can be the lens itself or another star in the foreground or in the background. Witt & Mao (1995) found that the minimum total magnification for a source inside the caustic is three. If this is not the case, it can be caused by "blending" or by a third component in the lens ("triple lens"). For OGLE-7 the magnification in between the caustic crossing was 2.2 and 2.4 in the R and I bands respectively.

The observed lightcurve and the best fit lens model are shown in the figure above (taken from Udalski et al. (1994)).
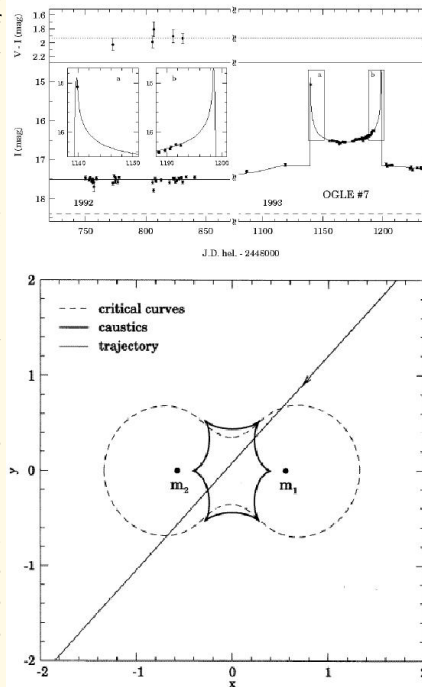
4.4 Microlensing surveys in search of extrasolar planets

4.4.1 General concepts

A particular type of binary lenses is that consisting of a star and of a planet orbiting around it. In this case, the lens is characterized by a mass ratio $q = M_{\mathrm{p}}/M_\star \ll 1$, where M_{p} and $M_\star$ are the mass of the planet and of the star, respectively. Thus, the light curve of a microlensing event produced by such lens systems consists of a single-lens light curve, where the planet just add a brief perturbation. The detections of such "anomalies" in the light-curves measured in microlensing event is one of the methods proposed to reveal the presence of planets around stars. This method is sensitive to masses as low as the mass of the Earth, and, as we will see, is giving the first interesting results.

In the figure on the right, we show the geometry of a microlensing event involving a star and a planet. The optical axis is chosen such to pass through the observer and the star. The large dots indicate the lens and the source stars, the small filled dot represents the planet. Its projected position on the lens plane, whose distance from the lens star defines the parameter d, is given by the small empty circle. (The figure is taken from Rattenbury (2006))
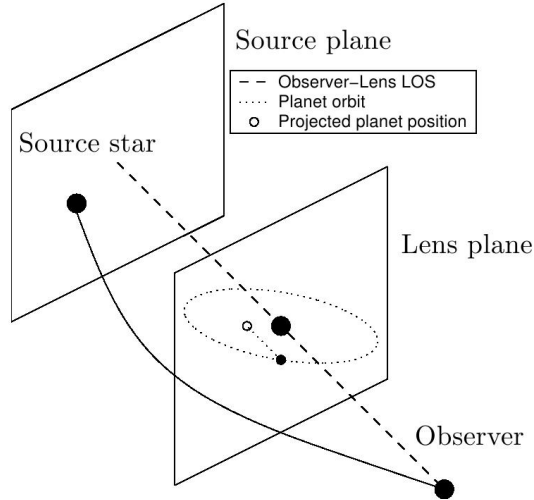
The natural unit of length is the Einstein radius, θ_E. Being $q \ll 1$, this is determined essentially by the mass of the star,

$$
\begin{aligned}
\theta_E(M_{\mathrm{p}} + M_\star) &\approx \theta_E(M_\star) \\
&= \left(\frac{4GM_\star}{c^2} \frac{D_{\mathsf{L}} D_{\mathsf{LS}}}{D_{\mathsf{S}}} \right)^{1/2} \\
&= 4.42\,\mathrm{AU} \left(\frac{M_\star}{0.3 M_\odot} \right)^{1/2} \left(\frac{D_{\mathsf{S}}}{8\mathrm{kpc}} \right)^{1/2} [x(1-x)]^{1/2}\,, \quad (4.18)
\end{aligned}
$$

where $x = D_{\mathsf{L}}/D_{\mathsf{S}}$ and $D_{\mathsf{LS}} \approx D_{\mathsf{S}} - D_{\mathsf{L}}$.

A planetary microlensing event falls into one of two broadly defined groups, based on when and how the planet perturbation is produced. Typically, in these binary lenses, the mass ratios and the distances between the components are such that both the planet and the star develop separated and extended caustics. There is always a small central caustic located near the lens-observer line of sight. This originates from the degenerate point-like caustic of the star, slightly perturbed by the presence of the planet. One or two planetary caustics are also present. Their size, position and orientation depends on the planet-star mass ratio and projected orbit radius. The planet alone should also develop a point caustic, but the strong perturbation given by the star transform such a point into a much more extended caustic. This is shown in Fig. 4.10. In the upper panel the caustics of a star-planet lens are recognizable along the axis $y = 0$. A zoom over them, displayed in the two bottom panels, show their shape in detail.
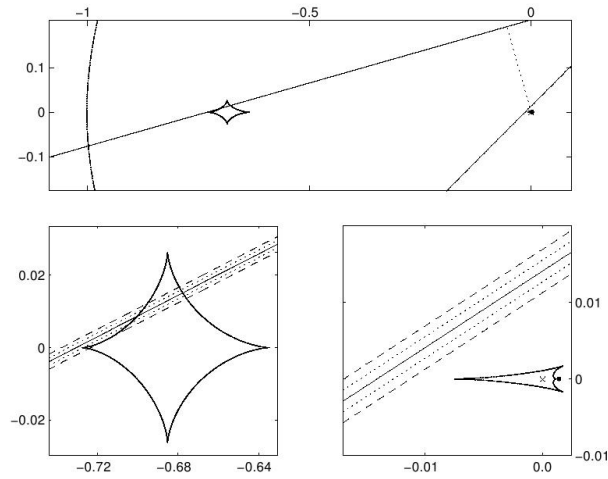
Figure 4.8: Comparison between detecting planets through caustic crossing events and high magnification events. Both axes are in units of θ_E. Top: Critical and caustic curves for a planetary lens system with $q = 10^{-3}$ and $d = 1.4$. Two source star tracks are shown, one corresponding to a low amplification planetary caustic crossing event, with $y_{\min} = 0.2$ and inclination angle $106°$; the other corresponding to a high amplification event, passing close to the small central caustic ($y_{\min} = 0.01$) with an inclination angle of $135°$. Bottom: Zoom over the regions surrounding the planetary (left) and central (right) caustics. The dashed and dotted lines refer to source radii $r_\star = 2 \times 10^{-3}\theta_E$ and $r_\star = 10^{-3}\theta_E$, respectively. From Rattenbury (2006).

If a source star moves relative to the lens and passes across a planetary caustic line, we have a first type of planetary microlensing event, namely a "caustic-crossing" event. Such case corresponds to the solid track connecting the bottom left to upper right corners of the upper panel in Fig. 4.10. The same source track is displayed in the bottom-left panel. In this example, two values of star radius are used, $r_\star = 2 \times 10^{-3}\theta_E$ (dashed lines) and $r_\star = 1 \times 10^{-3}\theta_E$ (dotted lines). The corresponding light curve is shown in the upper panel of Fig. **??**. It is characterized by three peaks super-imposed to the single-mass light curve which should be originated by the star alone (dashed line). The first peak corresponds to the passage of the star close to the left cusp of the planetary caustic. The other two occur at the caustic crossings. The thick and the thin lines refer to the larger and to the smaller source radii, respectively.

The second class of planetary microlensing events involves the source star passing close to the central caustic. Approaching the cusp of two caustic lines also produces a perturbation in the source magnification, which can be used to infer the presence of the planet. Such case is illustrated again in Fig. 4.10. The source track is now given by the line approaching the central caustic at $\sim (0,0)$ from the bottom left. In this case the source is strongly amplified by the star lens, and the perturbation produced by the planet appears as a secondary bump in the light curve (see the bottom panel of Fig. **??**).

Extra-solar planets have been detected in both types of microlensing events.

4.4.2 Observing strategy

As previously seen in this chapter, the probability that a microlensing event takes place is very small (10^{-6}). Then, once such events have been detected, one needs to monitor
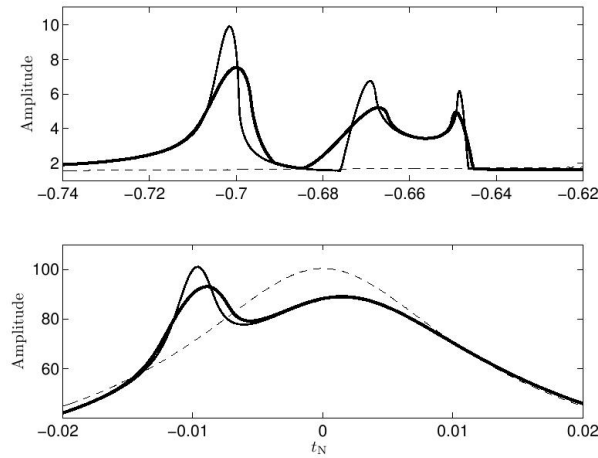
Figure 4.9: Light curves of the microlensing events described in Fig 4.10. The source amplification is shown as a function of the normalised time $t_N = (t_{JD} - t_0)/t_E$, where t_0 and t_E are the time of closest approach of the source to the star and the time required for crossing the Einstein ring, respectively. Top: planetary caustic crossing event. Bottom: high-amplification event. The thin and thick lines refer to the smallest and the largest source radii, respectively. The dashed line shows the light curve in absence of the planet. From Rattenbury (2006).

accurately the light curve for obtaining information about the lens system. The search for extra-solar planet is related to that for dark matter concentrations. As said, some groups make routine observations towards the Galactic bulge and the Magellanic Clouds. Those which are currently active are the OGLE and the MOA (New Zealand/Japan) collaborations. OGLE uses a 1.3m telescope located at La Silla (Chile). MOA works with a 1.8 telescope at Mount John, New Zealand. They analyze images at real-time and whenever they find light curves which show clear deviations from a single lens light profile they alert the scientific community.

Then, there are several other groups which perform follow-up observations of such microlensing events. These are PLANET (international collaboration), μFUN (US/SA/Israel/Korea) and RoboNET (US/UK/Australia) who use telescopes longitudinally spaced around the world to measure in detail the light curves.

So far four planets have been detected through microlensing (OGLE-2003-BLG-235/MOA-2003-BLG-53, OGLE-2005-BLG-071, OGLE-2005-BLG-390, OGLE-2006-BLG-169). One more detection is likely to be a planet (MACHO-98-BLG-35). A Table summarizing the details of such detections, taken from Rattenbury (2006) is shown below. For the confirmed detections, the planetary masses are in the range between $5.5^{+5.5}_{-2.7}\,M_\oplus$ (OGLE-2005-BLG-390) and $0.5 - 4M_J$ (OGLE-2005-BLG-071, preliminary result). MACHO-98-BLG-35 is probably a very light planet ($M_p \sim 0.4 - 1.5\,M_\oplus$).

Table 2.   Planetary microlensing event parameters

Event	A_{max}	t_E (d)	Source Star Sp[b]	ρ	Lens Star[a] Sp[b]	M_1 ($M_\odot$)	D_1 (kpc)	Planet q ($\times 10^{-3}$)	d (R_E)
O235/M53	7.5	61.5	G	0.00096	M2-M7	$0.36^{+0.03}_{-0.28}$	$5.2^{+0.2}_{-2.9}$	$3.9^{+1.1}_{-0.7}$	1.120(7)
O71[c]	42	70.9	?	?	?	$0.08 - 0.5$	$1.5 - 5$	7.1(3)	1.294(2)
O390	2.8	11.03	G4[d]	0.026	M	$0.22^{+0.21}_{-0.11}$	$6.6^{+1.0}_{-1.0}$	0.076(7)	1.610(8)
O169	$\simeq 800$	44	?	$\simeq 0.0005$	M	$0.49^{+0.23}_{-0.29}$	$2.7^{+1.6}_{-1.3}$	$0.08^{+0.02}_{-0.03}$	1.00(2)
98-35	96	27.7	?	0.002^e	?	0.3^e	6.0^e	$0.013^{+0.002}_{-0.009}$	1.225^f

[a]Quoted confidence limits are 90% for events OGLE-2003-BLG-235/MOA-2003-BLG-53 and OGLE-2005-BLG-169, and 68% for event OGLE-2005-BLG-390. [b]Luminosity class V unless specified otherwise. [c]Preliminary analysis. [d]Luminosity class III. [e]Assumed value. [f]Degenerate solution at $1/d = 0.81$ R_E.

Example: OGLE-2003-BLG/MOA-2003-BLG-53

This event was identified by the OGLE col-
laboration on June 22, 2003. It was inde-
pendently identified by the MOA collabora-
tion on July 21, 2003. The planetary signal
was discovered later (Bond et al., 2004).
The light curve in the I band is shown on
the right: it shows evidence of a plane-
tary caustic crossing feature, correspond-
ing to a crossing time of ~ 7 days. The
data (1092 data points from MOA and 183
from OGLE) were fit with different classes
of models.
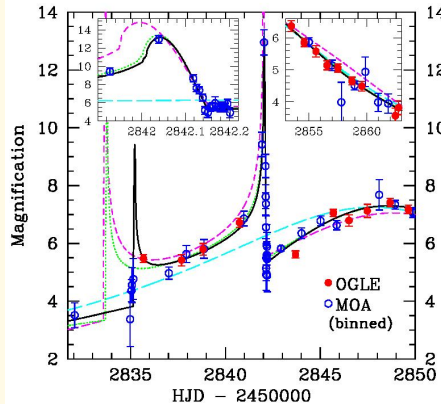
The fitting parameters were $y_{\min}$, t_E, t_0, q, d, ϕ and the source size in units of the
Einstein radius. The best fit model corresponds to the light curve given by the solid
black line. This model has an extreme mass ratio of $q = 0.0039$, which is a strong
indication that the secondary lens component is a planet. Other "non planetary"
models with $q > 0.03$ are strongly disfavored (see the magenta dashed line in the
Figure), because they would require larger magnification inside the caustic curve than
is observed. Moreover they would deviate more from the single lens light curve before
and after the caustic crossing (as shown by the two insets). A single lens model is
obviously ruled out as well (blue long-dashed line).

Some degeneracy between the system parameters exists which can be broken using
some external constraints. The only parameter which is directly measurable is the
Einstein crossing time t_E, which constraints the lens mass, distance and transverse
velocity with respect to the line of sight to the source. The color and baseline mag-
nitude of the source star suggested that this was a G-type bulge star near the Main
Sequence turn-off. Using color-color relation and empirical relations between $V - K$
and surface brightness, the source angular radius was determined. Modeling the light
curve gives instead the source radius in units of the Einstein radius. Combining the
two determinations, the Einstein radius was found to be $\theta_E = 520 \pm 80$ μas. Using
Eq. 4.18, the mass of the lens star was found to be

$$\frac{M_\star}{M_\odot} = 0.123 \left(\frac{\theta_E}{\text{mas}}\right)^2 \frac{D_S}{\text{kpc}} \frac{x}{1-x} \ . \tag{4.19}$$

The mass-luminosity relations for main-sequence stars allows to define an upper limit
to the lens distance star, which is determined to be $D_L < 5.4$ kpc. Thus, if it is
a main sequence star, the lens must be in the Galactic disk. Using Galactic disk
models, a maximum likelihood analysis based on the measurements of θ_E and t_E
gives $D_L = 5.2^{+0.2}_{-2.9}$ kpc, from which it was inferred that the lens star is an M2-M7
dwarf star of mass $0.36^{+0.03}_{-0.28}\,M_\odot$. The best fitting $q = 0.0039$ and $d = 1.12$ therefore
suggest that the planetary companion has mass $M_p = 1.5^{+0.1}_{-1.2}M_J$ and orbits at a
distance of $3.0^{+0.1}_{-1.7}$ A.U. from the lens star.

4.4.3 Discussion

Other methods have been employed to search for extrasolar planets. Briefly, the most
used can be summarized as follows:

- **astrometry:** it consists of searching for the influences of planets on the proper
  motions of the stars around which they orbit. A number of candidates have been
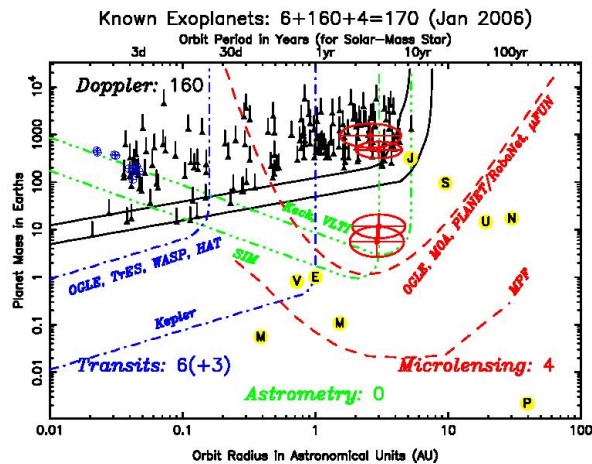
Figure 4.10: Distribution of known exo-planets in the plane orbit radius/planet mass. From Rattenbury (2006).

found using this method but none of them are confirmed. The main reason of such uncertainty is that the changes in proper motion are so small that they can be hardly measured with the instruments available today;

- **Doppler effect:** high precision spectroscopy allows to evidence the presence of a planet around a star through the Doppler effect. Both the star and the planet orbit around the center of mass of the system. The component of this motion along the line of sight is revealed by changes in the radial velocity of the star which can be deduced from the displacement in the star's spectral lines due to the Doppler effect. This method was very successful and allowed to detect ~ 160 extra-solar planets. However, its works for relatively close stars and it finds planets with small orbital radii. Moreover, it cannot be used to detect planets whose orbital plane is almost perpendicular to the line of sight;

- **transit:** this method detects a planet's shadow when it transits in front of its host star. This "transit method" works only for the small percentage of planets whose orbits happen to be perfectly aligned from astronomers' vantage point, but can be used on very distant stars. It has led to the discovery of a few planets with high mass;

- **pulsar timing:** the presence of a planet around a pulsar is found by observing anomalies in the regularity of pulses from the pulsar itself. Even if it has allowed the discovery of a few planets, in particular that orbiting around the binary system PSR B1620-26, the main limitation of the method is that it can be applied to a specific class of lenses only.

In Fig. **??** the distribution of all the known extra-solar planets in the planet mass/orbit radius plane is shown. Systems discovered via Doppler effect are indicated by the black triangles. They are concentrated in the upper-left corner of the diagram, reflecting the fact that this method is most efficient in detecting massive planets orbiting at small distance from their star. The theoretical detection limits of this method are shown by the solid black lines (sensitivities of 3 m/s and 1 m/s, respectively). Transit detections are given by the blue-circled plus. This method is also efficient at detecting massive, close planets. The theoretical detection limits are shown by the dashed dotted lines for ground based and space observations (as expected for the Kepler Space Observatory,

scheduled for launch in 2008). Astrometry still have to provide detections. The region of the diagram where instruments like Keck and VLTI could be able to find planets is that enclosed by the upper green dot-dashed line. NASA is building a space interferometer called SIM PlanetQuest, which will measure the proper motion of stars with an accuracy of one millionth of an arcsecond. The detection limits of this instrument are give by the bottom green dot-dashed curve. Finally, the red ellipses show the microlensing detections. The upper red dashed lines represent the detection limits reached by the ongoing microlensing collaborations. The Microlensing Planet Finder, a proposed space telescope dedicated to microlensing observations will dramatically increase the detectability of low-mass, large orbital radius planets. The yellow dots indicate the solar planets.

Clearly, microlensing is the most successful method for detecting low-mass planets. As mentioned before, planets of a few Earth masses have already been found and, with the next generation of experiments, objects of sub-earth mass will become detectable.

4.5 Microlensing of QSOs

In the next Chapter we will discuss in more detail the lensing effects of galaxies on background QSOs. In general, if the QSO happens to be within the galaxy caustics, it is strongly lensed and has multiple images (see also the discussion about axially symmetric and elliptical lenses in Chapter 3). The galaxy is made of stars, star clusters and possibly other compact objects, whose Einstein radii are of the order of

$$\theta_E \approx 10^{-6}\sqrt{\frac{M}{M_\odot}}\mathrm{arcsec} \qquad (4.20)$$

for "typical" lens and source redshifts of $z_\mathsf{L} \sim 0.5$ and $z_\mathsf{S} \sim 2$. The QSO continuum emitting regions have sizes comparable or smaller than the Einstein radii of stellar mass objects. Thus, such microlenses in the halo of the lensing galaxy can perturb the multiple images of distant QSOs. Since the galactic halo participate to the motion of the galaxy, the microlenses move relative to the background QSO. Thus their effect remain imprinted in the luminosity curve of the source. In particular, there will be luminosity fluctuations on a time scale of the order of

$$t_{cross} = \frac{R_{source}}{v_\perp} \approx 4R_{15}v_{600}^{-1}\mathrm{months} \ , \qquad (4.21)$$

which corresponds to the the time required for a source of radius R_{source} and transverse velocity $v_\perp$ to cross its own diameter. In the previous equation, the size of the QSO and its relative velocity have been parameterized in units of 10^{15} cm and 600 km/s respectively.

In microlensing of multiple QSOs, the convergence is of order unity. This means that a any given time a whole ensemble of microlenses is affecting the QSO. The phenomenon is illustrated in Fig.4.11. The ensemble of point lenses creates a complicated magnification pattern on the source plane (left panel). High magnification regions are brighter and correspond to a network of caustics. Three different tracks are given by the dashed lines, along which a background QSO moves. The corresponding light curves are shown in the right panel for small (solid lines) and large (dashed lines) sources. If the size of the QSO is small compared to the intra-caustic spacing, each individual caustic crossing is resolved. Otherwise, the light curves appear smooth. The shape of the light curve is also determined by the brightness profile of the source. The steeper it is, the sharper are the fluctuations.
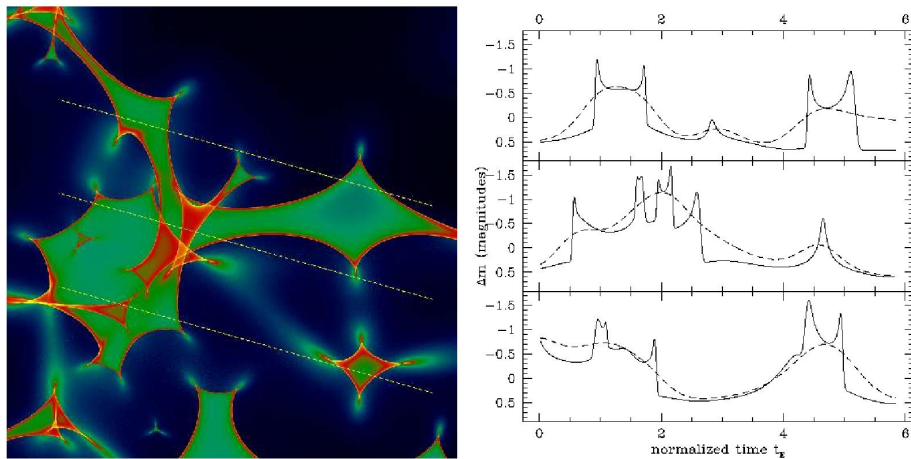
Figure 4.11: Left: microlensing magnification pattern produced by stars in a lensing galaxy. The dashed lines indicate three tracks along which a background QSO moves. Right: light curves corresponding to the tracks shown in the left panel. Solid and dashed lines refer to small and large sources, respectively. This first is a source with a gaussian luminosity profile with width of about 3% of the Einstein radius. The second is larger than the first by a factor of 10. Figures from Wambsganss (2006).

Thus, several important informations about the lens and the source can be derived by analyzing the light curves of multiply imaged QSOs:

- the existence and effects of compact objects between the observer and the source;

- the size of QSOs;

- the two-dimensional brightness profile of QSOs;

- the mass (and the mass distribution) of lensing objects

Example: QSO 2237+0305

QSOs are intrinsically variable sources. Therefore, it is usually very difficult to understand if the eventual fluctuations in their light curves are due to microlensing. However, if multiple images of a QSO exist, then this becomes possible. Indeed, the intrinsic variability of the source should show up in all the light curves (with some time delay). Conversely, those fluctuations which are not present in all the light curves are due to microlensing events.
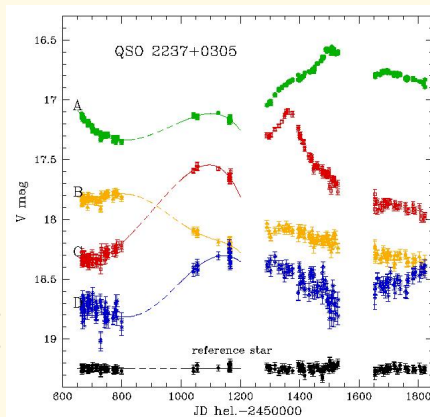
Irwin et al. (1989) found evidence for cosmological microlensing in one of the light curves of the quadruply imaged QSO Q2237+0305. Such object has been accuretely observed by the OGLE group (Woźniak et al., 2000a,b) who showed that all four components show variations corresponding to Δm between ~ 0.4 and ~ 1.3.

Comparison of the lightcurves with simulations show that the continuum emitting region of the QSO is relatively small, of order 10^{14} cm (see e.g Wambsganss, 1990).

Example: QSO Q0957+561

By measuring the microlensing effects, the population of microlenses can be constrained. A decade ago, it was popular the idea that dark matter halos could be made of black holes in the mass range of about $10^6 M_\odot$. If such a population of black holes exist, it would produce clear lensing signatures observable in the high resolution images of radio jets observed with VLBI. This was shown by Wambsganss & Paczynski (1992), who found that the microlenses would produce features like kinks, holes, additional milli-images in the images of the two jets of Q0957+561. Based on these results, Garrett et al. (1994) ruled out that the halo of the lensing galaxy in this double QSO consist of such objects.
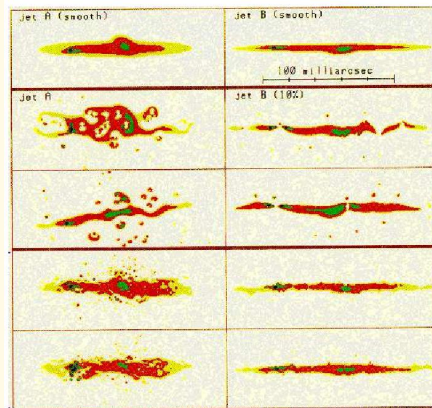
5 Lensing by galaxies and galaxy clusters

This Chapter gives an overview on the lensing phenomena produced by extended lenses like galaxies and galaxy clusters in the universe.

The lensing events produced by such lenses fall into two broad classes. If the observer, the lens and the source happen to be well aligned along the line of sight, i.e. if the observer is looking at far sources which are projected on the sky at small angular distances from the centre of the lens, and if the combination of convergence and shear in the inner regions of the lens is appropriate, *strong lensing* events may be observed. Depending on the characterisics of the lens and of the sources, such events may consist of

- multiple images of background sources. For example, massive galaxies can split one bright QSO into several images. The displacement of such images is determined by the mass distribution of the lenses. The spectra of all these images conserve all the features contained in the spectrum of the corresponding source. Therefore, multiple images can be identified thanks to spectral analysis;

- highly distorted images. If the source is extended, the differential deflection of the light creates distortions in the images. As discussed earlier, such distortions can be in the radial or in the tangential direction. The first is particularly large around the tangential critical curves, the second close to the radial critical curves. Typical and spectacular examples of distorted images are the gravitational arcs which are observed in the core of many massive galaxy clusters;

Conversely, if the angular separation between source and lens is large, lensing shows up in the *weak* regime. Such effect is detectable only by averaging on an ensamble of extended sources (galaxies), which happen to lay behind the lens. The shape of the images of these sources may be only weakly affected by lensing. The small distortions are difficult to measure. It is impossible to do so on the images of single galaxies because the deformation is indistiguishable from the intrinsic shape of the sources. Since the distortion is coherent across a region on the sky surrounding the lens, it can be detected only averaging over several sources in a given aperture.

Both the weak and the strong lensing regimes will be discussed in the following sections.

5.1 Strong lensing

5.1.1 General considerations

Strong lensing occurs in the central regions of galaxies and galaxy clusters when the lens is "critical". This happens when it develop extended critical lines. As seen in Chapter

2, these form where the conditions

$$
\begin{aligned}
\lambda_t &= 1 - \kappa - \gamma = 0 \\
\lambda_r &= 1 - \kappa + \gamma = 0 \ .
\end{aligned}
$$

(5.1)

(5.2)

The first equation defines the *tangential* critical line, the second the *radial* critical line. It is obvious that extended systems are much more complex lenses than point masses. Their strong lensing properties are determined by a much larger number of parameters than those which play a role in microlensing.

In particular

- galaxies and clusters are made of dark matter and baryons (stars, gas). These components may have different spatial ditributions;

- we may think of extended lenses as composed of a **main clump of matter** and many **substructures** orbiting around it. One can imagine a galaxy or a galaxy cluster as the superposition of several surface density modes corresponding to different spatial scales. Following this idea, we can write the surface density as a multipole expansion:

$$
\kappa(\vec{x}) = \kappa_0(x) + \sum_{m=1}^{\infty} \kappa_m(x) \exp(im\phi) \ ;
$$

(5.3)

- in this expansion the term κ_0 is the monopole and it describes the axially symmetric part of the lens; the term with $m = 1$ is the dipole; the term with $m = 2$ is the quadrupole, which gives the degree of **ellipticity** of the iso-density contours. If a "power spectrum" is calculated with the coefficients κ_m, these result to be the most important terms;

- the **density profile** $\kappa(x)$ $[\rho(r)]$ is a fundamental property of the lens. In Chapter 2, the differences between the lensing properties of the NFW and SIS profiles were highlightened: different profiles produce remarkably different lensing features, for example different multiplicities of the images, different strengths of the shear field and of the magnification pattern on the source and on the lens planes;

- depending on the shape of its density profile, a lens can be more or lens sensitive to **external perturbations**. For example, an external shear $\vec{\gamma}_e$, which corresponds to a lensing potential

$$
\Psi_\gamma(\vec{x}) = \frac{\gamma_e}{2}(x_1^2 - x_2^2) \ ,
$$

(5.4)

perturbs much more easily an NFW than a Singular-Isothermal sphere. The reason is that the SIS density profile is significantly steeper than the NFW in the central part. The situation is illustrated in Fig. 5.1. In the left panels, the critical lines and caustics of two axially symmetric lenses with the same mass $(M = 10^{14} \, M_\odot)$ are shown. The lens and the source redshifts are assumed to be 0.3 and 1.0, respectively. An external shear, whose amplitude is $\gamma_e = 0.1$, is applied to both the lenses. The corresponding critical lines and caustics are shown in the two right panels. Clearly, the deformation of the critical lines (and caustics) is more significant for the NFW than for the SIS profile;

- the **impact of the substructures**, described by the higher order multipoles in Eq. 5.3, is therefore much larger in halos whose density profiles are shallower. The same two lenses which were earlier embedded into an external shear are now
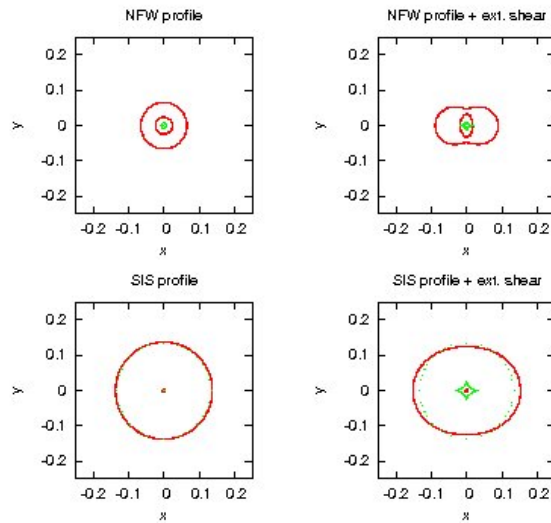
Figure 5.1: The figure illustrate how the shape of the critical lines (red) and of the caustics (green) change when the lens is embedded into an external shear. The upper and the bottom panels refer to an NFW and to a SIS lens model, respectively.
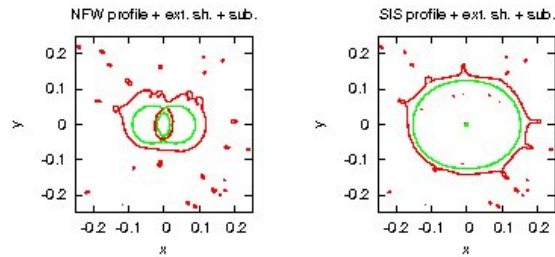
Figure 5.2: Different sensitivity to substructures of lenses with NFW (left) and SIS (right) density profiles. The red curves show the critical lines after populating the halo of the lens with 30 subhalos with masses $10^{10} < M/M_\odot < 10^{11}$. The green curves show the corresponding critical lines in absence of the subhalos.

shown in Fig. 5.2 after having been populated with 30 axially symmetric subhalos. Each subhalo has mass between 10^{10} and $10^{11} \, M_\odot$ and has been modelled as a SIS. One could think that they represent galaxies in the halo of a galaxy cluster. The same subhalos have been used to populate both the lenses. Two important features can be noticed. First, for both the NFW and SIS profiles, the critical lines of the main clump are expanded. The relative expansion of the critical line of the NFW lens is significantly larger than that of the SIS. Substructures typically enhance the strong lensing hability of the lens, because they provide additional convergence and shear. Second, the critical lines around the individual subhalos have different sizes, depending on density profile of the halos within which they are embedded. In other words: substructures are much stronger lenses when the structure they belong to has a shallow density profile;
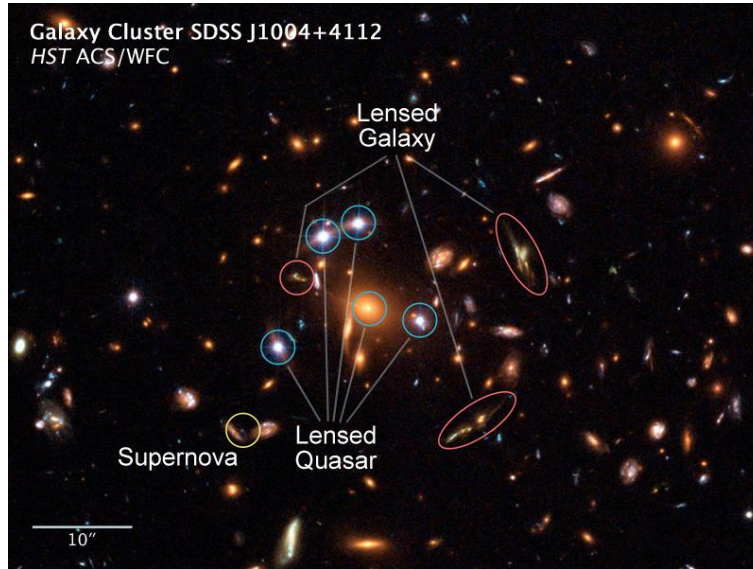
Figure 5.3: The galaxy cluster SDSS J1004+4112 has 5 images of a QSO close to its centre. A the same time, several other background galaxies are strongly lensed by this cluster.

5.1.2 Observables

What can we learn from images like that in Fig. 5.3? In fact, we can extract a huge amount of informations from this kind of observations. Indeed, lensing is a unique tool for tracing the total mass distribution of the lens and at the same time it magnifies distant sources, allowing to see objects which otherwise would be very faint. Finally, since lensing is a geometrical effect, for lensing systems at cosmological distances some important information about the geometry of the universe can be derived.

It is then crucial to use in the proper way the observational constraints given a lens system.

Galaxies and galaxy clusters can strongly lens point or extended sources. The angular separation between multiple images if of the order of the Einstein ring,

$$
\begin{aligned}
\theta_E &= 0.9'' \left(\frac{M}{10^{11} M_\odot} \right)^{1/2} \left(\frac{D}{\text{Gpc}} \right)^{1/2} \\
&= 1.5' \left(\frac{M}{10^{15} M_\odot} \right)^{1/2} \left(\frac{D}{\text{Gpc}} \right)^{1/2},
\end{aligned}
\tag{5.5}
$$

which means that the multiple images can be well resolved.

Among the things that can be measured for a lens are

(1) the relative positions of the components (lens and images; astrometric constraints);

(2) the relative fluxes of the images;

(3) the time delays between the images;

(4) several properties of the lens (dynamical properties, light distribution in different bands, etc.);

(5) the microlensing of the images.

The astrometric constraints are the most important. We can usually measure the relative positions of the lensed components very accurately (5 mas or better). Substructures and other perturbers set a lower limit of order 1-5 mas with which it is safe to impose astrometric constraints. A given lens-source model provides a configuration of the images which can be compared with the observations. If the images are extended, additional constraints derive from the fact that we can measure the relative transformation between one image and the other.

Flux ratios are relatively easy to measure, but not very useful because of the systematic uncertainties (see later in the text). As we will see, flux ratios are predictable. However, if taken at a sigle epoch they are affected by time variablity in the source (which appears with some time delay in the different images), microlensing (in galaxies) or lensing by subhalos and substructures (in galaxies and clusters), absorption by ISM (galaxies) and IGM (clusters). In fact, most applications of flux ratios have focused on probing these perturbers rather than on studying the mass distribution of the lenses.

Measurements of time delays are possible mainly for sources which are lensed by galaxies. Indeed, the angular separations between multiple images in galaxy clusters are typically too large and the time delays too long (except for close pairs of multiple images, like in SDSS J1004+4112, see astro-ph/0607513). For example, from Eqs. 2.64 and 3.48, the time delay between the two images produced by a SIS is

$$\Delta t_{SIS} = \frac{1}{2} \frac{D_{\mathsf{L}} D_{\mathsf{S}}}{c D_{\mathsf{LS}}} (1 + z_{\mathsf{L}})(\theta_A^2 - \theta_B^2) \; . \tag{5.6}$$

Such delay amounts to some months in the case of galaxies ($\theta_E \sim 1''$) and to some decades in the case of galaxy clusters. To date, time delays have primarily been used to estimate the Hubble constant rather than the surface density, but if we assume to know H_0 or consider only time delays ratios, then time delays can be used to constrain the mass distribution.

Any independent measurement of the mass of a component will also help to constrain the structure of the lens. For galaxies, this primarily means making stellar dynamical measurements of the lens galaxy and comparing the dynamical mass estimates to those from the lens geometry. For clusters, the dynamics of cluster galaxies, the X-ray emission from the hot intra-cluster gas, or weak lensing (see later) can be used to estimate the cluster mass. Unfortunately, these independent mass estimates are frequently in disagreement with those derived from strong lensing.

Using microlensing variability to constrain the mass distribution around where images appear is actually more theory than practice due to the lack of microlensing light curves for almost all lenses.

5.1.3 Mass modelling

One of the most important applications of strong lensing is that of using the observables listed above to constrain the mass distribution of the lens in its inner region.

The mass modelization of the lens is never an easy task. In particular, the modeler has to deal with huge degeneracies in the parameter space which make several models able to fit the observed data.

There exist two different approaches to this problem. The first consists in using parametric fitting models to recover the mass distribution of the lens. The monopole term is modelled using some analytic profile like those discussed in Chapter 3 (SIS, NFW, SIE, etc.). The quadrupole is added by introducing ellipticity into the model. Higher order terms in the multipole expansion of the surface density are generated by adding

additional mass components to the lens. The effect of the enviroment is mimicked by adding external shear. Each of the ingredients which are used to construct the model is described by some parameters. The list **p** of all these parameters defines the lens model.

Suppose we use only the astrometric constraints. The lens equation supplies the source position for each combination of the model parameters:

$$\vec{\beta}_i = \vec{\theta}_i - \vec{\alpha}(\vec{\theta}_i, \mathbf{p}) \tag{5.7}$$

It is easy to project the images onto the source plane and then minimize the difference between the projected source positions. This can be done with a χ^2 fit statistic of the form

$$\chi^2_{src} = \sum_i \left(\frac{\vec{\beta} - \vec{\beta}_i}{\sigma_i} \right)^2 . \tag{5.8}$$

The position of the source $\vec{\beta}$ is unknown, therefore it is a model parameter. By minimizing the χ^2, we look for the minimal scatter between the source points leading to the observed images.

The advantage of using χ^2_{src} is that mapping the observed positions of the images on the source plane is straightforward and fast. In the previous equation the σ_i are the astrometric uncertainties. These are known on the lens plane, not on the source plane. Therefore, this method is conceptually wrong.

Alternatively, one can define a χ^2 fit statistic on the lens plane. However, this implies that the lens equation has to be solved in the opposite direction, which is numerically much more expensive. The χ^2 is then

$$\chi^2_{img} = \sum_i \left(\frac{\vec{\theta}_i(\vec{\beta}) - \vec{\theta}_i}{\sigma_i} \right) . \tag{5.9}$$

Additional χ^2 variables can be constructed to fit the other observables, but, as we said in the previous section, they provide much less solid constraints than the astrometric data.

Note that even for relatively simple models the number of parameters can be very large. Some parameters define the density profile: for example, the NFW density profile has two free parameters, namely the scale radius r_s and the characteristic density ρ_s. These must be multiplied by the number of lens components. Each of them is also characterized by an ellipticity and a position angle. The external shear also brings some parameter in. For complicated models, the number of parameters grows significantly. Conversely the constraints are usually few.

Another approach is the non-parametric one. The basic idea behind non-parametric mass models is that the effective lens potential and the deflection equations are linear functions of the surface density. As we saw earlier the surface density can be decomposed in multipoles but also in pixels or any other form in which the surface density is represented as a linear combination of density functionals multiplied by unknown coefficients **k**. (Kochanek, 2004; Diego et al., 2005). In any such model the lens equation for image i takes the form

$$\vec{\beta} = \vec{\theta}_i - A_i \mathbf{k} \tag{5.10}$$

where A_i is the matrix that gives the deflection at the position of image i in terms of the coefficients of the surface density decomposition **k**. An example is the following.

Suppose that we observe N_{img} images and that the lens plane has been divided into N_c cells. Each cell contains a mass m_j with $1 \leq j \leq N_c$. Then, we have N_c coefficients which are the masses m_j and the matrix A is a matrix of $2N_{img} \times N_c$ elements casting the mass vector into a vector of displacements angles. The factor 2 in fronts of N_i comes from the fact that the images (and the sources) are identified by two coordinates.

For a lens with N_{img} images of the same source, such a system can be solved exactly if there are enough degrees of freedom in the description of the surface density. For example, if there are two images, we can eliminate the position of the source, obtaining the system of equations

$$\vec{\theta}_1 - \vec{\theta}_2 = (A_1 - A_2)\mathbf{k} \,, \tag{5.11}$$

and we can solve it by taking the inverse of the matrix $A_1 - A_2$:

$$\mathbf{k} = (A_1 - A_2)^{-1}(\vec{\theta}_1 - \vec{\theta}_2) \,. \tag{5.12}$$

Unfortunately there are usually more degrees of freedom than constraints. In the example given above, if the position of the sources are unknown, there are $2N_{img}$ linear equations for $2N_{img} + N_c$ unknowns. In order to identify a suitable solution for such a system, we need to add extra information or impose constraints.

One possibility is that of reducing the number of unknowns by removing the source positions from the unknown category. If the images are known to be multiple images of the same source, this can be achieved by minimizing the spread of the source points. If there are images which are known to derive from different sources, one can make the assumption that these sources are as much compact as possible.

5.1.4 When theory crashes agauints reality: lensing near cusps

We consider now a particular class of images originated by sources close to the cusps of the tangential caustic. Such an image forms at the position $\vec{x}^{(0)}$ close to the tangential critical line. The following conditions must be satisfied:

- given the Fermat potential

$$\phi(\vec{x}, \vec{y}) = \frac{1}{2}(\vec{x} - \vec{y})^2 - \psi(\vec{x}) \tag{5.13}$$

  images form where $\vec{\nabla}\phi = 0$. Thus,

$$\phi_1^{(0)} = 0 = \phi_2^{(0)} \,; \tag{5.14}$$

- $\det A|_0 = 0$ obviously, given that, as said, $\vec{x}^{(0)}$ is close to the critical line. Given that $A_{ij} = \phi_{ij}$,

$$\phi_{11}^{(0)}\phi_{22}^{(0)} - (\phi_{12}^{(0)})^2 = 0 \,; \tag{5.15}$$

- $\text{tr}A \neq 0$, unless the source lays at the interception between the radial and the tangential caustic;

- $(\vec{\nabla}\det A)|_0 \neq 0$, so that $\det A$ changes sign by crossing the critical line;

- the image on the source plane of a vector tangent to the critical line must vanish (definition of cusp). Since $(\vec{\nabla}\det A)|_0$ is normal to the critical line, a tangent vector is obtained by applying a rotation of $\pi/2$, $R(\pi/2)$. If the source is on the

cusp, the image on the source plane of such a vector tangent to the critical line must be

$$A_0 R(\pi/2)(\vec{\nabla} \det A)|_0 = 0 .$$ (5.16)

We choose the coordinate axes such that the image $\vec{x}^{(0)}$ and its source $\vec{y}^{(0)}$ are at the origin, the axes on the lens and on the source planes are parallel and the Jacobian matrix at $\vec{x}_0$ is diagonal $A_{11}^{(0)} \neq 0$, $A_{22}^{(0)} = 0$. This implies that

$$
\begin{aligned}
\phi_{12}^{(0)} &= \phi_{21}^{(0)} = 0 \\
\phi_{11}^{(0)} &\neq 0 \\
\phi_{22}^{(0)} &= 0 .
\end{aligned}
$$ (5.17)

From

$$(\vec{\nabla} \det A)|_0 = \vec{\nabla}[\phi_{11}^{(0)} \phi_{22}^{(0)} - (\phi_{12}^{(0)})^2] \neq 0$$ (5.18)

together with 5.17, we obtain

$$\phi_{111}^{(0)} \phi_{22}^{(0)} + \phi_{11}^{(0)} \phi_{221}^{(0)} - 2\phi_{12}^{(0)} \phi_{121}^{(0)} = \phi_{11}^{(0)} \phi_{221}^{(0)} \neq 0 ,$$ (5.19)

and/or

$$\phi_{112}^{(0)} \phi_{22}^{(0)} + \phi_{11}^{(0)} \phi_{222}^{(0)} - 2\phi_{12}^{(0)} \phi_{122}^{(0)} = \phi_{11}^{(0)} \phi_{222}^{(0)} \neq 0 ,$$ (5.20)

so $\phi_{122}^{(0)}$ and $\phi_{222}^{(0)}$ cannot be both zero.

Moreover,

$$R(\pi/2)(\vec{\nabla} \det A)|_0 = \begin{pmatrix} 0 & -1 \\ 1 & 0 \end{pmatrix} \phi_{11}^{(0)} \begin{pmatrix} \phi_{221}^{(0)} \\ \phi_{222}^{(0)} \end{pmatrix} = \phi_{11}^{(0)} \begin{pmatrix} -\phi_{222}^{(0)} \\ \phi_{122}^{(0)} \end{pmatrix} .$$ (5.21)

Mapping to the source plane, we find

$$
\begin{aligned}
A_0 R(\pi/2)(\vec{\nabla} \det A)|_0 &= \begin{pmatrix} \phi_{11}^{(0)} & 0 \\ 0 & 0 \end{pmatrix} \phi_{11}^{(0)} \begin{pmatrix} -\phi_{222}^{(0)} \\ \phi_{122}^{(0)} \end{pmatrix} \\
&= \phi_{11}^{(0)} \begin{pmatrix} -\phi_{11}^{(0)} \phi_{222}^{(0)} \\ 0 \end{pmatrix} .
\end{aligned}
$$ (5.22)

Given Eq. 5.16, we obtain

$$\phi_{222}^{(0)} = 0$$ (5.23)

and thus

$$\phi_{122}^{(0)} \neq 0 .$$ (5.24)

Summaryzing:

$$\phi_1^{(0)} = \phi_2^{(0)} = \phi_{12}^{(0)} = \phi_{22}^{(0)} = \phi_{222}^{(0)} = 0$$ (5.25)

$$\phi_{11}^{(0)} \neq 0 \neq \phi_{122}^{(0)} ,$$ (5.26)

thus, ϕ near the critical point (cusp point) is

$$
\begin{aligned}
\phi &= \phi^{(0)} + \frac{1}{2}\vec{y}^2 - \vec{x}\vec{y} + \frac{1}{2}\phi_{11}^{(0)}x_1^2 + \frac{1}{6}\phi_{111}^{(0)}x_1^3 + \frac{1}{2}\phi_{112}^{(0)}x_1^2 x_2 \\
&\quad + \frac{1}{2}\phi_{122}^{(0)}x_1 x_2^2 + \frac{1}{24}\phi_{2222}^{(0)}x_2^4 + \dots \, .
\end{aligned}
\tag{5.27}
$$

Images form where $\vec{\nabla}\phi = 0$. Thus,

$$
\begin{aligned}
\partial_1\phi &= -y_1 + \phi_{11}^{(0)}x_1 + \frac{1}{2}\phi_{111}^{(0)}x_1^2 + \phi_{112}^{(0)}x_1 x_2 + \frac{1}{2}\phi_{122}^{(0)}x_2^2 = 0 \\
\partial_2\phi &= -y_2 + \frac{1}{2}\phi_{112}^{(0)}x_1^2 + \phi_{122}^{(0)}x_1 x_2 + \frac{1}{6}\phi_{2222}^{(0)}x_2^3 = 0
\end{aligned}
\tag{5.28}
$$

Then, the lens mapping near the cusp point is (using only the leading terms in x_1 and x_2:

$$
\begin{aligned}
y_1 &= cx_1 - \frac{b}{2}x_2^2 + dx_1 x_2 \\
y_2 &= \frac{d}{2}x_1^2 - bx_1 x_2 - ax_2^3 \, ,
\end{aligned}
\tag{5.29}
$$

where

$$
a = -\frac{1}{2}\phi_{2222}^{(0)}, b = -\phi_{122}^{(0)}, c = \phi_{11}^{(0)}, d = \phi_{112}^{(0)} \, .
\tag{5.30}
$$

The Jacobian matrix is

$$
A = \frac{\partial \vec{y}}{\partial \vec{x}} = \begin{pmatrix} c + dx_2 & dx_1 - bx_2 \\ dx_1 - bx_2 & -bx_1 - 3ax_2^2 \end{pmatrix} \, .
\tag{5.31}
$$

The determinant is

$$
\begin{aligned}
\det A &= -(c + dx_2)(bx_1 + 3ax_2^2) - (dx_1 - bx_2)^2 \\
&= -(cbx_1 + 3acx_2^2 + bdx_1 x_2 + 3adx_2^3) - (d^2 x_1^2 + b^2 x_2^2 - 2bdx_1 x_2) \\
&= -bcx_1 - (3ac + b^2)x_2^2 - d(dx_1^2 - bx_1 x_2 + 3ax_2^3) \, .
\end{aligned}
\tag{5.32}
$$

All term in $\det A$ involving d turn out to be negligible near the origin although this was not obvious before.
The critical curve requires $\det A = 0$, which implies

$$
x_1 = -\frac{1}{bc}(3ac + b^2)x_2^2 \, .
\tag{5.33}
$$

Thus the critical curve is a parabola (red curve in the Fig. on the right).
The caustic curve is obtained from Eq. 5.29:

$$
\begin{aligned}
y_1 &= -\frac{3ac + b^2}{b}x_2^2 - \frac{b}{2}x_2^2 = -\frac{3}{2b}(2ac + b^2)x_2^2 \\
y_2 &= \frac{3ac + b^2}{c}x_2^2 - ax_2^3 = \frac{1}{c}(2ac + b^2)x_2^3
\end{aligned}
\tag{5.34}
$$

Then the caustic is a semicubic parabola (green curve in the Fig. on the right),

$$
y_1^3 = -\frac{27c^2(2ac + b^2)}{8b^3}y_2^2 \, .
\tag{5.35}
$$
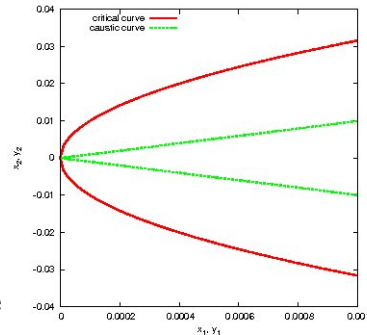
Let us now study the inversion of the lens mapping 5.29 near the cusp. We have:

$$
\begin{aligned}
y_1 &= cx_1 - \frac{b}{2}x_2^2 + dx_1x_2 \\
\Rightarrow \quad & x_1(c + dx_2) = y_1 + \frac{b}{2}x_2^2 \\
\Rightarrow \quad & x_1 = \frac{1}{c + dx_2}\left(y_1 + \frac{b}{2}x_2^2\right) \\
& \approx \frac{1}{c}\left(y_1 + \frac{b}{2}x_2^2\right) ,
\end{aligned}
\tag{5.36}
$$

and

$$
\begin{aligned}
y_2 &= \frac{d}{2} - bx_1x_2 - ax_2^3 \\
&= \frac{d}{2c^2}\left(y_1^2 + by_1x_2^2 + \frac{b^2}{4}x_2^4\right) - \frac{b}{c}\left(y_1x_2 + \frac{b}{2}x_2^3\right) - ax_2^3 \\
&= \frac{d}{2c^2}\left(y_1^2 + by_1x_2^2 + \frac{b^2}{4}x_2^4\right) - x_2^3\left(a + \frac{b^2}{2c}\right) - \frac{b}{c}y_1x_2 \\
\Rightarrow \quad & x_2^3\frac{2ac + b^2}{2c} + y_2 + \frac{b}{c}y_1x_2 - \frac{d}{2c^2}\left(y_1^2 + by_1x_2^2 + \frac{b^2}{4}x_2^4\right) = 0 .
\end{aligned}
\tag{5.37}
$$

Neglecling the last term, we obtain

$$
x_2^3 + \frac{2cy_2}{2ac + b^2} + \frac{2by_1x_2}{2ac + b^2} = 0 .
\tag{5.38}
$$

The second of these equations is in third order in x_2 and can be solved analytically. This solution can then be inserted in Eq. 5.36 to yead x_1. The number of solutions of Eq. 5.38 depends on the discriminant Δ,

$$
\Delta = \frac{1}{(2ac + b^2)^2}\left[c^2y_2^2 + \frac{8}{27}\frac{b^3y_1^3}{2ac + b^2}\right] .
\tag{5.39}
$$

If $\Delta < 0$ three real solutions exist. This correspond to the case of a source inside the caustic. If $\Delta > 0$ only one real solution exists, which correspond to the case of a source outside the caustic. If $\Delta = 0$, two solutions merge. It can be easily seen that

$$
\Delta = 0 \Rightarrow y_1^3 = -\frac{27c^2(2ac + b^2)}{8b^3}y_2^2 ,
\tag{5.40}
$$

which is the equation of the caustic curve. Thus, two images disappear when the source crosses the caustic curve. The caustic separates the regions of one and three solutions on the source plane.

Since the general solution of Eqs. 5.36 and 5.38 is very complicated, we restrict to the special case $y_2 = 0$, when the source is located on the symmetry axis of the cusp. Then,

$$
\begin{aligned}
x_2^3 + \frac{2by_1x_2}{2ac + b^2} &= 0 \\
\Rightarrow \quad & x_2 = 0 \text{ or } x_2^2 + \frac{2by_1}{2ac + b^2} = 0 \\
\Rightarrow \quad & x_2 = 0 \text{ or } x_{2\pm} = \frac{1}{2}\left[\pm\sqrt{-\frac{8by_1}{2ac + b^2}}\right] \\
\Rightarrow \quad & x_2 = 0 \text{ or } x_{2\pm} = \left[\pm\sqrt{-\frac{2by_1}{2ac + b^2}}\right] .
\end{aligned}
\tag{5.41}
$$

- If $x_2 = 0$, $x_1 = \frac{y_1}{c}$ (from Eq. 5.36);

- if $x_2 = \pm\sqrt{-\frac{2by_1}{2ac+b^2}}$, $x_1 = \frac{y_1}{c} - \frac{b}{2c}\frac{2by_1}{2ac+b^2} = \frac{2ay_1}{2ac+b^2}$;

- thus, images form at

$$\left(\frac{y_1}{c}, 0\right) \; ; \left(\frac{2ay_1}{2ac+b^2}, \pm\sqrt{-\frac{2by_1}{2ac+b^2}}\right) . \tag{5.42}$$

The magnifications are given by the inverse of the Jacobian determinant,

$$\det A = -bcx_1 - (3ac+b^2)x_2^2 . \tag{5.43}$$

- For image 1:

$$\det A = -by_1 ; \tag{5.44}$$

- for image 2:

$$\begin{aligned}
\det A &= -\frac{2abcy_1}{2ac+b^2} + (3ac+b^2)\frac{2by_1}{2ac+b^2} \\
&= \frac{(-2abc+6abc+2b^3)y_1}{2ac+b^2} = \frac{2by_1(b^2+2ac)}{2ac+b^2} \\
&= 2by_1 ,
\end{aligned} \tag{5.45}$$

which is valid also for image 3.

Thus:

$$\mu^{(1)} = -\frac{1}{by_1} \; ; \quad \mu^{(2)} = \frac{1}{2by_1} = \mu^{(3)} \tag{5.46}$$

$$\mu^{(1)} + \mu^{(2)} + \mu^{(3)} = 0 \qquad \text{signed magnifications} \tag{5.47}$$

$$|\mu^{(2)}| = \frac{1}{2}|\mu^{(1)}| \qquad \text{unsigned magnifications} \tag{5.48}$$

CASTLES

Thus, for cusp lenses we expect the three brightest images to satisfy these conditions. In fold lenses, analogous relations can be found for the two brightest images. What happens in reality? Unfortunately none of the systems observed so far show flux ratios in agreement with the theoretical expectations. For example, the famous quadruple quasar B1422+231 (Patnaik et al., 1992) displayed on the right strongly violates these rules. The three brightest images are labeled in Patnaik et al. (1992) A,B and C. B is the brightest images. In our previous discussion it corresponds to the image 1 (inside the critical line). The images A and C correspond to the images 2 and 3, which are outside the critical curve. Based on the theoretical expectations, the flux ratios A/B and C/B should be ~ 0.5,
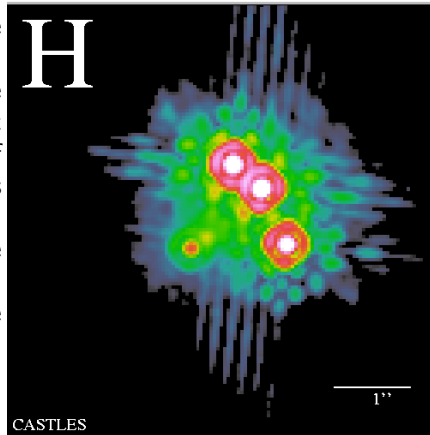
while the flux ratio A/C should be ~ 1. Instead, VLBA observations of this system found

$$\frac{A}{B} \sim 0.9$$
$$\frac{C}{B} \sim 0.5$$
$$\frac{C}{A} \sim 0.5 .$$

Many authors have attempted at finding a solution to this problem. For example, Mao & Schneider (1998) suggested that such anomalies may be due to substructures in the lenses. However, recently Mao et al. (2004) using numerical simulations found that at typical image positions the fraction of the surface density in substructures is $< 0.5\%$ in a ΛCDM cosmology. Such low fraction seems lower than required to explain the flux anomalies observed in B1422+231 and in other systems (e.g. B2045+265, B0712+472, B1933+503). The problem of the "flux anomalies" in lenses quasars is still unresolved. Generally, mass models can be found which fit very well all the observables but they fail at reproducing the flux ratios between the images.

5.1.5 General results from strong lensing

Galaxies

The are about 70 cases of strong lensing by galaxies now known. Most of them have two or four images, but a few have higher image numbers. Several important properties of these lenses have been revealed thanks to lensing. Some of the them are:

- image splittings allow the projected mass to be constrained which is enclosed by the images. In particular, galaxy lensing suggests that galaxies have inner density profiles near to isothermal (Rusin et al., 2003). For example, we have seen in the previous Chapter that gravitational lenses are expected to produce odd number of images, unless the surface-mass distribution has a steep inner density profile. All but very few observed galaxy-lens systems have an even image number, most of them either two or four, as required by isothermal density profiles;

- the time delay between images of the same source, can be measured if the source is instrinsically variable. The same features then are repeated in the light curves of all the images but shifted in time. If a model for the lens mass distribution is given, the time delay can be used to measure the Hubble constant. The most recent determinations of H_0 via lensing, $H_0 = 75^{+7}_{-6}$km s^{-1} Mpc^{-1} (Koopmans et al., 2003), are in agreement with the HST Key Project results, which give $H_0 = (72 \pm 8)$km s^{-1} Mpc^{-1} and with the WMAP constraints, $H_0 = (74 \pm 3)$km s^{-1} Mpc^{-1};

- the observed abundance of quadruples is particularly large, comparable to that of doubles. Such a large fraction of quads supports the view that galaxy lenses contain substructures, which contribute to the shear field in the lens, pushing the critical lines into regions of low density and then extending the lensing cross sections for quadruples. The large scale structure indeed seems to provide insufficient external shear for explaining the observed frequency of quadruples.

Clusters

Much can be learned on clusters studying the arcs that some of them produce:

- there must be more matter in clusters that what is contained in their galaxies, and that dark matter must be more smoothly distribute; otherwise, arcs would appear smaller and more strongly curved;

- prominent counter-arcs are often missing, thus clusters cannot typically be symmetric;

- arcs are thin, thus cluster density profiles must be steep; this can be seen as follows: for critical curves to appear, we need $\kappa \sim 1$ in the core; the radial magnification of a tangential arc is

$$\mu_r = \frac{1}{1 - \kappa + \gamma} \ , \tag{5.49}$$

while $1 - \kappa - \gamma = 0 \Rightarrow \gamma = (1 - \kappa)$. Thus

$$\mu_r = \frac{1}{2(1 - \kappa)} \ . \tag{5.50}$$

Thin arcs require $\mu_r \lesssim 1$, which implies $\kappa \lesssim 1/2$. Thus, the density profile must be steep enough to drop from $\kappa \sim 1$ to $\kappa \sim 1/2$ within $\sim \theta_E$;

- cluster cores, if they exist, need to be small, because otherwise no arcs would be formed, or radial arcs would be at much larger cluster centric distances;

- substructures need to be abundant in galaxy clusters, because otherwise "straight arcs" could not appear;

- the simple estimates of cluster properties using arcs, radial or tangential, are complicated in reality by cluster substructures or asymmetries; shear plays and important role.

5.2 Weak lensing

5.2.1 Weak lensing by galaxy clusters

Due to the very high number density of distant galaxies, clusters appear placed in front of a "cosmic wallpaper", which they distort in a very characteristic way. There are about 30-40 galaxies per square arcmin of the sky (but in deep space observations the amazing density of 80-100 galaxies per square arcmin has been reached!), thus approximately 20000 of them on the face of the full moon. Can the distortions imprinted on these galaxies by clusters be used for reconstructing cluster mass distributions?

While source sizes are unknown individually, source shapes can more easily be measured. Although sources are intrinsically irregulars, their large number allows averaging over several of them. Assuming that they are intrinsically randomly oriented, the average over their shapes should become circular.

If lensing is weak, the image of a circular source appears elliptical, with axes given by

$$\frac{r}{1 - \kappa - \gamma} \quad , \quad \frac{r}{1 - \kappa + \gamma} \ , \tag{5.51}$$

assuming $\kappa, \gamma \ll 1$. Defining the ellipticity as

$$\epsilon = \frac{a - b}{a + b} = \frac{2\gamma}{2(1 - \kappa)} = \frac{\gamma}{1 - \kappa} \approx \gamma \tag{5.52}$$

in the limit of weak lensing, i.e. the ellipticity directly measures the shear.

Like the shear, the ellipticity has two components, an orientation and a magnitude, which we can write as

$$\epsilon_1 = \epsilon \cos 2\phi \tag{5.53}$$
$$\epsilon_2 = \epsilon \sin 2\phi . \tag{5.54}$$

Note the dependence on 2ϕ rather than ϕ, which illustrates that an ellipse is symmetric under rotations by π rather than 2π.

Let the intrinsic source ellipticity be $\epsilon^{(s)}$, then, in the weak-lensing limit,

$$\epsilon_i = \epsilon_i^{(s)} + \gamma_i = \epsilon^{(s)} \begin{pmatrix} \cos 2\phi \\ \sin 2\phi \end{pmatrix} + \begin{pmatrix} \gamma_1 \\ \gamma_2 \end{pmatrix} ; \tag{5.55}$$

averaging over sufficiently many sources, the first term disappears and

$$\langle \epsilon \rangle = \langle \gamma \rangle . \tag{5.56}$$

Suppose now that we know γ at many positions $\vec{\theta}$ across a cluster, how can we find the mass distribution? The key is the relation between both γ and κ and the lensing potential ψ. If we transform ψ γ and κ to Fourier space, we find

$$\kappa = \frac{1}{2}(\psi_{11} + \psi_{22}) \quad \Rightarrow \quad \hat{\kappa} = -\frac{1}{2}(k_1^2 + k_2^2)\hat{\psi} \tag{5.57}$$

$$\gamma_1 = \frac{1}{2}(\psi_{11} - \psi_{22}) \quad \Rightarrow \quad \hat{\gamma}_1 = -\frac{1}{2}(k_1^2 - k_2^2)\hat{\psi} \tag{5.58}$$

$$\gamma_2 = \psi_{12} \quad \Rightarrow \quad \hat{\gamma}_2 = -k_1 k_2 \hat{\psi} , \tag{5.59}$$

where $\vec{k}$ is a wave vector conjugate to the angular position vector $\vec{\theta}$. From these relations, we can eliminate $\hat{\psi}$. Noting that

$$\left[k^{-2} \begin{pmatrix} k_1^2 - k_2^2 \\ 2k_1 k_2 \end{pmatrix} \right] [k^{-2}(\ k_1^2 - k_2^2 \quad 2k_1 k_2 \ )] = 1 \tag{5.60}$$

and writing

$$\begin{pmatrix} \hat{\gamma}_1 \\ \hat{\gamma}_2 \end{pmatrix} = k^{-2} \begin{pmatrix} k_1^2 - k_2^2 \\ 2k_1 k_2 \end{pmatrix} \hat{\kappa} , \tag{5.61}$$

we find immediately

$$\hat{\kappa} = k^{-2}(\ k_1^2 - k_2^2 \quad 2k_1 k_2 \ ) \begin{pmatrix} \hat{\gamma}_1 \\ \hat{\gamma}_2 \end{pmatrix} = k^{-2}[(k_1^2 - k_2^2)\hat{\gamma}_1 + 2k_1 k_2 \hat{\gamma}_2] \tag{5.62}$$

As a product in Fourier space, we can equally well write the result as a convolution in real space, using the Fourier convolution theorem,

$$\widehat{(f * g)} = \hat{f}\hat{g} . \tag{5.63}$$

This yealds, in real space,

$$\kappa(\vec{\theta}) = \frac{1}{\pi} \int d^2\theta' [D_1(\vec{\theta} - \vec{\theta}')\gamma_1 + D_2(\vec{\theta} - \vec{\theta}')\gamma_2] , \tag{5.64}$$

with

$$D_1(\vec{\theta}) = \frac{\theta_2^2 - \theta_1^2}{\theta^4} \tag{5.65}$$

$$D_2(\vec{\theta}) = \frac{2\theta_1 \theta_2}{\theta^4} . \tag{5.66}$$

In that way, mass maps of galaxy clusters can be constructed from shear measurements. However, there are numerous problems in detail, which can all be overcome to some degree. First of all, ellipticities measure

$$\left\langle \frac{\gamma}{1-\kappa} \right\rangle = \langle g \rangle \; , \tag{5.67}$$

the so-called *reduced* shear, rather than the shear alone. This can be overcome by writing

$$\gamma = g(1-\kappa) \tag{5.68}$$

and using that in the convolution equation, thus

$$\kappa(\vec{\theta}) = \frac{1}{\pi} \int \mathrm{d}^2\theta' [D_1(\vec{\theta}-\vec{\theta}')g_1(1-\kappa) + D_2(\vec{\theta}-\vec{\theta}')g_2(1-\kappa)] \; , \tag{5.69}$$

which can be solved analytically starting from $\kappa = 0$.

Formally, the convolution for κ extends over all of two-dimensional space, while real data fields are finite. In practice, this leads to a bias if the field is small, but modern data fields are large enough for the method to work straightforwardly.

A problem of principle arises because the Jacobian can be transformed by multiplying it with a factor $\lambda \neq 0$,

$$A \quad \rightarrow \quad \lambda A \equiv A' \; , \tag{5.70}$$

without the ellipticity measurements noticing it. Scaling the Jacobian in that way simply enlarges the sources, but does not change their shape. Thus, such transformations leave the shear signal invariant. Thus, transformations like

$$1 - \kappa' = \lambda(1-\kappa) \Rightarrow \kappa' = 1 - \lambda + \lambda\kappa \tag{5.71}$$

cannot be detected, and κ is only determined up to such trasformations. For $\lambda = 1 - \delta \approx 1$,

$$\kappa' \approx \delta + \kappa \; , \tag{5.72}$$

which corresponds to adding a sheet of constant surface mass density to the lens. Therefore, this invariance has been called the *mass sheet degeneracy*.

There are other techniques for cluster reconstruction which can in principle avoid the mass sheet degeneracy. Among them are the maximum-likelihood techniques. Suppose shear measurements are given on a cluster field, then the goal is to search a lensing potential ψ such as to reproduce the shear. This can be done by minimizing

$$\chi^2 = \sum_{pixels} \frac{[\gamma_1 - \gamma_1(\psi)]^2 + [\gamma_2 - \gamma_2(\psi)]^2}{2\sigma_\gamma^2} \; , \tag{5.73}$$

where $\gamma_1(\psi)$ and $\gamma_2(\psi)$ are the usual relations between shear and potential. This minimization leads to an estimate for ψ at each point where a shear value has been measured.

Additional information can now be added. Suppose we have a means to estimate galaxy sizes, then the magnification is given by

$$\mu = \frac{\mathrm{d}^2\Omega_{\text{lensed}}}{\mathrm{d}^2\Omega_{\text{unlensed}}} \; . \tag{5.74}$$

For weak lensing, the inverse magnification is

$$R = \frac{1}{\mu} = (1 - \kappa)^2 - \gamma^2 \approx 1 - 2\kappa \ . \tag{5.75}$$

This can then be incorporated into χ^2:

$$\chi^2 = \sum_{pixels} \left\{ \frac{[\gamma_1 - \gamma_1(\psi)]^2 + [\gamma_2 - \gamma_2(\psi)]^2}{2\sigma_\gamma^2} + \frac{[R - R(\psi)]^2}{2\sigma_R^2} \right\} \ , \tag{5.76}$$

which is now no longer invariant under the mass sheet transformation.

In practice smoothing is required to suppress the noise in the data (shot noise, intrinsic ellipticity) to a desired level.

5.2.2 Galaxy-galaxy lensing

Faint background galaxies are also lensed by brighter foreground galaxies. Although the effect is certainly weak, galaxies can be superposed to enhance the signal.

Let $p^{(s)}(\epsilon)$ be the intrinsic distribution of source ellipticities. The shear caused by a lens changes the ellipticity to

$$\epsilon \rightarrow \epsilon + \gamma \ , \tag{5.77}$$

thus, the observed distribution of image ellipticities is

$$p(\epsilon) = p^{(s)}(\epsilon - \gamma) \approx p^{(s)}(\epsilon) - \gamma_i \left(\frac{\partial p^{(s)}}{\partial \epsilon_i} \right)(\epsilon) \ . \tag{5.78}$$

We introduce now two angles: a position angle of the lensed galaxy with respect to the lens, α, and the angle between the major axis of the lensed galaxy and the line connecting it with the lens, ϕ.

Without loss of generality, we can rotate the coordinate system such that $\alpha = 0$. Then, we are in the principal axis system of the shear, such that

$$\gamma_1' = -\gamma_t = \gamma_1 \cos 2\alpha + \gamma_2 \sin 2\alpha \ , \tag{5.79}$$
$$\gamma_2' = 0 \tag{5.80}$$

We have defined the tangential component of the shear here as

$$\gamma_t = -(\gamma_1 \cos 2\alpha + \gamma_2 \sin 2\alpha) \ . \tag{5.81}$$

The example of a singular isothermal sphere shows that this definition is indeed useful. There, we had

$$\gamma_1 = -\gamma \cos 2\alpha \tag{5.82}$$
$$\gamma_2 = -\gamma \sin 2\alpha \ , \tag{5.83}$$

such that

$$\gamma_t = -[-\gamma \cos^2 2\alpha - \gamma \sin^2 2\alpha] = \gamma \ . \tag{5.84}$$

Note again that the shear components are elements of a 2×2 tensor, so that they transform under rotations as

$$\begin{aligned}
\begin{pmatrix} \gamma_1' & \gamma_2' \\ \gamma_2' & -\gamma_1' \end{pmatrix} &= \begin{pmatrix} \cos\alpha & \sin\alpha \\ -\sin\alpha & \cos\alpha \end{pmatrix} \begin{pmatrix} \gamma_1 & \gamma_2 \\ \gamma_2 & -\gamma_1 \end{pmatrix} \begin{pmatrix} \cos\alpha & -\sin\alpha \\ \sin\alpha & \cos\alpha \end{pmatrix} \\
&= \begin{pmatrix} \gamma_1 \cos 2\alpha + \gamma_2 \sin 2\alpha & -\gamma_1 \sin 2\alpha + \gamma_2 \cos 2\alpha \\ -\gamma_1 \sin 2\alpha + \gamma_2 \cos 2\alpha & -\gamma_1 \cos 2\alpha - \gamma_2 \sin 2\alpha \end{pmatrix}
\end{aligned} \tag{5.85}$$

We now return to the probability distribution of the image ellipticity, $p(\epsilon)$. The derivatives of the intrinisc ellipticity distribution can be written as

$$\left(\frac{\partial p}{\partial \epsilon_1}, \frac{\partial p}{\partial \epsilon_2}\right) \rightarrow \frac{\partial p}{\partial \epsilon} \cos 2\phi \tag{5.86}$$

in the principal axis frame of the shear, assuming that ellipticities are intrinsically isotropic, such that $\partial p / \partial \phi = 0$. Then

$$p(\epsilon) = p^{(s)}(\epsilon) + \gamma_t \cos 2\phi \frac{\partial p^{(s)}}{\partial \epsilon} . \tag{5.87}$$

Integrating now over $\int_0^\infty \epsilon d\epsilon$ in order to find the angle distribution of the images, we find

$$\begin{aligned}
p(\phi) &= \frac{2}{\pi} + \gamma_t \cos 2\phi \int_0^\infty \epsilon d\epsilon \frac{\partial p^{(s)}}{\partial \epsilon} \\
&= \frac{2}{\pi} - \gamma_t \cos 2\phi \int_0^\infty \epsilon d\epsilon \frac{1}{\epsilon} p^{(s)}(\epsilon) \\
&= \frac{2}{\pi} \left[1 - \gamma_t \cos 2\phi \left\langle \frac{1}{\epsilon^{(s)}} \right\rangle \right] .
\end{aligned} \tag{5.88}$$

here, the factors $2/\pi$ arise from the fact that $p(\phi)$ must be normalised when integrating ϕ from 0 to $\pi/2$, because it suffices to restrict the angle ϕ to that interval.

Thus, galaxy-galaxy lensing modifies the distribution of the position angles of the lensed galaxies to

$$p(\phi) = \frac{2}{\pi} \left[1 - \langle \gamma_t \rangle \cos 2\phi \left\langle \frac{1}{\epsilon^{(s)}} \right\rangle \right] , \tag{5.89}$$

where $\langle \gamma_t \rangle$ is the mean tangential shear of an ensemble of lensing galaxies. $p(\phi)$ can be observed once an estimate for $\langle 1/\epsilon^{(s)} \rangle$ is known, which can be directly inferred from observed galaxy images. Then, $\langle \gamma_t \rangle$ can be estimated and lens galaxy properties can be derived from it.

6 Lensing by large-scale structures

6.1 Light propagation through an inhomogeneous universe

In unperturbed spacetime, light travels alog null geodesic lines of the symmetric, homogenous and isotropic Friedmann-Lemaitre space-time.

In contrast to the earlier treatment, we have to take into account that lenses can now be of comparable size to the curvature scale of the universe, thus we need to refine the picture of straight light paths which are instantly deflected by sheet-like, thin lenses.

Starting from null geodesic in space-time, it can be shown that light rays propagate through the unperturbed Friedmann-Lemaitre spacetime such that the comoving separation vector $\vec{x}$ between them changes with the radial coordinate w as

$$\frac{\mathrm{d}^2\vec{x}}{\mathrm{d}w^2} + K\vec{x} = 0 \ , \tag{6.1}$$

where $K = (H_0/c)^2(\Omega_0 + \Omega_\Lambda - 1)$ is the curvature parameter of the universe. Note that c/H_0 is the Hubble length, so K has the unit of an inverse squared length, as it has to be.

Ω_0 is the density parameter of the universe today,

$$\Omega_0 = \left(\frac{3H_0^2}{8\pi G}\right)^{-1}\rho_0 \ , \tag{6.2}$$

while Ω_Λ is the density parameter corresponding to the cosmological constant,

$$\Omega_\Lambda = \frac{\Lambda}{3H_0^2} \ . \tag{6.3}$$

H_0 is the Hubble constant. According to present knowledge, $\Omega_0 \approx 0.3$, $\Omega_\Lambda \approx 0.7$ and $K \approx 0$.

Comoving means that the physical separation $\vec{r}$ between the rays is divided by the scale factor of the universe,

$$\vec{x} = \frac{\vec{r}}{a} \tag{6.4}$$

in order to get rid of the expansion of space-time.

The metric is written as

$$ds^2 = c^2dt^2 - a^2[dw^2 + f_K^2(w)d^2\Omega] \ , \tag{6.5}$$

such that dw is the radial, comoving distance element, and $f_K(w)$ is given by

$$f_K(w) = \begin{cases} \frac{1}{\sqrt{K}} \sin(\sqrt{K}w) & (K > 0) \\ w & (K = 0) \\ \frac{1}{\sqrt{-K}} \sinh(\sqrt{-K}w) & (K < 0) \end{cases} \qquad (6.6)$$

The propagation equation is easily solved. It is an oscillator equation, so that its general solution is

$$\vec{x} = \vec{A} \cos \sqrt{K}w + \vec{B} \sin \sqrt{K} \qquad (K > 0) . \qquad (6.7)$$

With the boundary conditions $\vec{x}(w = 0) = 0$ and $\mathrm{d}\vec{x}/\mathrm{d}w|_{w=0} = \vec{\theta}$, we find

$$\vec{x}(w) = \vec{\theta} \sin \sqrt{K}w . \qquad (6.8)$$

Generally, for negative and vanishing K, we find

$$\vec{x}(w) = \vec{\theta} f_K(w) . \qquad (6.9)$$

These solutions have a very simple interpretation: obviously, for $K = 0$, $\vec{x} = \vec{\theta}w$, as we know in Euclidean space. For positive or negative curvature, the light rays approach each other, or depart from each other compared to the flat case, as the meridional lines on a sphere or a hyperboloid do.

Adding perturbations is simple considering that the lensing masses are typically much smaller than the Hubble radius. Then, space-time can be considered flat in their surroundings, and we can use our earlier result on the deflection angle in the form

$$\frac{\mathrm{d}^2\vec{x}}{\mathrm{d}w^2} = -\frac{2}{c^2} \vec{\nabla}_\perp \phi , \qquad (6.10)$$

where it must now be noted that the perpendicular gradient of ϕ must be taken with respect to the comoving coordinates as well. This means

$$\vec{\nabla}_\perp \phi = \frac{1}{f_K(w)} \vec{\nabla}_{\vec{\theta}} \phi . \qquad (6.11)$$

The propagation equation changes to

$$\frac{\mathrm{d}\vec{x}}{\mathrm{d}w^2} + K\vec{x} = -\frac{2}{c^2} \vec{\nabla}_\perp \phi , \qquad (6.12)$$

which now incorporates overall space-time curvature and local perturbations caused by a potential ϕ.

The inhomogeneus oscillator equation can be solved by constructing a Greens function $G(w, w')$, which is defined on the square $0 \le w \le w_s$, $0 \le w' \le w_s$, where w_s is the coordinate distance to the source.
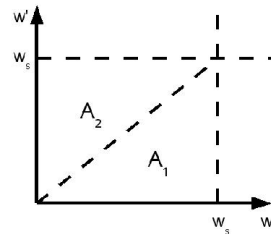
According to the definition of a Green function, $G(w, w')$ must satisfy the following conditions

- $G(w, w')$ is continously differentaible in both triangles $A_{1,2}$ and satisfies the homogeneous differential equation

$$\frac{\mathrm{d}^2 \vec{x}}{\mathrm{d}w^2} + K\vec{x} = 0 \; ; \tag{6.13}$$

- $G(w, w')$ is continous on the entire square;

- the derivative of $G(w, w')$ with respect to w jumps by 1 on the boundary between A_1 and A_2;

- as a function of w, $G(w, w')$ satisfies the homogeneous boundary conditions on the solution.

Accordingly, we set up

$$G(w, w') = \begin{cases} A(w')\cos\sqrt{K}w + B(w')\sin\sqrt{K}w & \text{on } A_1 \\ C(w')\cos\sqrt{K}w + D(w')\sin\sqrt{K}w & \text{on } A_2 \end{cases} . \tag{6.14}$$

The homogeneous boundary conditions demand $A = B = 0$.
Continuity requires

$$C\cos\sqrt{K}w' + D\sin\sqrt{K}w' = 0 \; , \tag{6.15}$$

and the jump in the derivative implies

$$-C\sin\sqrt{K}w' + D\cos\sqrt{K}w' = \frac{1}{\sqrt{K}} \; . \tag{6.16}$$

Thus,

$$C = -\frac{1}{\sqrt{K}}\sin\sqrt{K}w' \tag{6.17}$$

$$D = \frac{1}{\sqrt{K}}\cos\sqrt{K}w' \; . \tag{6.18}$$

This implies

$$G(w, w') = \begin{cases} 0 & (w < w') \\ \frac{1}{\sqrt{K}}\sin\sqrt{K}(w - w') & (w > w') \end{cases} . \tag{6.19}$$

More generally, i.e. for arbitrary sign of K, we find instead

$$G(w, w') = \begin{cases} 0 & (w < w') \\ f_K(w - w') & (w > w') \end{cases} . \tag{6.20}$$

Therefore the general solution of the propagation equation reads

$$\vec{x} = f_K(w)\vec{\theta} - \frac{2}{c^2}\int_0^w \mathrm{d}w' f_K(w - w')\vec{\nabla}_\perp\phi \; . \tag{6.21}$$

As in the single-lens plane approach, we evaluate this integral along the unperturbed path $f_K(w)\vec{\theta}$.
The deflection angle is defined as the deviation between the perturbed and the unperturbed path,

$$\vec{\alpha} = \frac{f_K(w)\vec{\theta} - \vec{x}}{f_K(w)} = \frac{2}{c^2}\int_0^w \mathrm{d}w' \frac{f_K(w - w')}{f_K(w)}\vec{\nabla}_\perp\phi[f_K(w')\vec{\theta}, w'] \; . \tag{6.22}$$

This is now the deflection angle accumulated along a light path propagating into direction $\vec{\theta}$ out to the coordinate distance w. Hence, we denote it as $\vec{\alpha}(\vec{\theta}, w)$.

For a spatially flat universe, $K = 0$ and $f_K(w) = w$. Then,

$$
\begin{aligned}
\vec{\alpha}(\vec{\theta}, w) &= \frac{2}{c^2} \int_0^w \mathrm{d}w' \left(1 - \frac{w'}{w}\right) \vec{\nabla}_\perp \phi(w'\vec{\theta}, w') \\
&= \frac{2w}{c^2} \int_0^1 \mathrm{d}y (1 - y) \vec{\nabla}_\perp \phi(wy\vec{\theta}, wy) \ .
\end{aligned}
\tag{6.23}
$$

6.2 Effective convergence

In the single lens-plane case, the convergence is one half the divergence of $\vec{\alpha}$. Analogously, we define here an effective convergence for large-scale structure lenses,

$$
\begin{aligned}
\kappa_{\mathrm{eff}}(\vec{\theta}, w) &= \frac{1}{2} \vec{\nabla}_{\vec{\theta}} \vec{\alpha}(\vec{\theta}, w) \\
&= \frac{1}{c^2} \int \mathrm{d}w' \frac{f_K(w') f_K(w - w')}{f_K(w)} \triangle^{(2)} \phi[f_K(w')\vec{\theta}', w'] \ ,
\end{aligned}
\tag{6.24}
$$

where $\triangle^{(2)}$ is the two-dimensional Laplacian with respect to comoving coordinates,

$$
\triangle^{(2)} = \vec{\nabla}_\perp^2 = \frac{\partial^2}{\partial x^2} + \frac{\partial^2}{\partial y^2} \ .
\tag{6.25}
$$

We now do the same as we did when we introduced the lensing potential: we replace

$$
\triangle^{(2)} \to \triangle = \frac{\partial^2}{\partial x^2} + \frac{\partial^2}{\partial y^2} + \frac{\partial^2}{\partial z^2} \ ,
\tag{6.26}
$$

and assume that $\partial\phi/\partial z = 0$ at the boundaries of the perturbations. Then, we can write

$$
\kappa_{\mathrm{eff}} = \frac{1}{c^2} \int_0^w \mathrm{d}w' \frac{f_K(w') f_K(w - w')}{f_K(w)} \triangle\phi(f_K(w')\vec{\theta}, w') \ ,
\tag{6.27}
$$

and substitute for $\triangle\phi$ using Poisson's equation.

In its original form, Poisson's equation reads

$$
\triangle_r \phi = 4\pi G \rho \ ,
\tag{6.28}
$$

where the Laplacian is now taken with respect to physical coordinates. Introducing the density contrast

$$
\delta \equiv \frac{\rho - \overline{\rho}}{\overline{\rho}} \ ,
\tag{6.29}
$$

we can write

$$
\triangle\phi = 4\pi G\overline{\rho}(1 + \delta)a^2 = 4\pi G\overline{\rho}_0 a^{-1}(1 + \delta) \ ,
\tag{6.30}
$$

where we have inserted $\overline{\rho}a^{-3}$ as for ordinary (non-relativistic) matter. Decoupling the potential into a background potential

$$
\triangle\overline{\phi} = 4\pi G\overline{\rho}_0 a^{-1} \ ,
\tag{6.31}
$$

and a peculiar (perturbing) potential ϕ, we have

$$\triangle\phi = 4\pi G\bar{\rho}_0 a^{-1}\delta \; . \tag{6.32}$$

Using further

$$\bar{\rho}_0 = \Omega_0 \frac{3H_0^2}{8\pi G} \tag{6.33}$$

yields the Poisson equation that we need,

$$\triangle\phi = \frac{3}{2}H_0^2\Omega_0 \frac{\delta}{a} \; . \tag{6.34}$$

The effective convergence can then be written as

$$\kappa_{\text{eff}}(\vec{\theta}, w) = \frac{3\Omega_0}{2}\left(\frac{H_0}{c}\right)^2 \int_0^w \mathrm{d}w' \frac{f_K(w')f_K(w-w')}{f_K(w)}\frac{\delta[f_K(w')\vec{\theta}, w']}{a} \; . \tag{6.35}$$

Notice the similarity of the distance factor with the factor $D_{\text{L}}D_{\text{LS}}/D_{\text{S}}$ that we had in the single-lens case.

If the sources are distributed in redshift or, equivalently, in coordinate distance w, the mean effective convergence is

$$\langle\kappa_{\text{eff}}\rangle(\vec{\theta}) = w\int_0^{w_H} \mathrm{d}w G(w)\kappa_{\text{eff}}(\vec{\theta}, w) \; , \tag{6.36}$$

where $G(w)\mathrm{d}w$ is the probability to find a source within $\mathrm{d}w$ of w. Then we can write

$$\langle\kappa_{\text{eff}}\rangle(\vec{\theta}) = \frac{3H_0^2\Omega_0}{2c^2}\int_0^{w_H} \mathrm{d}w W(w)f_K(w)\frac{\delta[f_K(w)\vec{\theta}, w]}{a(w)} \; , \tag{6.37}$$

with the effective weight function

$$W(w) = \int_w^{w_H} \mathrm{d}w'G(w')\frac{f_K(w'-w)}{f_K(w')} \; . \tag{6.38}$$

6.3 Limber's equation

It is impossible to predict exactly which density fluctuations a light ray will find on its way. Concerning the effective convergence, we thus need a statistical approach.

We want to compute the correlation function

$$\langle\kappa(\vec{\theta})\kappa(\vec{\theta}+\vec{\phi})\rangle_{\vec{\theta}} = \xi_\kappa(\phi) \; , \tag{6.39}$$

in which the average extends over all positions $\vec{\theta}$ on the sky, and over all directions of the separation vector $\vec{\phi}$. Due to isotropy, the result cannot depend on the direction of $\vec{\phi}$.

It is typically more convenient to go into Fourier space and to use the power spectrum instead. Suppose we have a function $g(x)$ of n-dimensional space, whose correlation function is

$$\xi_{gg}(y) = \langle g(x)g(x+y)\rangle_x \; . \tag{6.40}$$

We Fourier transform $g(x)$,

$$\hat{g}(k) = \int \mathrm{d}^n x g(x) \exp{(ikx)} \qquad g(x) = \int \frac{\mathrm{d}^n k}{(2\pi)^n} \hat{g}(k) \exp{(-ikx)} \qquad (6.41)$$

and compute the correlation function in Fourier space,

$$
\begin{aligned}
\langle \hat{g}(k)\hat{g}^*(k') \rangle &= \left\langle \int \mathrm{d}^n x g(x) \exp{(ikx)} \int \mathrm{d}^n x' g(x') \exp{(-ik'x')} \right\rangle \\
&= \int \mathrm{d}^n x \exp{(ikx)} \int \mathrm{d}^n x' \exp{(-ik'x')} \langle g(x)g(x') \rangle .
\end{aligned} \qquad (6.42)
$$

Inserting $y + x = x'$ and using the isotropy of the correlation function, we can continue to compute

$$
\begin{aligned}
\langle \hat{g}(k)\hat{g}^*(k') \rangle &= \int \mathrm{d}^n x \exp{[i(k-k')x]} \int \mathrm{d}^n y \exp{(-ik'y)}\xi_{gg}(y) \\
&= (2\pi)^n \delta_D^{(n)}(k-k')P_g(k) ,
\end{aligned} \qquad (6.43)
$$

where we have defined the power spectrum

$$P_g(k) \equiv \int \mathrm{d}^n y \exp{(-iky)}\xi_{gg}(y) \qquad (6.44)$$

as the Fourier transform of the correlation function. $\delta_D^{(n)}$ is the Dirac delta function in n dimensions.

Suppose we are given the power spectrum of a three-dimensional function $\delta(\vec{x})$. What is the power spectrum of a two-dimensional projection

$$g(\vec{\theta}) = \int \mathrm{d}w q(w)\delta[f_K(w)\theta, w] , \qquad (6.45)$$

where $q(w)$ is a weighting function?

Its correlation function is

$$
\begin{aligned}
\xi_{gg} &= \langle g(\vec{\theta})g(\vec{\theta}') \rangle \\
&= \int q(w)\mathrm{d}w \int q(w')\mathrm{d}w' \langle \delta[f_K(w)\vec{\theta}, w]\delta[f_K(w')\vec{\theta}, w'] \rangle .
\end{aligned} \qquad (6.46)
$$

Inserting the Fourier transform of δ, we find

$$
\begin{aligned}
\xi_{gg} &= \int q(w)\mathrm{d}w \int q(w')\mathrm{d}w' \int \frac{\mathrm{d}^3 k}{(2\pi)^3} \int \frac{\mathrm{d}^3 k'}{(2\pi)^3} \langle \hat{\delta}(\vec{k})\hat{\delta}^*(\vec{\kappa}') \rangle \exp{(-if_K(w)\vec{\theta}\vec{k}_\perp} \\
&\quad \exp{(-if_K(w')\vec{\theta}'\vec{k}'_\perp} \exp{(-ik_s w)} \exp{(-ik'_s w')} ,
\end{aligned} \qquad (6.47)
$$

where we have split the wave vector $\vec{k}$ into a perpendicular and a parallel part, $\vec{k}_\perp$ and k_s, respectively. The average over $\hat{\delta}\hat{\delta}^*$ can be replaced by the power spectrum of δ,

$$
\begin{aligned}
\xi_{gg} &= \int q(w)\mathrm{d}w \int q(w')\mathrm{d}w' \int \frac{\mathrm{d}^3 k}{(2\pi)^3} P_\delta(k) \exp{[-i(f_K(w)\vec{\theta} - f_K(w')\vec{\theta}')\vec{k}_\perp]} \\
&\quad \int \mathrm{d}(\Delta w) \exp{(-ik_s \Delta w)} .
\end{aligned} \qquad (6.48)
$$

The last factor,

$$\int \mathrm{d}(\Delta w) \exp{(-ik_s \Delta w)} = 2\pi\delta_D(k_s) , \qquad (6.49)$$

means that only such modes contribute which are perpendicular to the line-of-sight, $\vec{k} = (\vec{k}_\perp, 0)$.

The k_s-integral can the be carried out and we get

$$\xi_{gg} = \int q^2(w)\mathrm{d}w \int \frac{\mathrm{d}^2 k_\perp}{(2\pi)^2} P_\delta(|\vec{k}_\perp|) \exp\left(i f_K(w)(\vec{\theta} - \vec{\theta}')\vec{k}_\perp\right) . \tag{6.50}$$

The difference $\vec{\theta} - \vec{\theta}'$ is the separation vector between the two rays. Defining $\phi \equiv |\vec{\theta} - \vec{\theta}'|$ and using isotropy, we get

$$\begin{aligned}
\xi_{gg}(\phi) &= \int q^2(w)\mathrm{d}w \int \frac{\mathrm{d}^2 k}{(2\pi)^2} P_\delta(k) \exp\left(-i f_K(w)\vec{k}\vec{\phi}\right) \\
&= \int q^2(w)\mathrm{d}w \int \frac{k\mathrm{d}k}{(2\pi)} P_\delta(k) J_0[f_K(w)\phi k] .
\end{aligned} \tag{6.51}$$

The power spectrum of the projected quantity $g(\vec{\theta})$ is

$$\begin{aligned}
P_g(l) &= \int \mathrm{d}^2\phi\, \xi_{gg}(\phi) \exp\left(i\vec{l}\vec{\phi}\right) \\
&= \int q^2(w)\mathrm{d}w \int \frac{\mathrm{d}^2 k}{(2\pi)^2} P_\delta(k) \exp\left\{i[\vec{l} - f_K(w)\vec{k}]\vec{\phi}\right\} \\
&= \int \mathrm{d}w \frac{q^2(w)}{f_K^2(w)} P_\delta\left(\frac{l}{f_K(w)}\right) .
\end{aligned} \tag{6.52}$$

We can now simply read the power spectrum of the effective convergence off the expression for κ_{eff}. With

$$q(w) = \frac{3 H_0^2 \Omega_0}{2c^2} W(w) f_K(w) \frac{1}{a} , \tag{6.53}$$

we have

$$P_\kappa(l) = \frac{9 H_0^4 \Omega_0^2}{4c^2} \int_0^{w_H} \frac{W^2(w)}{a^2} P_\delta\left(\frac{l}{f_K(w)}\right) . \tag{6.54}$$

This power spectrum will be central to all further considerations.

For example, the convergence correlation function is

$$\begin{aligned}
\xi_\kappa(\phi) &= \int \frac{\mathrm{d}^2 l}{(2\pi)^2} P_\kappa(l) \exp\left(-i\vec{l}\vec{\phi}\right) \\
&= \int \frac{l\mathrm{d}l}{2\pi} P_\kappa(l) J_0(l\phi) .
\end{aligned} \tag{6.55}$$

The magnification is, as in the single lens-plane case,

$$\mu = \frac{1}{\det A} \qquad A = I - \frac{\partial\vec{\alpha}}{\partial\vec{\theta}} \tag{6.56}$$

$$\Rightarrow \qquad \mu \approx 1 + \vec{\nabla}_{\vec{\theta}} \cdot \vec{\alpha} = 1 + 2\kappa_{\mathrm{eff}} . \tag{6.57}$$

Thus, the magnification fluctuation, i.e. its deviation from unity, has the correlation function

$$\langle \delta\mu(\vec{\theta})\delta\mu(\vec{\theta} + \vec{\phi})\rangle = \xi_\mu(\phi) = 4\xi_\kappa(\phi) . \tag{6.58}$$

Its r.m.s. value is

$$\langle \delta\mu^2 \rangle^{1/2} = \xi_\mu^{1/2}(0) = \left[\int_0^\infty \frac{l\,\mathrm{d}l}{2\pi} P_\kappa(l) \right]^{1/2} , \tag{6.59}$$

which gives the typical magnification of cosmic sources by large-scale structures.

6.4 Shear correlation functions

Compared to the convergence, the shear depends on the direction with respect to which it is defined. Let ψ be the effective lensing potential and the separation vector $\vec{\phi}$ between any two points have a polar angle α. Then, the tangential component of the shear with respect to that direction is

$$\gamma_t = \gamma(\cos^2\alpha - \sin^2\alpha) = \gamma\cos 2\alpha , \tag{6.60}$$

if α is the polar angle with respect to the principal-axis frame of the shear. Of course, α will vary, so we have to average over it.

Let us now define the correlation function of the tangential shear,

$$\langle \gamma_t \gamma_t' \rangle \equiv \xi_{tt}(\phi) , \tag{6.61}$$

which can be obtained from the power spectrum of the tangential shear component,

$$\xi_{tt}(\phi) = \int \frac{\mathrm{d}^2 l}{(2\pi)^2} P_{\gamma_t}(l) \exp\left(-i\vec{l}\vec{\phi}\right) . \tag{6.62}$$

According to its definition, the tangential component of the shear has the Fourier transform

$$\begin{aligned}
\hat{\gamma}_t &= -\frac{1}{2}(k_1^2 + k_2^2)\hat{\psi} \\
&= \frac{k^2}{2}(\cos^2\alpha - \sin^2\alpha)\hat{\psi} .
\end{aligned} \tag{6.63}$$

Thus, its power spectrum is

$$P_{\gamma_t} = \frac{k^4}{4}(\cos^2\alpha - \sin^2\alpha)^2 P_\psi . \tag{6.64}$$

We know the power spectrum of κ,

$$P_\kappa = \frac{1}{4}(k_1^2 + k_2^2)^2 P_\psi = \frac{k^4}{4} P_\psi , \tag{6.65}$$

so that we can infer P_{γ_t}:

$$P_{\gamma_t} = (\cos^2\alpha - \sin^2\alpha)^2 P_\kappa . \tag{6.66}$$

Now, $(\cos^2\alpha - \sin^2\alpha) = \cos^2 2\alpha = 1/2(1 + \cos 4\alpha)$, from which we find

$$\langle \gamma_t \gamma_t' \rangle = \frac{1}{2} \int \frac{l\,\mathrm{d}l}{2\pi} P_\kappa(l)[J_0(l\phi) + J_4(l\phi)] . \tag{6.67}$$

Similarly, the "cross-component" of the shear is

$$\gamma_x = \gamma\sin 2\alpha , \tag{6.68}$$

and its autocorrelation function is

$$\langle \gamma_x \gamma_x' \rangle = \xi_{xx}(\phi) = \int \frac{\mathrm{d}^2 l}{(2\pi)^2} P_{\gamma_x}(l) \exp\left(-i \vec{l} \vec{\phi}\right) . \tag{6.69}$$

As before, we find

$$
\begin{aligned}
P_{\gamma_x} &= k_1^2 k_2^2 P_\psi = k^4 \cos^2\alpha \sin^2\alpha P_\psi \\
&= 4\cos^2\alpha \sin^2\alpha P_\kappa .
\end{aligned}
\tag{6.70}
$$

Since

$$
\begin{aligned}
4\cos^2\alpha \sin^2\alpha &= 1 - \cos^2 2\alpha = 1 - \frac{1}{2} - \frac{1}{2}\cos 4\alpha \\
&= \frac{1}{2}(1 - \cos 4\alpha) ,
\end{aligned}
\tag{6.71}
$$

we find

$$\langle \gamma_x \gamma_x' \rangle = \frac{1}{2} \int \frac{l\mathrm{d}l}{2\pi} P_\kappa(l)[J_0(l\phi) - J_4(l\phi)] . \tag{6.72}$$

Finally, the mixed correlation function,

$$\langle \gamma_t \gamma_x' \rangle \tag{6.73}$$

follows from the mixed power spectrum,

$$
\begin{aligned}
P_{\gamma_t \gamma_x} &= \frac{1}{2}(k_1^2 - k_2^2)k_1 k_2 \frac{4}{k^4} P_\kappa \\
&= 2(\cos^2\alpha - \sin^2\alpha)\sin\alpha\cos\alpha P_\kappa .
\end{aligned}
\tag{6.74}
$$

Now, $2(\cos^2\alpha - \sin^2\alpha)\sin\alpha\cos\alpha = \cos 2\alpha \sin 2\alpha = \cos 2\alpha \sin 2\alpha = 1/2 \sin 4\alpha$, and this factor makes the correlation function vanish, thus

$$\xi_{tx}(\phi) = 0 . \tag{6.75}$$

It therefore makes sense to define the correlation functions

$$\xi_\pm(\phi) \equiv \langle \gamma_t \gamma_t' \rangle \pm \langle \gamma_x \gamma_x' \rangle , \tag{6.76}$$

and

$$\xi_x(\phi) \equiv \langle \gamma_t \gamma_x' \rangle . \tag{6.77}$$

such that

$$\xi_+(\phi) = \int \frac{l\mathrm{d}l}{2\pi} P_\kappa(l) J_0(l\phi) , \tag{6.78}$$

$$\xi_-(\phi) = \int \frac{l\mathrm{d}l}{2\pi} P_\kappa(l) J_4(l\phi) , \tag{6.79}$$

and the expectation value of $\xi_{(\phi)} = 0$. For any measurement of cosmic shear, $\xi_x(\phi) = 0$ provides a test for the reliability of the measurement, because $\xi_x(\phi) \neq 0$ points at systematic errors.

6.5 Shear in apertures and aperture mass

Another convenient measure for the magnitude of the shear is to compute the mean shear in a (circular) aperture of radius θ,

$$\gamma_{\mathrm{av}}(\theta) = \int_0^\theta \frac{\mathrm{d}^2\Theta}{\pi\Theta^2}\gamma(\vec{\Theta}) , \tag{6.80}$$

and to study its variance,

$$
\begin{aligned}
\langle|\gamma_{\mathrm{av}}|^2\rangle &= \left\langle \int_0^\theta \frac{\mathrm{d}^2\Theta}{\pi\Theta^2} \int_0^\theta \frac{\mathrm{d}^2\Theta'}{\pi\Theta'^2} [\gamma_1(\vec{\Theta})\gamma_1(\vec{\Theta}') + \gamma_2(\vec{\Theta})\gamma_2(\vec{\Theta}')] \right\rangle \\
&= \int_0^\theta \frac{\mathrm{d}^2\Theta}{\pi\Theta^2} \int_0^\theta \frac{\mathrm{d}^2\Theta'}{\pi\Theta'^2} \xi_\kappa(|\vec{\Theta}' - \vec{\Theta}|) .
\end{aligned}
\tag{6.81}
$$

The latter equality follows from the fact that the correlation functions of convergence and absolute value of the sheare are identical, as is best seen from their power spectra. We have

$$
\begin{aligned}
P_\gamma &= \left[\left(\frac{k_1^2 - k_2^2}{2} \right)^2 + k_1^2 k_2^2 \right] P_\psi \\
&= \frac{1}{4}(k_1^4 + k_2^4 - 2k_1^2 k_2^2 + 4k_1^2 k_2^2) P_\psi \\
&= \frac{1}{4}(k_1^2 + k_2^2)^2 P_\psi = \frac{k^4}{4} P_\psi = P_\kappa .
\end{aligned}
\tag{6.82}
$$

Inserting the convergence power spectrum into the shear variance, we obtain

$$
\begin{aligned}
\langle|\gamma_{\mathrm{av}}|^2\rangle(\theta) &= \int_0^\theta \frac{\mathrm{d}^2\Theta}{\pi\Theta^2} \frac{\mathrm{d}^2\Theta'}{\pi\Theta'^2} \int \frac{\mathrm{d}^2l}{(2\pi)^2} P_\kappa(l) \exp(-i\vec{l}(\vec{\Theta} - \vec{\Theta}')) \\
&= 4\pi^2 \int_0^\infty \frac{l\,\mathrm{d}l}{2\pi} P_\kappa(l) \left[\frac{J_1(l\Theta)}{\pi l\Theta} \right]^2 ,
\end{aligned}
\tag{6.83}
$$

for which we have used

$$\int_0^1 x\,\mathrm{d}x\, J_0(ax) = \frac{1}{a}J_1(a) . \tag{6.84}$$

The aperture mass is defined as a weighted integral over the (effective) convergence within a (circular) aperture,

$$M_{\mathrm{ap}}(\theta) = \int_0^\theta \mathrm{d}^2\Theta\, U(\vec{\Theta})\kappa_{\mathrm{eff}}(\vec{\Theta}) . \tag{6.85}$$

If the weight function satisfies the condition

$$\int_0^\theta \Theta\,\mathrm{d}\Theta\, U(\Theta) = 0 , \tag{6.86}$$

i.e. if it is compensated, the aperture mass can also be written as

$$M_{\mathrm{ap}}(\theta) = \int_0^\theta \mathrm{d}^2\Theta\, Q(\Theta)\gamma_t(\vec{\Theta}) , \tag{6.87}$$

where γ_t is the tangential shear with respect to the aperture centre. Q is related to U through

$$Q(x) = \frac{2}{x^2} \int_0^x \mathrm{d}x' x' U(x') - U(x) \;. \tag{6.88}$$

A common choice (but not a neccessary one) is

$$U(\Theta) = \frac{9}{\pi \Theta^2} (1 - x^2) \left(\frac{1}{3} - x^2 \right) \;, \tag{6.89}$$

with $x \equiv \theta/\Theta$. This implies

$$Q(\Theta) = \frac{6}{\pi \Theta^2} x^2 (1 - x^2) \;. \tag{6.90}$$

Using this choice the variance of the aperture mass turns out to be

$$
\begin{aligned}
\langle M_{\mathrm{ap}}^2 \rangle &= \left\langle \int_0^\theta \mathrm{d}^2 \Theta \int_0^\theta \mathrm{d}^2 \Theta' U(\Theta) U(\Theta') \kappa_{\mathrm{eff}}(\vec{\Theta}) \kappa_{\mathrm{eff}}(\vec{\Theta}') \right\rangle \\
&= \int \mathrm{d}^2 \Theta \int \mathrm{d}^2 \Theta' U(\Theta) U(\Theta') \xi_\kappa(|\vec{\Theta}' - \vec{\Theta}|) \\
&= \int \mathrm{d}^2 \Theta \int \mathrm{d}^2 \Theta' U(\Theta) U(\Theta') \int \frac{\mathrm{d}^2 l}{(2\pi)^2} P_\kappa(l) \exp[-i\vec{l}(\vec{\Theta} - \vec{\Theta}')] \\
&= 4\pi \int \frac{l\,\mathrm{d}l}{2\pi} P_\kappa(l) J^2(l\theta) \;,
\end{aligned}
\tag{6.91}
$$

where

$$J(l\theta) \equiv \frac{12}{\pi (l\theta)^2} J_4(l\theta) \;. \tag{6.92}$$

Obviously, the magnification correlation, the shear correlation functions $\xi_p m$, the shear in apertures or the aperture mass all measure weighted integrals of $P_\kappa(l)$, where the weight functions can be more or less peaked.

6.6   E- and B-modes

Shear caused by gravitational lensing cannot have a curl component because of its origin in a scalar potential. If there is a curl component in measured shear, it must therefore be caused by systematic effects. In analogy to electromagnetic fields, real (scalar) modes are called E-modes, others (vectorial modes) are called B-modes.

Assuming E- and B-modes to be independent, the shear powerspectrum can be written as

$$\langle \gamma(\vec{l}) \gamma^*(\vec{l}') \rangle = (2\pi)^2 \delta_D^2(\vec{l} - \vec{l}')[P_E(l) + P_B(l)] \;. \tag{6.93}$$

As before, we now use

$$
\begin{aligned}
\gamma_t &= \gamma(\cos^2 \alpha - \sin^2 \alpha) = \gamma \cos 2\alpha \tag{6.94} \\
\gamma_x &= \gamma 2 \sin \alpha \cos \alpha = \gamma \sin 2\alpha \;, \tag{6.95}
\end{aligned}
$$

and find

$$\xi_+(\phi) = \int \frac{l\,\mathrm{d}l}{2\pi} [P_E(l) + P_B(l)] J_0(l\phi) \tag{6.96}$$

and

$$\xi_-(\phi) = \int \frac{l \mathrm{d}l}{2\pi} [P_E(l) - P_B(l)] J_4(l\phi) \ . \tag{6.97}$$

Using Fourier transforms, these relations can be inverted to yield

$$P_E(l) = \int_0^\infty \phi \mathrm{d}\phi [\xi_+(\phi) J_0(l\phi) + \xi_-(\phi) J_4(l\phi)] \ , \tag{6.98}$$

$$P_E(l) = \int_0^\infty \phi \mathrm{d}\phi [\xi_+(\phi) J_0(l\phi) - \xi_-(\phi) J_4(l\phi)] \ . \tag{6.99}$$

This allows quantifying E- and B-mode contributions to the signal.

In particular, the aperture mass is only sensitive to E modes, while

$$M_{\mathrm{ap}\perp} \equiv \int_0^\theta \Theta \mathrm{d}\Theta Q(\Theta)\gamma_x(\Theta) \tag{6.100}$$

is only sensitive to B-modes. That way, they can be easily compared.

6.7 Lensing of the Cosmic Microwave Background

Lensing also changes the appearance of the CMB, because temperature fluctuations originally at a position $\vec{\beta}$ are shifted to $\vec{\theta} = \vec{\beta} + \vec{\alpha}$ due to lensing.

The CMB is characterized by its relative temperature fluctuations

$$\tau(\vec{\theta}) \equiv \frac{T(\vec{\theta})}{\langle T \rangle} \tag{6.101}$$

and their power spectrum

$$P_T(l) = \langle \hat{\tau}(\vec{l})\hat{\tau}^*(\vec{l'}) \rangle = \int \mathrm{d}^2\phi \, \xi_T(\phi) \exp(-i\vec{\phi}\vec{l}) \ . \tag{6.102}$$

We wish to calculate how the power spectrum of the CMB will change due to lensing. The temperature autocorrelation function without lensing would be

$$\langle \tau(\vec{\theta})\tau(\vec{\theta} + \vec{\phi}) \rangle \ , \tag{6.103}$$

with lensing it is

$$\langle \tau(\vec{\theta} - \vec{\alpha})\tau(\vec{\theta'} - \vec{\alpha'}) \rangle \ , \tag{6.104}$$

where $\vec{\alpha} = \vec{\alpha}(\vec{\theta})$ and $\vec{\alpha'} = \vec{\alpha'}(\vec{\theta'})$; $\vec{\theta'} = \vec{\theta} + \vec{\phi}$.

In terms of Fourier transforms

$$\tau(\vec{\theta} - \vec{\alpha}) = \int \frac{\mathrm{d}^2 l}{(2\pi)^2} \hat{\tau}(\vec{l}) \exp[-i(\vec{\theta} - \vec{\alpha})] \ , \tag{6.105}$$

thus

$$
\begin{aligned}
\xi_T(\phi) &= \left\langle \int \frac{\mathrm{d}^2 l}{(2\pi)^2} \hat{\tau}(\vec{l}) \exp[-i(\vec{\theta} - \vec{\alpha})\vec{l}] \int \frac{\mathrm{d}^2 l'}{(2\pi)^2} \hat{\tau}^*(\vec{l'}) \exp[i(\vec{\theta'} - \vec{\alpha'})\vec{l'}] \right\rangle \\
&= \int \frac{\mathrm{d}^2 l}{(2\pi)^2} \int \frac{\mathrm{d}^2 l'}{(2\pi)^2} \langle \hat{\tau}(\vec{l})\hat{\tau}^*(\vec{l'}) \rangle \langle \exp[-i(\vec{\theta} - \vec{\alpha})\vec{l}] \exp[i(\vec{\theta'} - \vec{\alpha'})\vec{l'}] \rangle \\
&= \int \frac{\mathrm{d}^2 l}{(2\pi)^2} P_T(l) \exp[-i(\vec{\theta} - \vec{\theta'})\vec{l}] \langle \exp[i(\vec{\alpha} - \vec{\alpha'})\vec{l}] \rangle \ .
\end{aligned} \tag{6.106}
$$

The two averages are separated because one extends over the unlensed CMB temperature fluctuations and the other over the deflection-angle differences.

Typical angular scales in the CMB are large compared to the deflection-angle differences, so $\vec{l}(\vec{\alpha} - \vec{\alpha}')$ is usually a small number. Thus,

$$
\begin{aligned}
\langle \exp[i(\vec{\alpha} - \vec{\alpha}')\vec{l}] \rangle &\approx 1 + i\langle(\vec{\alpha} - \vec{\alpha}')\vec{l}\rangle - \frac{1}{4}\langle < (\vec{\alpha} - \vec{\alpha}')^2\rangle l^2 \\
&\approx \exp\left[-\frac{1}{2}\sigma^2(\phi)l^2\right] ,
\end{aligned}
\tag{6.107}
$$

with

$$
\sigma^2(\phi) \equiv \frac{1}{2}\langle(\vec{\alpha} - \vec{\alpha}')^2\rangle .
\tag{6.108}
$$

Thus,

$$
\begin{aligned}
\xi_T(\phi) &= \int \frac{\mathrm{d}^2 l}{(2\pi)^2} P_T(l)\exp(-\sigma^2 l^2/2)\exp(-i\vec{\phi}\vec{l}) \\
&= \int \frac{l\mathrm{d}l}{2\pi} P_T(l)\exp(-\sigma^2 l^2/2)J_0(l\phi) .
\end{aligned}
\tag{6.109}
$$

Therefore, the effect of lensing on the CMB is to smooth the CMB fluctuations on scales smaller than $\sim \sigma(\phi)$.

In order to calculate $\sigma(\phi)$, we use the deflection-angle correlation function,

$$
\xi_{\vec{\alpha}} = \langle \vec{\alpha}\vec{\alpha}' \rangle = \langle \alpha_1 \alpha_1' \rangle + \langle \alpha_2 \alpha_2' \rangle = \xi_{\alpha_1} + \xi_{\alpha_2} .
\tag{6.110}
$$

In terms of $\xi_{\vec{\alpha}}$, we have

$$
\begin{aligned}
\sigma^2(\phi) &= \frac{1}{2}\langle \vec{\alpha}^2 + \vec{\alpha}\vec{\alpha}' + \vec{\alpha}'\vec{\alpha} + \vec{\alpha}'^2 \rangle \\
&= \xi_{\vec{\alpha}}(0) + \xi_{\vec{\alpha}}(\phi) .
\end{aligned}
\tag{6.111}
$$

Since $\vec{\alpha} = \vec{\nabla}\psi$, the power spectrum of $\vec{\alpha}$ is

$$
\langle \hat{\vec{\alpha}}\hat{\vec{\alpha}}'^* \rangle = l^2 P_\psi = \frac{4}{l^2}P_\kappa ,
\tag{6.112}
$$

hence

$$
\xi_{\vec{\alpha}}(\phi) = \int \frac{l\mathrm{d}l}{2\pi}\frac{4}{l^2}P_\kappa(l)J_0(l\phi) .
\tag{6.113}
$$

For $\phi \sim 10'$, $\sigma(\phi) \sim 0.05' \approx 3''$.

The lensed CMB power spectrum is

$$
\begin{aligned}
P_T'(l) &= \int \mathrm{d}\phi\, \xi_T(\phi)\exp(i\vec{\phi}\vec{l}) \\
&= \int \mathrm{d}^2\phi \int \frac{\mathrm{d}^2 l'}{(2\pi^2)}P_T(l')\exp(-\sigma^2 l'^2/2)\exp[i\vec{\phi}(\vec{l} - \vec{l}')] ,
\end{aligned}
\tag{6.114}
$$

which illustrates again that lensing smoothes the intrinsic CMB power spectrum.

Bibliography

Afonso, C., Albert, J. N., Andersen, J., Ansari, R., Aubourg, É., Bareyre, P., Beaulieu, J. P., Blanc, G., Charlot, X., Couchot, F., Coutures, C., Ferlet, R., Fouqué, P., Glicenstein, J. F., Goldman, B., Gould, A., Graff, D., Gros, M., Haissinski, J., Hamadache, C., de Kat, J., Lasserre, T., Le Guillou, L., Lesquoy, É., Loup, C., Magneville, C., Marquette, J. B., Maurice, É., Maury, A., Milsztajn, A., Moniez, M., Palanque-Delabrouille, N., Perdereau, O., Prévot, L., Rahal, Y. R., Rich, J., Spiro, M., Tisserand, P., Vidal-Madjar, A., Vigroux, L., & Zylberajch, S., 2003, *A & A* , **400**, 951

Alcock, C., Allsman, R. A., Alves, D. R., Axelrod, T. S., Becker, A. C., Bennett, D. P., Cook, K. H., Dalal, N., Drake, A. J., Freeman, K. C., Geha, M., Griest, K., Lehner, M. J., Marshall, S. L., Minniti, D., Nelson, C. A., Peterson, B. A., Popowski, P., Pratt, M. R., Quinn, P. J., Stubbs, C. W., Sutherland, W., Tomaney, A. B., Vandehei, T., & Welch, D., 2000, *ApJ* , **542**, 281

Bartelmann, M., 1996, *A&A*, **313**, 697

Bartelmann, M., Meneghetti, M., Perrotta, F., Baccigalupi, C., & Moscardini, L., 2002a, astro-ph/0210066

Bartelmann, M., Perrotta, F., & Baccigalupi, 2002b, astro-ph/0206507

Bond, I. A., Udalski, A., Jaroszyński, M., Rattenbury, N. J., Paczyński, B., Soszyński, I., Wyrzykowski, L., Szymański, M. K., Kubiak, M., Szewczyk, O., Żebruń, K., Pietrzyński, G., Abe, F., Bennett, D. P., Eguchi, S., Furuta, Y., Hearnshaw, J. B., Kamiya, K., Kilmartin, P. M., Kurata, Y., Masuda, K., Matsubara, Y., Muraki, Y., Noda, S., Okajima, K., Sako, T., Sekiguchi, T., Sullivan, D. J., Sumi, T., Tristram, P. J., Yanagisawa, T., & Yock, P. C. M., 2004, *ApJL* , **606**, L155

Bullock, J. S., Kolatt, T. S., Sigad, Y., Somerville, R. S., Kravtsov, A. V., Klypin, A. A., Primack, J. R., & Dekel, A., 2001, *MNRAS*, **321**, 559

Diego, J. M., Protopapas, P., Sandvik, H. B., & Tegmark, M., 2005, *MNRAS*, **360**, 477

Einstein, A., 1916, *Ann. der Ph.*, **49**, 769

Eke, V. R., Navarro, J. F., & Steinmetz, M., 2001, *ApJ* , **554**, 114

Fassnacht, C. D., Xanthopoulos, E., Koopmans, L. V. E., & Rusin, D., 2002, *ApJ* , **581**, 823

Garrett, M. A., Calder, R. J., Porcas, R. W., King, L. J., Walsh, D., & Wilkinson, P. N., 1994, *MNRAS*, **270**, 457

Golse, G. & Kneib, J.-P., 2002, *A&A*, **390**, 821

Irwin, M. J., Webster, R. L., Hewett, P. C., Corrigan, R. T., & Jedrzejewski, R. I., 1989, *AJ* , **98**, 1989

Kassiola, A., Kovner, I., & Fort, B., 1992, *ApJ*, **400**, 41

Kerins, E., Carr, B. J., Evans, N. W., Hewett, P., Lastennet, E., Le Du, Y., Melchior, A.-L., Smartt, S. J., & Valls-Gabaud, D., 2001, $MNRAS$, **323**, 13

Kochanek, C. S., 2004, *ArXiv Astrophysics e-prints*,

Koopmans, L. V. E., Treu, T., Fassnacht, C. D., Blandford, R. D., & Surpi, G., 2003, *ApJ*, **599**, 70

Kormann, R., Schneider, P., & Bartelmann, M., 1994, *A&A*, **284**, 285

Li, L. & Ostriker, J. P., 2002, ApJ, **566**, 652

Mao, S., Jing, Y., Ostriker, J. P., & Weller, J., 2004, $ApJL$, **604**, L5

Mao, S. & Paczynski, B., 1991, $ApJL$, **374**, L37

Mao, S. & Schneider, P., 1998, $MNRAS$, **295**, 587

Meneghetti, M., Bartelmann, M., & Moscardini, L., 2002, astro-ph/0201501

Narayan, R. & Bartelmann, M., 1995, in A. Dekel and J. Ostriker (eds.), *Formation of Structure in the Universe*, 1995 Jerusalem Winter School, Cambridge University Press

Navarro, J. F., Frenk, C. S., & White, S. D. M., 1997, *ApJ*, **490**, 493+

Paczynski, B., 1986, *ApJ*, **301**, 503

Paczynski, B., 1996, *ARAA*, **34**, 419

Patnaik, A. R., Browne, I. W. A., Walsh, D., Chaffee, F. H., & Foltz, C. B., 1992, $MNRAS$, **259**, 1P

Perrotta, F., Baccigalupi, C., Bartelmann, M., De Zotti, G., & Granato, G. L., 2002, $MNRAS$, **329**, 445

Rattenbury, N. J., 2006, *Modern Physics Letters A*, **21**, 919

Refsdal, S., 1964, *MNRAS*, **128**, 307

Rusin, D., Kochanek, C. S., & Keeton, C. R., 2003, ApJ, **595**, 29

Schneider, P., Ehlers, J., & Falco, E., 1992, *Gravitational Lenses*, (Heidelberg: Springer)

Schneider, P. & Weiss, A., 1986, $A \& A$, **164**, 237

Shapiro, I. I., 1964, *Phys. Rev. Lett.*, **13**, 789

Soldner, J., 1801, *Berliner Astronomisches Jahrbruch fuer Jahr 1804*, Cambridge University Press

Udalski, A., Szymanski, M., Mao, S., Di Stefano, R., Kaluzny, J., Kubiak, M., Mateo, M., & Krzeminski, W., 1994, $ApJL$, **436**, L103

Wambsganss, J., 1990, *NASA STI/Recon Technical Report N*, **92**, 22300

Wambsganss, J., 2006, astro-ph/0604278

Wambsganss, J. & Paczynski, B., 1992, $ApJL$, **397**, L1

Will, C. M., 1988, *Am. J. Phys.*, **56**, 5

Witt, H. J. & Mao, S., 1995, *ApJL* , **447**, L105+

Woźniak, P. R., Alard, C., Udalski, A., Szymański, M., Kubiak, M., Pietrzyński, G., & Zebruń, K., 2000a, *ApJ* , **529**, 88

Woźniak, P. R., Udalski, A., Szymański, M., Kubiak, M., Pietrzyński, G., Soszyński, I., & Żebruń, K., 2000b, *ApJL* , **540**, L65

Wright, C. O. & Brainerd, T. G., 2000, *ApJ* , **534**, 34

Wyithe, J. S. B., Turner, E. L., & Spergel, D. N., 2001, *ApJ* , **555**, 504